CHARACTERIZATION AND PREDICTIVE MODELING OF THERMALLY AGED GLASS FIBER REINFORCED PLASTIC COMPOSITES

MD MIJANUR RAHMAN

M.SC. ENGINEERING THESIS

DEPARTMENT OF AERONAUTICAL ENGINEERING
MILITARY INSTITUTE OF SCIENCE AND TECHNOLOGY
DHAKA, BANGLADESH

JULY 2023

CHARACTERIZATION AND PREDICTIVE MODELING OF THERMALLY AGED GLASS FIBER REINFORCED PLASTIC COMPOSITES

MD MIJANUR RAHMAN (SN. 0420220002)

A Thesis Submitted in Partial Fulfillment of the Requirements for the Degree of Master of Science in Aeronautical Engineering

DEPARTMENT OF AERONAUTICAL ENGINEERING
MILITARY INSTITUTE OF SCIENCE AND TECHNOLOGY
DHAKA, BANGLADESH

JULY 2023

CHARACTERIZATION AND PREDICTIVE MODELING OF THERMALLY AGED GLASS FIBER REINFORCED PLASTIC COMPOSITES

M.Sc. Engineering Thesis

By

MD MIJANUR RAHMAN (SN. 0420220002)

Approved as to style and content by the Board of Examination on 13th July 2023

_____ Commodore M Muzibur Rahman, psc, PhD (Retd.) Professor Department of Naval Arch. & Marine Engineering MIST, Dhaka.	Chairman (Supervisor) Board of Examination
_____ Md Atif Yasir Assistant Professor Department of Mechanical Engineering MIST, Dhaka.	Member (Co-Supervisor) Board of Examination
_____ Dr. Shaikh Reaz Ahmed Professor Department of Mechanical Engineering BUET, Dhaka.	Member (External) Board of Examination
_____ Dr. Shahida Begum Professor Department of Mechanical Engineering MIST, Dhaka.	Member (Internal) Board of Examination
_____ Air Cdre Md Aminul Haque, ndc, psc Head Department of Aeronautical Engineering MIST, Dhaka.	Head of the Department (Ex-Officio)

Department of Aeronautical Engineering, MIST, Dhaka

CHARACTERIZATION AND PREDICTIVE MODELING OF THERMALLY AGED GLASS FIBER REINFORCED PLASTIC COMPOSITES

DECLARATION

I hereby declare that the study reported in this thesis entitled as above is my own original work and has not been submitted before anywhere before for any degree or other purpose. Further I certify that the intellectual content of this thesis is the product of my own work and that all the assistance received in preparing this thesis and sources have been acknowledged and/or cited in the reference section.

_____

Md Mijanur Rahman

Department of Aeronautical Engineering, MIST, Dhaka.

CHARACTERIZATION AND PREDICTIVE MODELING OF THERMALLY AGED GLASS FIBER REINFORCED PLASTIC COMPOSITES

A Thesis

By

Md Mijanur Rahman

DEDICATION

Dedicated to my family for supporting and encouraging me to be the best I can be.

ACKNOWLEDGEMENT

The author would like to convey his heartiest gratitude to Commodore M Muzibur Rahman, psc, PhD (Retd.), Professor, Department of Naval Architecture and Marine Engineering, MIST for his relentless support, guidance, supervision and encouragement throughout the entire research work. The author also gratefully acknowledges the invaluable suggestion and cooperation of Md Atif Yasir, Assistant Professor, Department of Mechanical Engineering, MIST.

The author wishes to express his sincere gratitude to Air Cdre Md Aminul Haque, ndc, psc, Professor and Head, Department of Aeronautical Engineering, MIST for his utmost support and guidance regarding an excellent research environment.

The author also wishes to convey his thanks and gratitude to Dr. Shaikh Reaz Ahmed, Professor, Department of Mechanical Engineering, BUET and Dr. Shahida Begum, Professor, Department of Mechanical Engineering, MIST for their comments, suggestions and approvals have undoubtedly enhanced the quality of the work.

Special thanks are offered to Mr. Razu, Mr. Nazmul and other lab staff of MIST for their cooperation in this research. The author also acknowledges the support of MAWTS for GFRP fabrication and BCSIR for their support in SEM testing.

Finally, the author expresses his devoted affection to his family and friends for their moral support and sacrifice in completing the thesis.

ABSTRACT

Characterization And Predictive Modeling Of Thermally Aged Glass Fiber Reinforced Plastic Composites

This study investigated the characterization and predictive modeling of thermally aged Glass Fiber Reinforced Plastic (GFRP) Composites. The experimental part of the study explored the effect of fiber orientation, laser cutting and thermal aging on GFRP mechanical properties. The development of a predictive model for estimating the mechanical properties of thermally aged GFRP was explored in the computational part. GFRP composites were fabricated with woven and random glass fiber and epoxy resin hardener and subjected to mechanical and laser machining. Mechanical property testing reveals that Tensile and flexural properties are found to be superior in mechanically cut samples. Compromised surface integrity due to thermal damage in the case of laser cut samples is also noted. All results indicated that woven GFRP has superior mechanical properties than random GFRP. Woven GFRP tensile test samples were thermally aged at 50°C, 100°C, 150°C and 200°C for 30 mins, 60 mins, 90 mins and 120 mins. The samples showed a gradually increasing brown color at temperatures above 150°C. The tensile test showed that the Ultimate Tensile Strength (UTS) value had a general decreasing trend as the thermal aging temperature increased. The predictive model read the photographic image of a thermally aged sample and used the color change due to thermal aging as an identifier for the image processing algorithm. Artificial Neural Networks (ANN) estimated the thermal aging temperature and time from the image processing algorithm's Red Green Blue (RGB) color matrix output. A regression equation was also developed which creates a mathematical relationship between the UTS values and the thermal aging variables from the experimental data. Finally, the ANN's output was forwarded to the developed regression equation to get the estimated UTS. The predictive model's estimated UTS showed an average accuracy of 97% compared to the experimental results. The results of the characterization of mechanical properties of thermally aged GFRP can contribute meaningful insights into the existing literature. The developed predictive model can have potential applications in aerospace line maintenance operations with the promise of cost and time savings.

সারসংক্ষেপ

Characterization And Predictive Modeling Of Thermally Aged Glass Fiber Reinforced Plastic Composites

এই গবেষণাটিতে তাপপ্রভাবিত গ্লাস ফাইবার রিইনফোর্সড প্লাস্টিক (জিএফআরপি) কম্পোজিটগুলির ভৌত বৈশিষ্ট্য এবং প্রাক্কলনমূলক মডেলিং অনুসন্ধান করা হয়েছে। গবেষণার পরীক্ষামূলক অংশটিতে জিএফআরপি-র ভৌত বৈশিষ্ট্যগুলিতে ফাইবার অভিযোজন, লেজার কাটিং এবং তাপপ্রভাবনের প্রভাব অন্বেষণ করা হয়েছে। তাপপ্রভাবিত জিএফআরপি-র ভৌত বৈশিষ্ট্য অনুমান করার জন্য একটি প্রাক্কলনমূলক মডেলিং গঠন গবেষণার গণনামূলক অংশে অন্বেষণ করা হয়েছে। জিএফআরপি কম্পোজিটগুলি বোনা ও এলোমেলো গ্লাস ফাইবার এবং ইপোক্সি রজন ও হার্ডনার দিয়ে তৈরি করা হয়েছিল এবং যান্ত্রিক ও লেজার মেশিনিংয়ের মাধ্যমে কাটা হয়েছিল। ভৌত বৈশিষ্ট্যের পরীক্ষায় দেখা যায় যে প্রসার্য এবং নমনীয় বৈশিষ্ট্যগুলি যান্ত্রিকভাবে কাটা নমুনাগুলিতে উচ্চতর। লেজার কাটা নমুনার ক্ষেত্রে তাপজনিত কারণে পৃষ্ঠের ক্ষতি লক্ষণীয়। সমস্ত ফলাফল ইঙ্গিত করে যে বোনা জিএফআরপি এলোমেলো জিএফআরপির চেয়ে উচ্চতর ভৌত বৈশিষ্ট্য সম্পন্ন। বোনা জিএফআরপি-র প্রসার্য পরীক্ষার নমুনাগুলি ৫০, ১০০, ১৫০ এবং ২০০- ডিগ্রী সেলসিয়াসে ৩০ মিনিট, ৬০ মিনিট, ৯০ মিনিট এবং ১২০ মিনিটের জন্য তাপপ্রভাবিত করা হয়েছিল। নমুনাগুলি ১৫০ ডিগ্রি সেলসিয়াসের উপরে তাপমাত্রায় ধীরে ধীরে ক্রমবর্ধমান বাদামী রঙ ধারণ করেছিল। প্রসার্য পরীক্ষায় দেখা গেছে যে তাপ প্রভাবনের তাপমাত্রা বৃদ্ধির সাথে সাথে চরম প্রসারনযোগ্য শক্তি (ইউটিএস) মান হ্রাসের একটি সাধারণ প্রবণতা রয়েছে। প্রাক্কলনমূলক মডেলটিতে তাপপ্রভাবিত নমুনার ফটোগ্রাফিক চিত্রটি পাঠ করে তাপ প্রভাবনের কারণে রঙ পরিবর্তনের বিষয়টি চিত্র প্রক্রিয়াকরণ অ্যালগরিদমের শনাক্তকারী ইঙ্গিত হিসাবে ব্যবহার করা হয়েছিল। কৃত্রিম নিউরাল নেটওয়ার্কগুলি (এ এন এন) চিত্র প্রক্রিয়াকরণ অ্যালগরিদমের লাল সবুজ নীল (লা স নী) রঙের ম্যাট্রিক্স থেকে তাপপ্রভাবনের তাপমাত্রা এবং সময় অনুমান করে। একটি প্রত্যাবৃত্তি সমীকরণও তৈরি করা হয়েছে যা পরীক্ষামূলক উপাত্ত থেকে ইউটিএস-র মান এবং তাপপ্রভাবনের চলকগুলোর মধ্যে একটি গাণিতিক সম্পর্ক তৈরি করে। অবশেষে, আনুমানিক ইউটিএস পেতে এ এন এন-এর ফলাফল প্রত্যাবৃত্তি সমীকরণে প্রয়োগ করা হয়। প্রাক্কলনমূলক মডেলের আনুমানিক ইউটিএস পরীক্ষামূলক ফলাফলের তুলনায় ৯৭% গড় নির্ভুলতা দেখায়। তাপপ্রভাবিত জিএফআরপি-র ভৌত বৈশিষ্ট্যের ফলাফলগুলি বিদ্যমান জ্ঞানভাণ্ডারে অর্থপূর্ণ অন্তর্দৃষ্টিমূলক অবদান রাখতে পারে। প্রাক্কলনমূলক মডেলের খরচ এবং সময় সাশ্রয়ের প্রতিশ্রুতি সহ বিমান প্রকৌশলের লাইন রক্ষণাবেক্ষণ কার্যক্রমে প্রয়োগের সম্ভাব্যতা রয়েছে।

LIST OF MAIN NOTATIONS

GFRP	Glass Fiber Reinforced Plastic
FRP	Fiber Reinforced Plastic
ANN	Artificial Neural Network
Tg	Glass Transition Temperature
UTS	Ultimate Tensile Strength
UFS	Ultimate Flexural Strength
HAZ	Heat Affected Zone
ASTM	American Society for Testing and Materials
RGB	Red Green Blue
HV	Vickers Microhardness
SGN	Sample Group Number
SEM	Scanning Electron Microscope
MC	Mechanically Cut
LC	Laser Cut

LIST OF TABLES

LIST OF FIGURES

TABLE OF CONTENTS

CHAPTER 1
INTRODUCTION

1.1 Background of the Study

Glass fiber reinforced plastic (GFRP), a type of Fiber Reinforced Plastic (FRP) composite having glass fibers as the reinforcing element, has received widespread attraction in many applications including aerospace, marine, automobile and sports components due to mainly high strength-to-weight ratio, sustainability at cryogenic as well as elevated temperature, notable surface finishing, attractive aesthetic view, corrosion resistance and wear resistance (Ghafarizadeh et al., 2015; Krishnamoorthy et al., 2009; Rao B et al., 2019).

The mechanical behavior of a fiber-reinforced composite depends on the fiber strength and modulus, the chemical stability, matrix strength and the interface bonding between the fiber/matrix to enable stress transfer (Erden et al., 2010). Scientists and engineers are well aware of the properties of fiber reinforced polymers, but there are still a lot of unsolved questions concerning their durability and performance under harsh environmental conditions (Bakis et al., 2002). In aerospace applications, GFRP composites are subjected to thermal aging at elevated temperatures, especially in Unmanned Aerial Vehicle (UAV) operations, aircraft fuselage panels, aircraft wingtips, control surfaces, bleed air ducts and inlet fan blade casing (Pavan et al., 2021).

Several researchers have studied the thermal aging effect of GFRPs and predictive modeling techniques. Kun et al. used epoxy resin and glass fiber and performed wet and heat cycle aging tests, finding that the composites' mechanical and dielectric properties deteriorate over time. Lan et al. studied the color changes and mechanical properties of glass fiber-reinforced polycarbonate (GF-PC) composites after aging at various temperatures and revealed that the brightness of the GF-PC composites relates with trends detected in their tensile strength and bending strength.

A good number of researchers have also investigated the computational methods to estimate the mechanical properties of GFRP particularly when exposed to thermal aging. Gibson et al. studied raised temperature effect on mechanical property measurements of woven glass fiber/polypropylene composites and suggested a 3-parameter model to define the tensile behavior and a 2-parameter model to define the compressive behavior to analyze the effects.

Kim and Oh, experimented with multiple regression analysis (MRA), polynomial regression analysis (PRA) and Artificial Neural Networks (ANNs) to analyze issues affecting the tensile strength of basalt and glass fiber-reinforced polymers (FRPs). They found that ANNs can be the most efficient model for forecasting the durability of FRPs.

This research is focused on the characterization and predictive modeling of thermally GFRP composites. The predictive model will be developed using image processing, regression analysis and artificial neural networks. This model will be able to make predictions about the mechanical properties of thermally aged GFRP with a photographic image of the sample.

1.2 Problem Statement

There is significant literature on varying fiber orientation and the addition of different fillers in GFRP; leading to a comparison of the changes in mechanical properties. The effects of different types of machining have also been studied. The mechanical property testing of thermally aged GFRP has also been studied in detail. Also, several predictive models using multi-parameter models, regression and ANN techniques have been developed with good accuracy. It is evident that regarding thermal aging, on a macroscopic level, the physical and chemical mechanisms causing a change in GFRP properties are well understood. However, the mechanical property values reported by different researchers remain in a large scatter for thermally aged GFRP. The precise physical micro-phenomena and chemical reactions, as well as how they interact, are still being researched. Again, most of the predictive models in the literature depend on testing the material and predicting the output value based on the test input parameters. This is a time-consuming process that involves disassembly, sample preparation and destructive testing. It costs a lot of money for applications in aerospace, automobile, marine and similar industries. As such, a computational method to estimate the mechanical properties of thermally aged GFRP would be very beneficial for highly competitive and operational industries like Aerospace. As such, the literature survey pinpoints the following problem statements:

i. Mechanical property testing of thermally aged GFRP shows variations in results reported by researchers.
ii. Determining the physical state of the GFRP after thermal aging and retracing the mechanical and thermal histories are difficult tasks.

iii. A data-driven computational method to estimate the mechanical properties of thermally aged GFRP remains largely unaddressed.

1.3 Research Objectives

The objectives of this research are as follows:

i. To fabricate GFRP composites with woven and random fibers, epoxy resin-hardener.

ii. To characterize and compare the mechanical properties of thermally aged GFRP composites.

iii. To develop a predictive model for estimating the mechanical properties of thermally aged GFRP composites.

GFRP samples are to be prepared from composite slabs. Tensile, Flexural and Microhardness tests are to be carried out. SEM imaging is to be performed to supplement the findings of the mechanical property testing at room temperature. The tensile test will also be carried out after the thermal aging of GFRP samples. Thereafter, a predictive model is to be developed to estimate the Ultimate Tensile Strength (UTS) of thermally aged samples.

1.4 Scope of this Work

The scope of this work regarding the Characterization and Predictive Modeling of Thermally Aged Glass Fiber Reinforced Plastic Composites encompasses several key areas of investigation.

i. GFRP Fabrication: GFRP composites will be prepared using woven and randomly oriented glass fibers. Epoxy resin will be used as the matrix. The composite slab will be prepared by the hand lay-up method.

ii. Machining: A study of two types of machining namely mechanical cutting using an angle grinder and laser cutting using a CO_2 laser machine will be performed to produce the samples for mechanical property testing.

iii. Thermal Aging: The prepared samples will be thermally aged in ovens below and beyond the glass transition temperature (Tg). The selected temperature will be chosen with Aerospace applications in mind. Samples will be thermally aged at different temperatures with different aging times.

iv. Characterization of Mechanical Properties: Several mechanical properties of the GFRP samples will be tested including Tensile, Flexural, Microhardness and SEM Imaging. The thermally aged samples will undergo a tensile test to show the effect of thermal aging on Ultimate Tensile Strength (UTS). A dataset containing the mechanical properties of the thermally aged GFRP composite will be developed after the completion of the mechanical property testing.

v. Predictive Modeling: A predictive model will be developed to estimate the mechanical properties of the thermally aged GFRP composites. The model will use the dataset developed earlier. This model will be developed by combining image processing, regression analysis and artificial neural networks (ANNs). The model will be able to estimate the mechanical properties of the thermally aged GFRP composite from its photographic image. This will be accomplished by using the color changes due to thermal aging as an identifier for the image processing algorithm. The regression analysis will develop a mathematical model with the desired mechanical property as the output and the thermal aging temperature and time as the input. Afterward, two ANNs will be trained and tested to estimate the thermal aging temperature and time from the image processing algorithm. The ANN output variables will be sent to the mathematical model to estimate the mechanical property of the thermally aged GFRP. Finally, a comparison will be made between the experimental results and the predictive model's estimation

1.5 Significance of this Research

The research aims to experimentally study the mechanical properties and machinability of thermally aged GFRP and provide sets of data for future reference as well as shed light on the variations in results reported by researchers. Also, the predictive model can estimate the Ultimate Tensile Strength (UTS) values only from a photographic image of the sample. This model has the potential to save time and money by avoiding disassembly, sample preparation and destructive testing of GFRP components especially in aerospace line maintenance applications.

1.6 Novelty of this Research

Laser machining of GFRP and its SEM imaging provides new information regarding the effect of very high temperatures on the mechanical properties of GFRP.

Thermal aging of GFRP contributes contemporary insights into the interdependency of thermal aging temperature and time for the chosen configurations.

The predictive model developed in this research and its exact design is completely novel and it has not been studied yet by researchers as per the literature review and best knowledge of the author.

1.7 Potential Application

The predictive model developed in this research has the potential to estimate the mechanical properties of in-service aerospace parts which have been subjected to thermal aging. The model can estimate the UTS value from a photographic image only. This can lead to time and cost savings by avoiding the disassembly and testing of thermally aged parts. In the case of aerospace applications, this model can be used to take a photo of a thermally aged GFRP part and assist in deciding its airworthiness status with reference to Aircraft Maintenance Manual (AMM). The model can be retrofitted and adapted to predict a multitude of Mechanical properties.

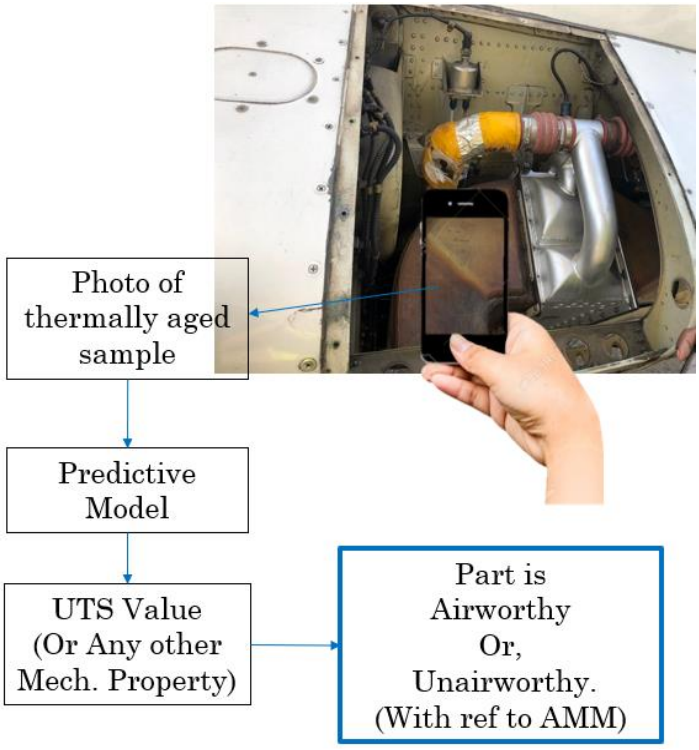

Fig. 1.1: Potential application of the predictive model.

1.8 Organization of the Thesis

This thesis is presented in several chapters, starting with Introduction, and ending with Conclusions. Each of the other chapters has a precise title reflecting the contents of the chapter. A chapter is further subdivided into sections, subsections and subsubsection to present the content discretely and with due emphasis.

Chapter 1 is the Introduction. It gives a brief background to the problem and highlights the importance of the study. It outlines the scope, aim, general character of the research and the reasons for the interest in the problem.

Chapter 2 is Literature Review. This chapter demonstrates a systematic examination of the scholarly literature on the research topic. The literature review chapter aims to delineate various theoretical positions and from these, develop a conceptual framework for the generation of hypotheses and setting up the research question.

Chapter 3 is Materials and Methodology. Here, materials and research methods used are provided in detail so that other researchers can repeat the experiments. Sufficient information is given allowing the readers to judge whether the experimental methods are suitable and, consequently, whether the validity of the findings are acceptable.

Chapter 4 is Characterization of GFRP. This chapter covers how the GFRP was fabricated, and machined and what mechanical property testing was carried out in the experimental work. This section also reports the experimental data through Tables and Figures, emphasizing important patterns or trends. Results and discussions relevant to the experimental work is also discussed.

Chapter 5 is Predictive Modeling of GFRP. The overview and methodology of the predictive model is discussed here. This chapter introduces the different elements of the predictive model, explains their software architecture and how they are developed. The results of the individual elements are also presented. Results and discussions relevant to the computational work is also discussed.

Chapter 6 is Conclusions. This chapter states the conclusions drawn from the study and interpretations in a concise form. It bridges the culmination of the research work and relates it to the objective of the study. Potential applications, limitations and future recommendations of this study are also discussed.

Finally, A List of references and appendices are placed at the end of the thesis.

CHAPTER 2
LITERATURE REVIEW

2.1 Background on Composite Materials

Composite materials are engineered materials made up of two or more distinct components with different physical or chemical properties. These components, known as the matrix and the reinforcement, work together to create a composite material with improved overall properties compared to the individual components. The matrix material holds the reinforcement in place and transfers loads between the reinforcement elements, while the reinforcement material provides strength and stiffness to the composite. The combination of the matrix and reinforcement materials allows composite materials to exhibit superior properties compared to traditional materials. Composites can possess high strength, stiffness, and durability while also being lightweight. They can have improved resistance to corrosion, impact, and fatigue. Additionally, composite materials can have tailorable properties, allowing for customization to suit specific application requirements (Egbo, 2021). Figure 2.1 shows the schematic representation of FRP composites.

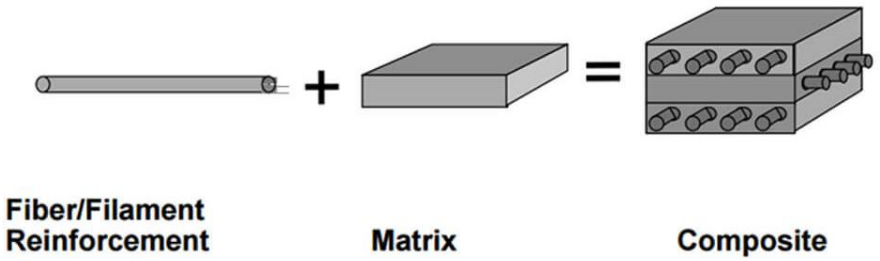

Fig. 2.1: Composition of composite materials (Peairs et al., 2004).

The history of composite materials spans centuries, with civilizations throughout time exploring the concept of combining different materials to create a new material with enhanced properties. However, the modern development and widespread use of composite materials can be attributed to significant advancements in the 20th century. In the early 1900s, researchers and engineers began experimenting with the incorporation of fibers, such as asbestos, into matrix materials to enhance their mechanical properties (Daniel and Ishai, 2005). These early attempts laid the foundation for the development of composite materials as we know them today.

One pivotal milestone in the history of composites was the invention of fiberglass in the 1930s by Russell Games Slayter and Dale Kleist, who discovered the reinforcing properties of glass fibers when mixed with a resin matrix. This breakthrough opened up new possibilities for the use of composites in various industries. During World War II, composites gained significant attention and were extensively used in military applications, such as aircraft components and radomes. The high strength-to-weight ratio and corrosion resistance offered by composites proved to be advantageous in these demanding environments (Daniel and Ishai, 2005).

Since then, the development of composite materials has continued to advance rapidly. New types of reinforcing fibers, such as carbon fibers, aramid fibers, and natural fibers, have been introduced, each offering unique properties suitable for specific applications. Matrix materials have also evolved, with thermosetting resins like epoxy and thermoplastics like polyetheretherketone (PEEK) becoming widely used in composite manufacturing (Dodiuk, 2013). In Figure 2.2 the historical evaluation of composite materials is presented.

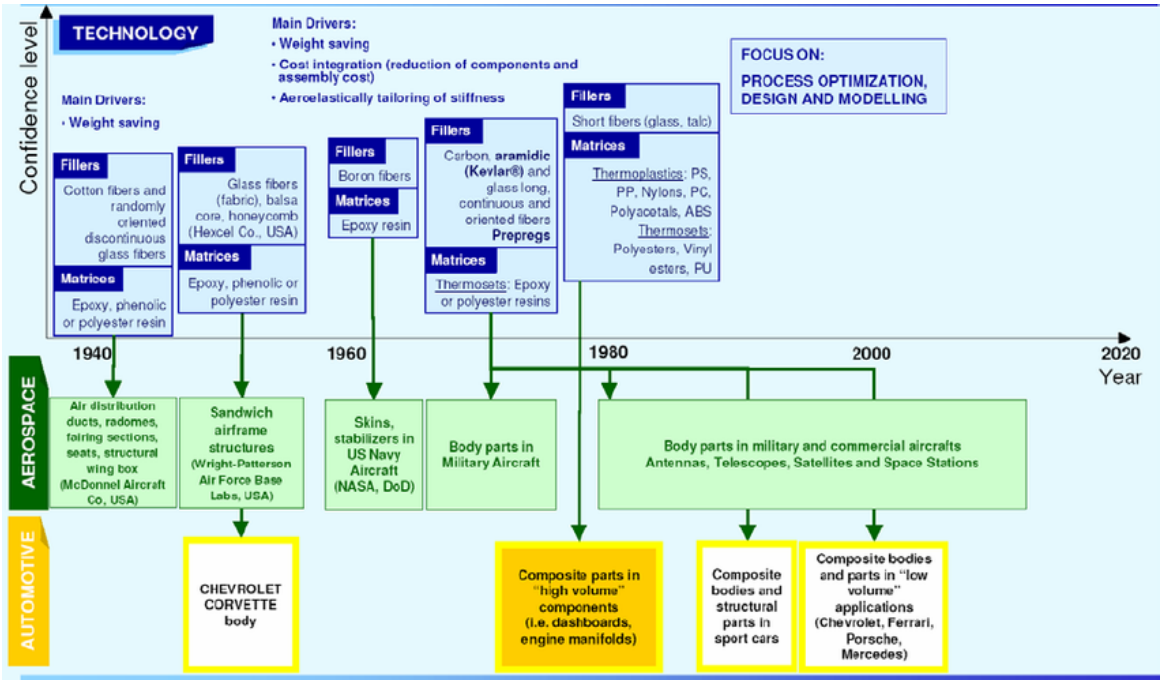

Fig. 2.2: Historical evolution of the composite materials (Kelly and Zweben, 1999).

To understand the significance and potential of composite materials, it is crucial to explore their various types and manufacturing processes. Polymer Matrix Composites (PMCs), Metal Matrix Composites (MMCs), and Ceramic Matrix Composites (CMCs) are some of

the prominent types of composites with unique characteristics and applications (Gibson, 2016). The fabrication of composites involves specific manufacturing processes tailored to each composite type, including layup, filament winding, compression molding, and sintering (Hull & Clyne, 1996).

2.2 Classification of Composite Materials

Composite materials consist of a matrix phase that binds and supports the reinforcement phase, resulting in a synergistic combination of properties. This literature review aims to provide an overview of different types of matrix materials used in composite materials, focusing on their composition, properties, and applications. The review aims to consolidate the findings from relevant studies and highlight the advancements made in understanding and utilizing various matrix materials in composite systems.

Polymer Matrix Composites: Polymer matrix composites (PMCs) are widely used due to their low density, excellent corrosion resistance, and ease of processing. The matrix phase is composed of a polymeric material, such as epoxy, polyester, or polyamide. These polymers offer a wide range of mechanical properties, including flexibility, toughness, and chemical resistance (Gibson, 2016). PMCs find applications in industries such as automotive, aerospace, and sporting goods.

Metal Matrix Composites: Metal matrix composites (MMCs) incorporate a metallic matrix phase, usually aluminum, magnesium, or titanium, with reinforcing elements such as ceramic particles or fibers. MMCs exhibit excellent mechanical properties, including high strength, stiffness, and thermal conductivity (Kelly and Zweben, 1999). These composites are utilized in applications requiring high strength-to-weight ratios, such as aerospace structures, automotive components, and electronic packaging.

Ceramic Matrix Composites: Ceramic matrix composites (CMCs) consist of a ceramic matrix phase, such as silicon carbide, alumina, or zirconia, reinforced with ceramic fibers or particles. CMCs offer exceptional high-temperature stability, excellent corrosion resistance, and low thermal expansion coefficients (Hegde et al., 2019). These materials are widely used in aerospace propulsion systems, heat exchangers, and thermal protection systems.

Carbon Matrix Composites: Carbon matrix composites (CMCs) utilize a carbon-based matrix material, such as carbon/carbon composites or carbon nanotubes, in combination with carbon fibers or other reinforcing materials. CMCs possess high strength, lightweight characteristics, and excellent thermal properties, making them suitable for applications in aerospace, defense, and high-performance industries (Hegde et al., 2019). These composites also exhibit good resistance to oxidation and wear.

Hybrid Matrix Composites: Hybrid matrix composites combine different types of matrix materials to leverage their unique properties. For example, combining a polymer matrix with ceramic particles or fibers can enhance the mechanical and thermal properties of the composite (Gibson, 2016). Hybrid matrix composites offer a balance of strength, toughness, and versatility, making them suitable for diverse applications in engineering and construction. Figure 2.3 a comparison of specific strength of different composite materials is shown.

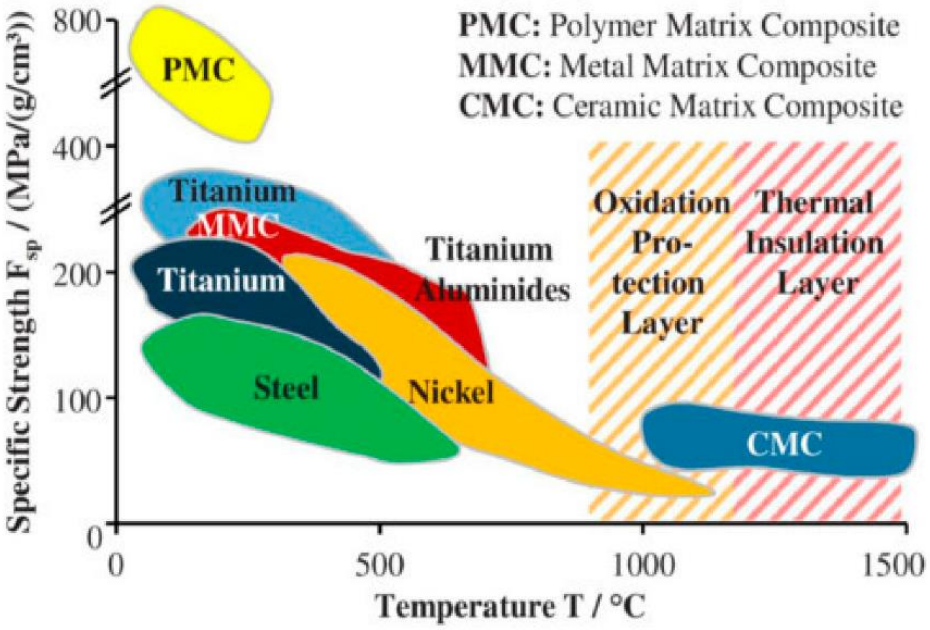

Fig. 2.3: Specific strength of aircraft engine materials as a function of temperature (Parveez et al., 2022).

Different types of matrix materials used in composite materials, including polymer matrix composites, metal matrix composites, ceramic matrix composites, carbon matrix composites, and hybrid matrix composites offer distinct advantages in terms of mechanical properties, thermal stability, and corrosion resistance. Polymer matrix composites excel in

versatility and ease of processing, while metal matrix composites offer high strength and thermal conductivity. Ceramic matrix composites provide excellent high-temperature stability, and carbon matrix composites combine lightweight properties with exceptional performance. Understanding the composition, properties, and applications of these matrix materials is crucial for the design and development of composite systems for various industries. This research work deals with Glass Fiber Reinforced Plastic Composites (GFRP) which is a type of Polymer matrix composites (PMC).

2.3 Glass Fibers

Glass fibers have become widely recognized as an essential component in composite materials, offering exceptional mechanical properties and versatility (Gibson, 2016). These fibers, composed of thin strands of glass, are commonly used as reinforcements in various industries due to their high tensile strength and durability (Hull & Clyne, 1996). Glass fibers are extensively employed in applications where lightweight materials with excellent mechanical performance are required.

The unique properties of glass fibers make them suitable for a wide range of industries, including aerospace, automotive, construction, and marine (Kelly and Zweben, 1999). In the aerospace sector, glass fibers are utilized in the fabrication of composite aircraft components such as wings, fuselage, and interior structures. Their lightweight nature contributes to weight reduction, leading to improved fuel efficiency and increased payload capacity. In the automotive industry, glass fibers are incorporated into composites to create lightweight panels, reinforcing structures, and interior components, resulting in enhanced fuel economy and reduced emissions. Figure 2.4 shows the unique properties of different types of glass fibers.

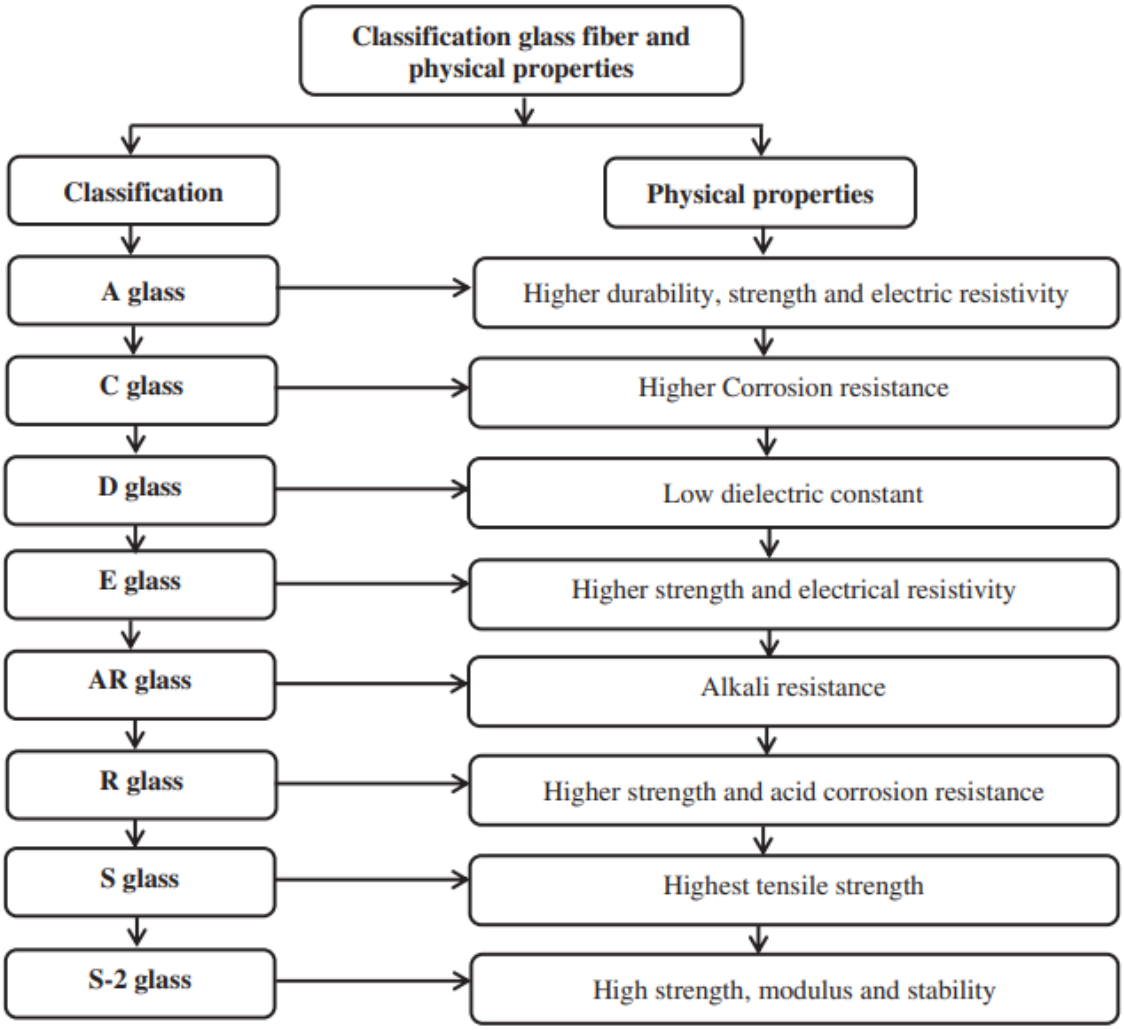

Fig. 2.4: Classification of glass fiber and physical properties (Sathishkumar et al., 2014).

The manufacturing process of glass fibers involves several stages, including melting, fiberization, and surface treatment (Hull & Clyne, 1996). The raw materials, typically silica sand, limestone, and soda ash, are melted together at high temperatures to form molten glass. This molten glass is then extruded through tiny orifices, which results in the formation of thin continuous strands of glass fibers. Surface treatment techniques are employed to enhance the adhesion between the glass fibers and the polymer matrix in composite materials. In Figure 2.5, different types of glass fibers are shown.

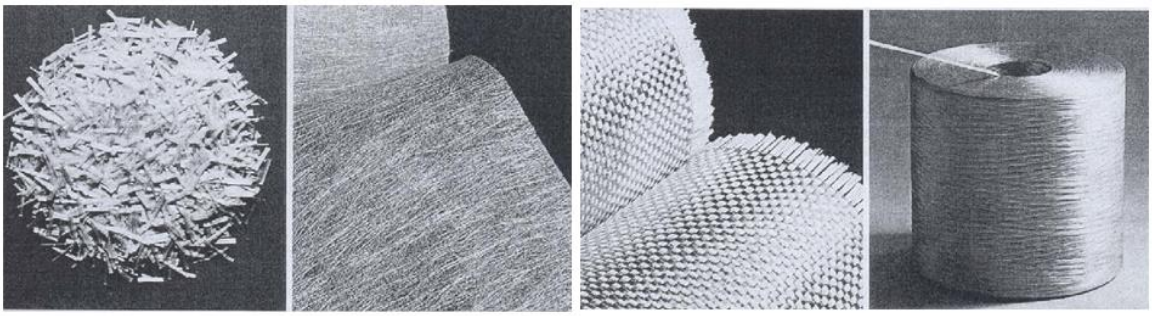

Fig. 2.5: Different types of glass fibers (Havenith, George, 1999).

Glass fibers are commonly incorporated into polymer matrix composites, where they act as the primary reinforcement. The glass fibers provide strength and rigidity to the composite structure, enhancing its mechanical properties. They are often combined with a matrix material, such as epoxy or polyester resin, to create a strong and durable composite material. Figure 2.6 shows the preparation of woven glass fiber cloth from glass fibers.

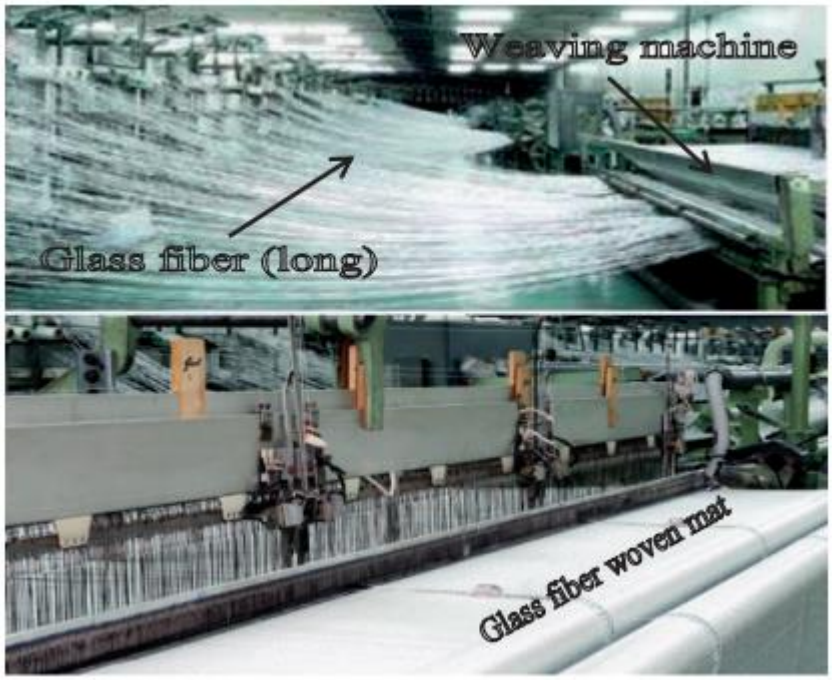

Fig. 2.6: Preparation of woven glass fiber mat (Sathishkumar et al., 2014).

The use of glass fibers in composites offers several advantages. Glass fibers have low density, making them lightweight and ideal for applications where weight reduction is important. They also exhibit good resistance to moisture, making them suitable for use in humid or corrosive environments. Glass fibers can be easily processed and molded into various shapes, allowing for versatility in design and manufacturing processes. Also, the

fiber orientation can be varied to create different types of glass fibers as shown in Figure 2.7.

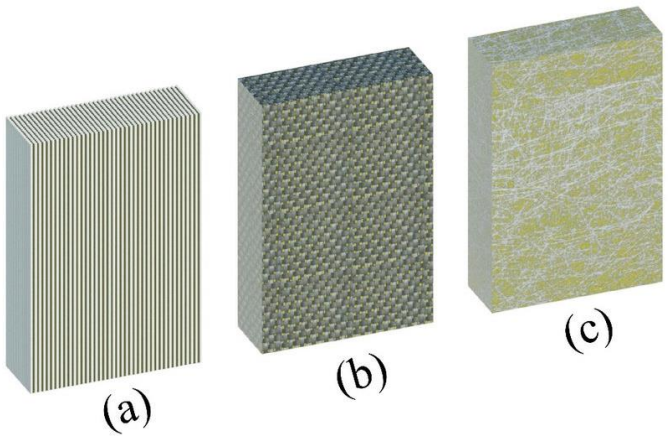

Fig. 2.7: Different types of GFRP laminates (a) Continuous unidirectional fibers, (b) continuous woven fibers and (c) random fibers (Bazli et al., 2019).

Research studies have extensively investigated the mechanical behavior and performance of glass fiber-reinforced composites. These studies have examined the effects of fiber content, orientation, and surface treatment on the composite's strength, stiffness, and fatigue resistance. The findings have contributed to the optimization of composite manufacturing processes and the development of tailored glass fiber composites for specific applications.

2.4 Epoxy Resins

Epoxy resins are a class of versatile thermosetting polymers widely used as matrix materials in composite applications. These resins are derived from the reaction between epoxide monomers and curing agents, resulting in a cross-linked and highly durable structure. Epoxy resins offer a combination of excellent mechanical properties, chemical resistance, and adhesion strength, making them suitable for various industries and applications.

Epoxy resins are known for their high strength and stiffness, making them an ideal choice for load-bearing applications. They exhibit a low shrinkage during curing, ensuring dimensional stability and minimizing the formation of internal stresses within the composite structure. Additionally, epoxy resins have excellent adhesion to a wide range of substrates, including metals, ceramics, and fibers, leading to strong interfacial bonding in composite materials (Kinloch, 1987).

The curing process of epoxy resins can be tailored to suit specific application requirements. By selecting different curing agents and adjusting curing conditions, the processing and mechanical properties of epoxy-based composites can be optimized. Epoxy resins are compatible with various reinforcement materials, including carbon fibers, glass fibers, and aramid fibers, enabling the production of high-performance composites with tailored mechanical characteristics (Balguri et al., 2021).

Research studies have extensively investigated the mechanical, thermal, and chemical properties of epoxy resin-based composites. These studies have focused on optimizing the resin formulation, curing parameters, and reinforcement configurations to enhance the overall performance of the composites. The findings have contributed to advancements in the development of epoxy-based composites for the aerospace, automotive, electronics, and construction industries (Tikhani et al., 2020).

2.5 Glass Fiber Reinforced Plastic (GFRP) Composites

Glass Fiber Reinforced Plastic (GFRP) composites have emerged as a prominent type of composite material, offering a unique combination of strength, stiffness, and corrosion resistance (Gibson, 2016). GFRP composites are composed of a polymer matrix, typically epoxy or polyester, reinforced with glass fibers (Hull & Clyne, 1996). The incorporation of glass fibers imparts exceptional mechanical properties to the composite, making it suitable for various applications. The use of GFRP composites has gained significant traction in industries such as aerospace, automotive, construction, and marine due to their lightweight nature and high strength-to-weight ratio (Kelly and Zweben, 1999). GFRP is being extensively used in the following industries.

Aerospace Industry: The aerospace industry extensively employs GFRP composites for their lightweight nature and high strength-to-weight ratio (Kelly and Zweben, 1999). GFRP composites are used in the manufacturing of aircraft components, including wings, fuselage sections, interior structures, and engine parts. These composites offer weight reduction, leading to improved fuel efficiency, increased payload capacity, and enhanced performance.

Automotive Industry: In the automotive sector, GFRP composites contribute to lightweight vehicle designs and sustainable transportation solutions (Kelly and Zweben, 1999). They are utilized in the fabrication of body panels, structural components, and interior parts. By incorporating GFRP composites, automakers can achieve significant weight reduction, resulting in improved fuel economy, reduced emissions, and enhanced crash performance. Construction Industry: GFRP composites find application in the construction industry for various structural elements (Gibson, 2016). They are utilized in the production of reinforcement bars, rebars, and grids. GFRP composites offer corrosion resistance, high strength, and durability, making them an ideal alternative to traditional steel reinforcement. Their use in construction enables longer service life, reduced maintenance costs, and improved resistance to harsh environmental conditions.

Marine Industry: The marine industry benefits from the use of GFRP composites in boat hulls, decks, and other marine structures (Hull & Clyne, 1996). These composites provide lightweight alternatives to traditional materials while maintaining strength and durability. GFRP composites offer resistance to water, chemicals, and UV radiation, making them well-suited for marine environments. Their utilization in marine applications leads to improved fuel efficiency and reduced maintenance requirements.

Sports and Recreation: GFRP composites have found extensive applications in the sports and recreation sector (Hull & Clyne, 1996). They are used in the production of sporting goods such as tennis rackets, golf clubs, bicycle frames, and fishing rods. The lightweight and high-strength properties of GFRP composites contribute to improved performance, increased maneuverability, and enhanced player experience in various sports.

2.6 GFRP in Aerospace

The application of GFRP composites across industries has revolutionized several sectors by offering lightweight, high-strength, and corrosion-resistant solutions. In aerospace, automotive, construction, marine, sports, and recreation industries, GFRP composites enable improved performance, fuel efficiency, sustainability, and cost-effectiveness. As research and development continue to enhance the properties and manufacturing techniques of GFRP composites, their significance in various applications is expected to grow, leading to further advancements in multiple industries.

(GFRP) composites have revolutionized the aerospace industry, offering lightweight and high-performance alternatives to traditional materials (Gibson, 2016). This article explores the extensive application of GFRP composites in the aerospace sector, highlighting their significance in aircraft components and their contributions to improved fuel efficiency, enhanced performance, and reduced maintenance requirements.

Wings and Fuselage: GFRP composites find extensive use in the manufacturing of aircraft wings and fuselage sections (Kelly and Zweben, 1999). The lightweight nature of these composites allows for significant weight reduction compared to conventional metallic structures. This weight reduction contributes to increased fuel efficiency, enabling aircraft to consume less fuel and reduce carbon emissions. Additionally, GFRP composites offer excellent strength-to-weight ratio and resistance to corrosion, enhancing the durability and longevity of the aircraft. Recently, the use of composite materials in aircraft is increasing significantly. Figure 2.8 shows an illustration of Boeing 787 aircraft which contains about 50% composite materials.

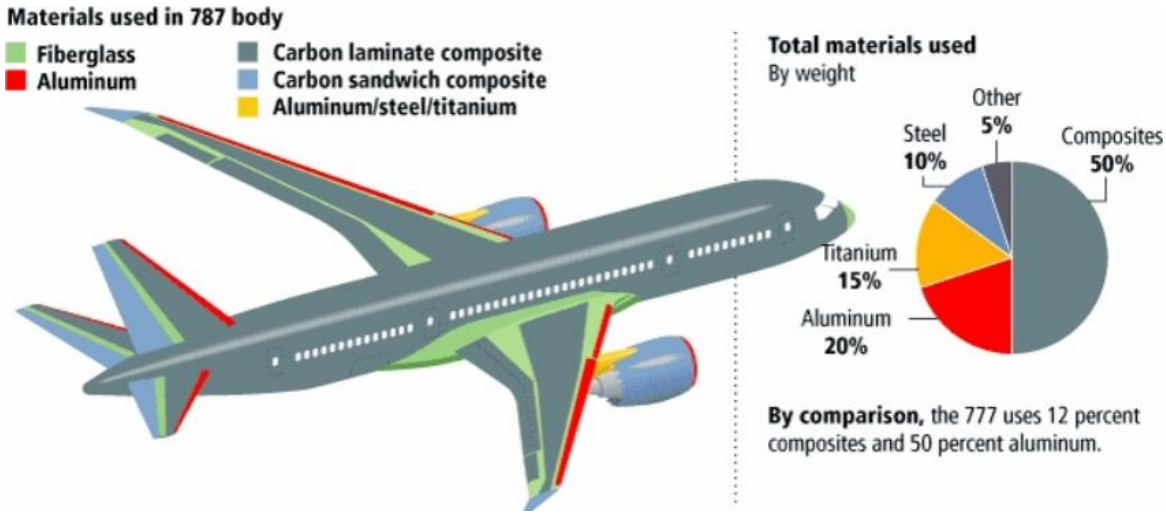

Fig. 2.8: Usage of composite materials in Boeing 787 (Peairs et al., 2004).

Interior Structures: GFRP composites are utilized in the construction of interior structures in aircraft, such as cabin panels, overhead compartments, and lavatory components. These composites provide a balance between weight reduction and structural integrity, ensuring passenger safety while maintaining fuel efficiency. Moreover, GFRP composites offer design flexibility, allowing for customized and aesthetically pleasing interiors. In Figure 2.9, GFRP components used in exterior components (not subjected to structural loads) of

ATR 72-212A aircraft is shown. It is worth mentioning that these components are exposed to up to -40 °C during flight.

Fig. 2.9: GFRP structural components in an ATR 72-212A aircraft.

Engine Components: GFRP composites play a crucial role in the manufacturing of engine components, including fan blades, nacelles, and thrust reversers (Gibson, 2016). The exceptional strength and heat resistance of these composites makes them suitable for demanding engine environments. By incorporating GFRP composites, engine manufacturers can achieve weight reduction, leading to improved overall aircraft performance and reduced fuel consumption.

Structural Reinforcements: GFRP composites are utilized as structural reinforcements in various aircraft components (Kelly and Zweben, 1999). They provide enhanced strength and stiffness, improving the structural integrity of critical areas such as landing gear, control surfaces, and structural joints. The use of GFRP composites in these applications contributes to increased safety, reduced maintenance costs, and extended service life.

(GFRP) composites have significantly impacted the aerospace industry, offering lightweight, high-strength, and corrosion-resistant solutions for aircraft components. Their application in wings, fuselage, interior structures, engine components, and structural reinforcements has resulted in improved fuel efficiency, enhanced performance, and reduced maintenance requirements. As research and development continue to advance the

properties and manufacturing techniques of GFRP composites, their significance in aerospace applications is expected to grow, leading to further advancements in aircraft design and performance.

2.7 GFRP Mechanical Properties

GFRP composites have gained significant attention in various industries due to their exceptional mechanical properties, making them a desirable material for high-performance applications. This literature review aims to provide an overview of the research conducted on the mechanical properties of GFRP composites, focusing on strength, stiffness, toughness, and fatigue resistance. The review aims to consolidate the findings from relevant studies and highlight the advancements made in understanding and optimizing the mechanical performance of GFRP composites. The Physical and mechanical properties of glass fibers depend on a lot of factors including the selection of fiber type, weave pattern and treatments. A general overview of the physical and mechanical properties of glass fibers in weight% is given in Table 2.1.

Table 2.1: Physical and mechanical properties of glass fibers (Sathishkumar et al., 2014).

Fiber	Density (g/cm^3)	Tensile strength GPa	Young's modulus (GPa)	Elongation (%)	Coefficient of thermal expansion ($10^{-7}/°C$)	Poison's ratio	Refractive index	Ref.
E-glass	2.58	3.445	72.3	4.8	54	0.2	1.558	17
C-glass	2.52	3.310	68.9	4.8	63	–	1.533	
S_2-glass	2.46	4.890	86.9	5.7	16	0.22	1.521	
A-glass	2.44	3.310	68.9	4.8	73	–	1.538	
D-glass	2.11–2.14	2.415	51.7	4.6	25	–	1.465	
R-glass	2.54	4.135	85.5	4.8	33	–	1.546	
EGR-glass	2.72	3.445	80.3	4.8	59	–	1.579	
AR glass	2.70	3.241	73.1	4.4	65	–	1.562	

Strength: Numerous studies have demonstrated the impressive strength characteristics of GFRP composites. The incorporation of glass fibers, known for their high tensile strength, significantly enhances the strength of the composite material (Hull & Clyne, 1996). Researchers have investigated various parameters, such as fiber orientation, fiber volume fraction, and matrix properties, to optimize the strength of GFRP composites. The findings indicate that higher fiber volume fractions and proper fiber alignment can lead to improved strength properties (Gibson, 2016).

Stiffness: The stiffness or modulus of elasticity is a critical mechanical property of GFRP composites. The reinforcing glass fibers provide excellent stiffness, enabling the composites to resist deformation under applied loads. Researchers have examined the effect of fiber type, fiber content, and matrix properties on the stiffness of GFRP composites (Kelly and Zweben, 1999). It has been observed that the use of high-modulus glass fibers and increased fiber content enhances the stiffness of the composites.

Toughness: The toughness of GFRP composites refers to their ability to absorb energy before fracture. Researchers have investigated the impact resistance and crack propagation behavior of GFRP composites, which are essential for applications subjected to dynamic loading or potential impacts. The incorporation of toughening mechanisms, such as interlayer toughening and hybrid fiber reinforcements, has been explored to enhance the toughness of GFRP composites (Gibson, 2016).

Fatigue Resistance: The fatigue resistance of GFRP composites is crucial in applications subjected to cyclic loading. Researchers have conducted fatigue tests to assess the endurance and durability of GFRP composites under repeated loading conditions. Factors such as fiber architecture, matrix properties, and environmental conditions have been investigated to understand their influence on the fatigue behavior of GFRP composites (Kelly and Zweben, 1999). It has been observed that the use of appropriate fiber architecture and matrix materials can significantly improve the fatigue resistance of GFRP composites.

There are several works found in the literature on the mechanical property testing of GFRP. The mechanical performance of FRP depends on the physio-mechanical properties of the individual constituents, i.e., fibers, matrix, fillers and their interface (Cs. Varga, N. Miskolczi, 2010). Suitable orientations and composition of glass fibers can produce GFRPs with desired characteristics and functional properties. GFRPs can be fabricated having greater stiffness than aluminum with less relative density than steel. The matrix of the composite decides the maximum operating temperature of the composite material (Morampudi et al., 2021). For high-performance applications in engineering, epoxy resins are most widely used as the matrix material among thermosetting plastics (Hameed et al., 2007).

Many researchers have been investigating the role of inorganic and organic fillers to enhance mechanical and tribological properties. Micro and Nanofillers like Al_2O_3, TiO_2, SiO_2, $Mg(OH)_2$, SiC, Carbon Nano Tubes (CNTs) and also various natural fillers have been added by researchers to augment the mechanical properties of GFRPs (Devendra and Rangaswamy, 2012; Dhawan et al., 2013; Nayak et al., 2014; Roustazadeh et al., 2020). (Ashrafi et al., 2020) examined the tensile characteristics of several GFRP laminates after being exposed to high temperatures. The test factors were laminate thickness, fiber arrangement, and exposure temperature. In general, it was found that as exposure time and laminate thickness increased, so did the rate at which the tensile strength was reduced. Following exposure to high temperatures, the results of tensile testing revealed that laminates with progressive unidirectional fibers outperformed those with chopped strands of randomly dispersed fibers, and laminates with woven continuous fibers performed in the middle. (Ratim et al., 2012) studied the effects of woven and non-woven kenaf fiber on the mechanical properties of polyester composites. They discovered that the composite's tensile strength was greatest for the twill weave pattern of fiber structure, while there was no significant difference between the mat structures and plain weave. (EL-Wazery et al., 2017) studied the effect of the percentage of glass fiber on the tensile strength, bending strength, and impact strength of GFRP in their research. The results revealed that adding more glass fibers by weight percentage significantly improved the mechanical properties of the composite that was created. The manufactured composites with 60-weight percent glass fiber had the best mechanical characteristics. (Alavudeen et al., 2015) investigated the impact of weaving patterns and random orientation on the mechanical properties of polyester composites reinforced with banana, kenaf, and banana/kenaf fibers. The hand lay-up technique was used to make composites with two different weaving types, namely plain and twill. In all the produced composites, the plain type outperformed the twill type in terms of tensile characteristics. Furthermore, plain woven hybrid composites rather than composites with random orientation showed the greatest gain in mechanical strength. (Almeida et al., 2015) investigated the interlaminar and in-plane shear characteristics of glass fiber reinforced epoxy composites as a result of the lay-up design. For this work, resin transfer molding with vacuum aid was used to create the following laminates: [0]5, [90]5, [0/90/0/90/0], and randomly oriented (mat). Due to its random fiber orientation, the mat samples displayed stronger in-plane shear strength in both tests compared to the [0]5laminate and [90]5 interlaminar shear strength. Due to the longitudinally oriented fibers, the composites [0]5 had a greater dynamic shear modulus than one might anticipate.

The literature review highlights the research conducted on the mechanical properties of GFRP composites, including strength, stiffness, toughness, and fatigue resistance. The findings from various studies indicate that the incorporation of glass fibers enhances the mechanical performance of the composites. Factors such as fiber orientation, volume fraction, matrix properties, and toughening mechanisms have been investigated to optimize the mechanical properties of GFRP composites. Further research is needed to explore advanced manufacturing techniques and innovative material combinations to further enhance the mechanical performance of GFRP composites in different applications.

2.7 Machining of GFRP

Machining of GFRP presents unique challenges due to the heterogeneous nature of the composite material. GFRP consists of a matrix, typically epoxy resin, reinforced with glass fibers. The presence of glass fibers significantly impacts the machining process and requires careful consideration to ensure optimal results.

When machining GFRP, the main objective is to cut through the composite material while minimizing damage to the fibers and maintaining dimensional accuracy. However, the hardness and abrasive nature of the glass fibers can cause excessive tool wear, leading to reduced machining efficiency and compromised surface finish. In Figure 2.10, FRP composite surface failures resulting from different machining techniques are shown.

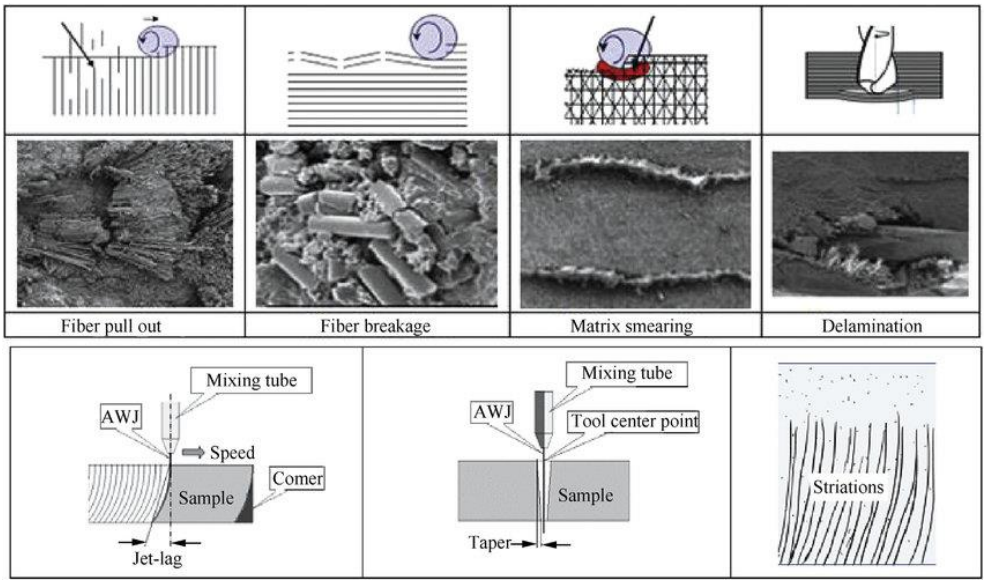

Fig. 2.10: Surface failures resulting from machining of FRP with different cutting tools (Altin Karataş and Gökkaya, 2018).

Several machining techniques are commonly employed for GFRP, including milling, drilling, turning, and grinding. The selection of the machining method depends on the specific requirements of the application and the desired outcome. Machining parameters such as cutting speed, feed rate, depth of cut, and tool material play a crucial role in achieving satisfactory results (Biermann, 2016).

Due to extensive use, the machining of GFRP has received widespread attention among researchers. It is a very important consideration and different processes are needed to be explored to impart high surface quality, good dimensional accuracy and less alteration of mechanical properties. To address the challenges associated with GFRP machining, researchers have conducted extensive investigations into the optimization of machining parameters and tool selection. Studies have explored the influence of various factors, such as fiber orientation, cutting tool geometry, and cooling strategies, on the machinability of GFRP (Negarestani & Li, 2012; Saad et al., 2020). Advanced machining techniques, such as ultrasonic machining and laser machining, have also been explored to overcome the limitations of conventional machining methods when dealing with GFRP (Slamani and Chatelain, 2023). These techniques offer advantages such as reduced tool wear, improved precision, and better surface finish.

Laser beam machining being a non-contact and virtually force-free manufacturing method is a preferable alternative means of cutting FRP composites. Laser cutting is a thermal process that focuses a laser beam to melt and vaporize material in a localized area (Fatimah et al., 2012). Machining of GFRPs or FRPs in general is a challenging task and different from that of metals due to their low thermal conductivity, heat sensitivity and anisotropic behavior (El-Hofy et al., 2011). In the case of laser machining, these considerations are even more acute and need sound technical investigation to achieve good results. Several researchers have explored different laser drilling/cutting parameters including laser intensity, cutting speed and gas pressure to achieve minimum surface roughness (Ra), heat-affected zone (HAZ), taper angle (TA), and maximum tensile strength (TS) of the laser-drilled glass fiber-reinforced plastic (GFRP) laminate (Solati et al., 2019). (Rose et al., 2020) investigated how the mechanical characteristics of CFRP were affected by the remote-laser beam cutting technique. The findings of the present investigation demonstrate that, in comparison to test specimens made from milling, the maximal tensile stress decreases when the HAZ expands to an unreasonable degree. (Harada et al., 2012)

experimented on the impact of various cutting techniques on the static tensile strength and the fatigue strength of CFRP. The CFRP was cut using a CO2 gas laser, a single-mode fiber laser, an abrasive water jet, and a conventional mechanical device. High-quality cuts were made by the mechanical cutting specimen. The heat-affected zone (HAZ) was clearly visible in the laser-cutting specimens. When compared to mechanical or water-jet cut specimens, the static tensile strength and fatigue strength of specimens created by laser cutting was significantly reduced. The specimen created by laser cutting showed a linear dependence of the tensile strength on the HAZ, showing that the primary effect was caused by the thermal degradation of CFRP inside the HAZ. Choudhury and Chuan, investigated the quality of glass fiber-reinforced plastic surfaces cut by single-pass and double-pass laser beams. The input laser variables were the nozzle diameter, material thickness, and cutting speed, while the outputs were the surface roughness and kerf width at the irradiation and exit sides. According to the findings, a double-pass laser beam appeared to generate cut surfaces of a significantly higher quality than a single-pass laser beam. Hirsch et al. investigated the single mode fiber laser cutting of a composite with glass fiber reinforcement (PA6/GF60) and a composite with carbon fiber reinforcement (PA6/CF60). Both were continuous fiber-reinforced thermoplastic composites (TPC) with polyamide6 (PA6) matrix and fiber content of 60 weight percent of these materials was investigated. By using optical microscopy and uniaxial tensile testing to analyze the HAZ and mechanical characteristics of the laser-cut composites, it was revealed that there was anisotropy and a dependence on the laminate structure. The obtained mechanical properties of the laser-cut composites, however, were discovered to be on par with those of their water jet-cut counterparts. Rahman and Rahman, studied the laser cutting effect of woven glass fiber reinforced plastic composites. They found mechanical cutting to be superior than laser cutting in terms of tensile, flexural and Vickers microhardness propertiesThe reason being thermal damage in laser cutting.

According to available research, laser cutting affects the mechanical performance of FRP components. The reason is the formation of a HAZ, whose development is dependent on the laser cutting circumstances. Modifications to the laser cutting parameters may affect mechanical performance (Rose et al., 2020). However, studies on the comparative effect of mechanically cut and laser cut on the mechanical performance of GFRPs or even FRPs, in general, are very seldom. The closest to our experiment is research on the evaluation of the cutting process on the tensile and fatigue strength of CFRP composites (Harada et al.,

2012), which found that the static tensile strength and the fatigue strength by laser cutting specimens decreased in comparison with mechanical or water-jet cutting specimen. Moreover, the laser cutting specimen exhibited a linear dependency of the tensile strength on the heat-affected zone (HAZ), indicating that the main effect resulted from the thermal destruction of CFRP within the HAZ.

The research in GFRP machining aims to optimize the process parameters to enhance productivity, reduce costs, and minimize damage to the composite material. By understanding the interaction between the cutting tool and the composite structure, manufacturers and engineers can develop effective machining strategies for GFRP components used in industries such as aerospace, automotive, and marine.

2.8 Thermal Aging of GFRP

Thermal aging is a critical factor that can significantly impact the performance and reliability of various materials, particularly those exposed to high temperatures for extended periods. This literature review aims to provide an overview of research conducted on the thermal aging of materials, focusing on the effects of elevated temperatures on their mechanical, thermal, and chemical properties.

Glass Fiber Reinforced Plastic (GFRP) composites are widely used in various industries due to their excellent mechanical properties and corrosion resistance. However, their long-term performance under thermal aging conditions is a critical concern. This literature review aims to provide an overview of research conducted on the thermal aging of GFRP composites, focusing on the effects of elevated temperatures on their mechanical, thermal, and chemical properties. The review aims to consolidate the findings from relevant studies and highlight the challenges and advancements in understanding the thermal aging behavior of GFRP composites.

Effect on Mechanical Properties: Several studies have investigated the influence of thermal aging on the mechanical properties of GFRP composites. Researchers have conducted tensile, flexural, and impact tests to evaluate changes in strength, stiffness, and toughness after exposure to elevated temperatures. The findings indicate that prolonged thermal aging can lead to a decrease in mechanical properties, including reductions in tensile strength, stiffness, and impact resistance (Huang et al., 2018; Ouedraogo et al., 2020). The

degradation mechanisms include matrix degradation, fiber-matrix interface debonding, and fiber damage.

Thermal Properties: Thermal aging can also affect the thermal properties of GFRP composites. Researchers have examined changes in thermal conductivity, coefficient of thermal expansion (CTE), and glass transition temperature (Tg) after exposure to elevated temperatures. It has been observed that thermal aging can result in increased thermal conductivity, higher CTE, and a shift in the Tg of the composite material (Song et al., 2021; Kim et al., 2017). These changes can impact the dimensional stability and thermal performance of GFRP composites under thermal loading conditions.

Chemical Degradation: In addition to mechanical and thermal property changes, thermal aging can cause chemical degradation of GFRP composites. Researchers have studied the effects of elevated temperatures on the chemical composition, degradation of the polymer matrix, and fiber-matrix interfacial bonding. The findings indicate that thermal aging can lead to the degradation of the polymer matrix, including chain scission, oxidation, and crosslinking reactions (Song et al., 2021; Huang et al., 2018). The chemical changes can affect the overall performance and service life of GFRP composites.

Regarding the thermal aging of GFRPs and its influence on mechanical properties, a considerable amount of literature has been published. Bazli et al. investigated the behavior of unidirectional, woven, and chopped strand GFRP laminates subjected to impact and flexure loads at extreme temperatures. According to the findings, GFRP laminates' flexural and impact capabilities generally deteriorate as exposure time and temperature rise, and as laminate thickness decreases. Kun et al. developed an epoxy glass fiber composite and performed wet and heat cycle aging tests. They found that the composites' mechanical and dielectric properties deteriorated over time. Zuo et al. performed an experiment in which the isothermal and non-isothermal crystallization behaviors of glass fiber-reinforced polyphenylene sulfide were rigorously investigated and a broad variety of widely used models were applied to this material. It was discovered that the polymer crystallizes more slowly during crystallization when it has undergone extreme age and degeneration. According to Birger et al., thermal aging influences the mechanical characteristics and failure processes of graphite-fabric epoxy composites exposed to flexural stress. The authors thermally aged the samples at 170 °C for 120, 240, and 626 hours. For the longest

exposure period, bare fibers were detectable due to the weakening of the fiber-matrix interface, and as thermal aging progresses, fracture transforms from ductile with more plastic deformations to brittle. Mouritz et al. investigated the post-fire residual flexure strength of glass, carbon, and Kevlar-reinforced polyester, epoxy, and phenolic-based laminates. They discovered that even a little amount of fire damage resulted in a significant decrease in strength qualities, and the model used to forecast the strength properties showed a strong connection with the experimental data. Dodds et al. subjected the epoxy, phenolic, and polyester GFRP panels to a high-temperature fire and compared the behavior using thermal modeling. Phenolic-based GFRP laminates were shown to be more susceptible to delamination. In addition, the thickness of the composites had a significant effect in their fire resistance. (Jafari et al., examined the behavior of unidirectional, woven, and randomly dispersed (chopped strand mat) laminate specimens at elevated temperatures. The type of fiber, temperature, and laminate thickness was the test variables. The results demonstrated that an increase in temperature had the greatest impact on the specimens among the parameters. At 550°C, the unidirectional laminate specimens performed the best, retaining about 40% of their load capacity. The laminate specimens with randomly distributed fibers lost all of their strength at 400°C, while the woven laminate specimens were unable to support any tensile loads at this temperature.

The glass transition temperature (Tg) is an important consideration for the thermal aging study of all FRPs. Zavatta et al. conducted research to determine how the strength of carbon fabric/epoxy composites changed as a result of thermal aging in air. For aging at temperatures below the glass transition temperature (Tg) of the resin, a considerable decline in strength was observed. In contrast, a fast drop in strength was found at aging temperatures exceeding Tg. Furthermore, it was determined that even brief exposure to operating temperatures over Tg might significantly reduce the load-bearing capacity of CFRP components.

Several researchers have also noted the color changes due to thermal aging. (Lan et al., 2022) studied the color changes and mechanical properties of glass fiber-reinforced polycarbonate (GF-PC) composites after aging at various temperatures. The experiment revealed that the brightness of the GF-PC composite is related to trends detected in their tensile strength and bending strength. Song et al., investigated the impact of thermal aging on the mechanical properties of glass-reinforced PEI plate composites. They found that as

the aging temperature increased from 80 to 145°C, both the tensile and flexural strengths of the GF/PEI composite samples dropped, which was also reflected in their color difference. In Figure 2.11, the interior GFRP components of an ATR 72-212A aircraft subjected to thermal aging are shown. Their distinctive color change is notable.

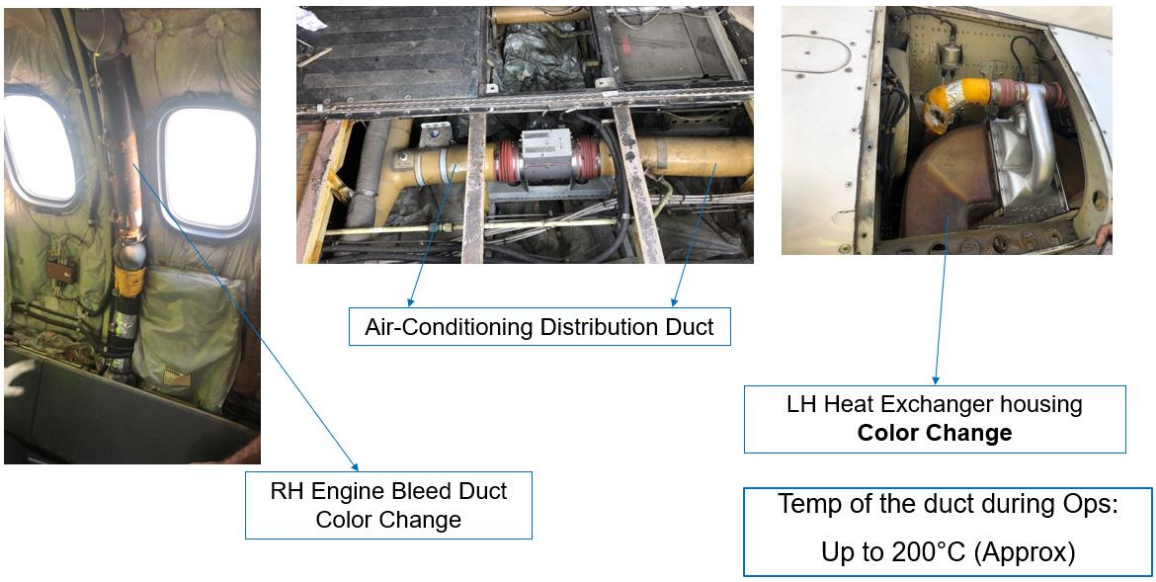

Fig 2.11: GFRP color change due to thermal aging in ATR 72-212A aircraft.

To mitigate the negative effects of thermal aging, researchers have explored various strategies. These include incorporating thermally stable matrix materials, utilizing advanced fiber-matrix interfacial bonding techniques, and employing protective coatings or additives to enhance the thermal stability of GFRP composites (Ouedraogo et al., 2020; Sun et al., 2021). These approaches aim to improve the resistance of GFRP composites to thermal aging and extend their service life in high-temperature environments.

The literature review highlights the research conducted on the thermal aging of GFRP composites, focusing on the effects of elevated temperatures on their mechanical, thermal, and chemical properties. The findings indicate that thermal aging can lead to degradation in mechanical properties, changes in thermal behavior, and chemical degradation of the composite material. Mitigation strategies have been explored to enhance the thermal stability and extend the service life of GFRP composites under thermal aging conditions. Further research is needed to develop robust and reliable techniques for the design and manufacturing of GFRP composites with improved thermal resistance and durability.

2.9 Glass Transition Temperature

The Glass Transition Temperature (Tg) is a critical parameter in understanding the thermal behavior of GFRP composites. Tg refers to the temperature at which the polymer matrix transitions from a glassy, rigid state to a rubbery, more flexible state. It is an essential characteristic that influences the mechanical, thermal, and processing properties of GFRP composites.

The determination of Tg is crucial for selecting appropriate operating conditions and ensuring the long-term stability and performance of GFRP components. Several experimental techniques, such as Differential Scanning Calorimetry (DSC) and Dynamic Mechanical Analysis (DMA), are commonly employed to measure the Tg of GFRP composites (Bishay et al., 2017; Sehrawat et al., 2022). Knowledge of the Tg of GFRP composites aids in material selection, process optimization, and component design, ensuring that the composite can withstand the intended service conditions. By accurately determining and considering the Tg, engineers and manufacturers can produce GFRP composites with superior thermal performance and durability.

The Tg of GFRP composites depends on various factors, including the polymer matrix, fiber content, fiber orientation, and the presence of additives or fillers. Generally, the addition of glass fibers to the polymer matrix increases the Tg of the composite due to the reinforcing effect of the fibers (Nassar & Nassar, 2020). Figure 2.12 shows a general illustration of Tg of a material by plotting the stiffness vs temperature. It is noteworthy that beyond the Tg temperature, the material transitions into a rubbery state.

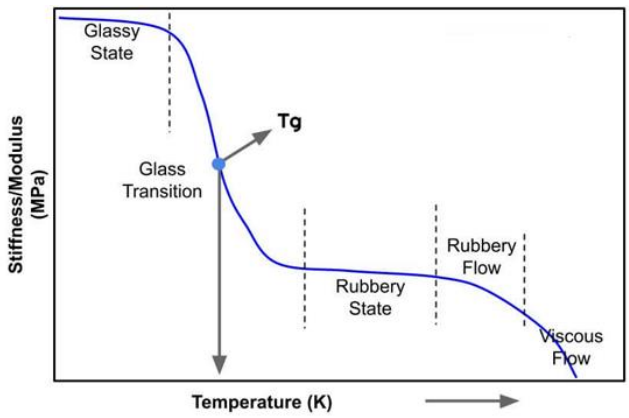

Fig 2.12: An illustration of Tg plotting the temperature and stiffness (Polanský et al., 2009).

Understanding the Tg of GFRP composites is essential for designing and manufacturing components that can withstand the anticipated operating temperatures. Operating a GFRP composite above its Tg can lead to a significant reduction in mechanical properties, dimensional stability, and even structural failure.

To optimize the performance of GFRP composites, researchers have investigated methods to improve the Tg and thermal stability of the composite materials. Strategies such as modifying the polymer matrix, using hybrid reinforcement systems, and incorporating nanofillers have been explored to enhance the Tg and thermal resistance of GFRP composites (Seydibeyoğlu et al., 2023).

2.10 Predictive Modeling

Predictive modeling of thermally aged Glass Fiber Reinforced Plastic (GFRP) composites plays a vital role in understanding the long-term behavior and performance of these materials under elevated temperature conditions. Thermal aging refers to the degradation and changes that occur in the composite structure when exposed to high temperatures over extended periods.

The development of predictive models for thermally aged GFRP composites is crucial for industries that rely on these materials, such as aerospace and automotive. By utilizing these models, engineers can assess the long-term durability and performance of GFRP components, optimize maintenance schedules, and make informed decisions regarding material selection and design modifications.

Predictive models are well suited for FRP composites due to their non-homogeneous nature of microstructure arrangement (Cai and Jin, 2018). Generally, upon close examination of FRP microstructure, manufacturing-level defects are observed. The most common defects are fibers without any matrix in between, uneven spacing, epoxy pockets which are empty voids that the epoxy did not fill and air entrapment. Figure 2.13 shows this nonhomogeneous microstructure arrangement of FRPs.

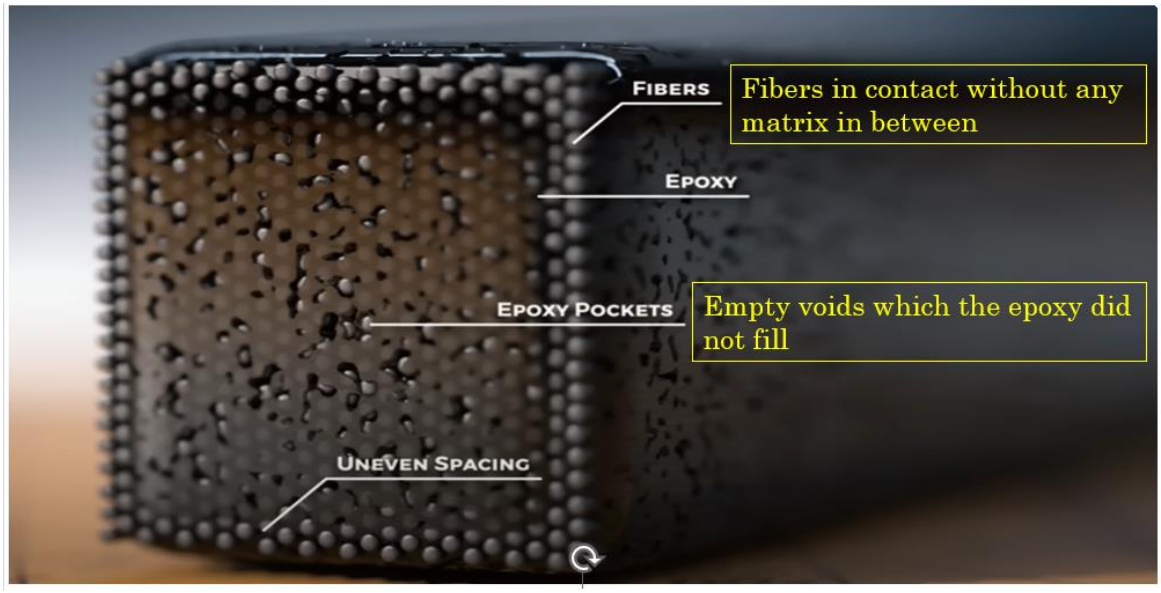

Fig. 2.13: Nonhomogeneous microstructure of FRP ("The Questionable Engineering of Oceangate," 2023).

All these defects combinedly create a random arrangement of microstructure arrangement which makes traditional Finite Element Method (FEM) analysis less effective. This is because FEM analysis relies on mathematical modeling of a finite element of the material and integrating it over different boundary conditions. Although it can be mentioned that FRPs fabricated in good quality controlled manufacturing facilities have a negligible amount of defects as discussed above. In addition, autoclave curing further removes any air bubbles within the matrix. However, these are very high-level manufacturing techniques that are used only for very sensitive applications. For general manufacturing techniques like the hand layup method which is used for this study, the possibility of the defects as discussed above remains very much a concern. Hence, data-driven predictive models are of more interest in general for FRPs. Also, with the rise in computing power, availability of cross-platform data and advancement in data mining technologies, data-driven predictive models have gained the attention of researchers.

To accurately predict the effects of thermal aging on GFRP composites, various modeling approaches have been developed and applied. These models aim to simulate the degradation mechanisms, mechanical property changes, and microstructural evolution that occur during thermal aging. One commonly used modeling technique is finite element analysis (FEA), which employs mathematical algorithms to simulate the behavior of complex structures. FEA can be utilized to predict the mechanical properties, such as stiffness and strength, of thermally aged GFRP composites based on inputs such as

temperature, time, and material properties (Karuppannan Gopalraj and Kärki, 2021). Another approach is the development of empirical models based on experimental data. Researchers have conducted extensive testing to characterize the mechanical properties of GFRP composites before and after thermal aging. By analyzing the experimental data, empirical models can be derived to predict the degradation of specific properties, such as tensile strength or flexural modulus, as a function of aging time and temperature (Shalaby et al., 2018).

The literature review suggests thorough experimentation by different researchers combining different new and old approaches to get increasingly higher accuracy. Gibson et al. studied raised temperature effect on the mechanical properties of woven glass fiber/polypropylene composites and suggested a 3-parameter model to define the tensile behavior and a 2-parameter model to define the compressive behavior to analyze the effects. Kim et al. experimented with multiple regression analysis (MRA) and polynomial regression analysis (PRA) and ANNs, to analyze the factors affecting the tensile strength of basalt and glass fiber-reinforced polymers (FRPs). They found that ANNs could be the most efficient model for forecasting the durability of FRPs. Gayatri Vineela et al. performed an experiment in which the ultimate tensile strength of hybrid short fiber composites comprised of glass fiber, carbon fiber, and epoxy resin is predicted utilizing artificial neural network approaches. It was discovered that ANN can predict the values of tensile strength more precisely than the regression model. Mishra et al. conducted an experiment to demonstrate a MATLAB-based artificial neural network (ANN)-based approach for forecasting the deflection behavior of three kinds of beams: plain, steel-reinforced, and bamboo-reinforced beams. The findings demonstrate that the ANN is a potent and trustworthy technique for evaluating the deflection behavior of concrete beams under the studied loading circumstances. Doblies et al. have developed a model to predict the mechanical properties, as well as the thermal exposure time and temperature of epoxy resin, using Fourier-transform infrared spectroscopy (FTIR)-spectroscopy, data processing, and artificial neural networks. Turco et al. developed two Artificial Neural Networks (ANNs) in order to forecast the compressive (ANN1) and tensile (ANN2) strengths of natural fiber-reinforced CEBs. The correlation coefficients (R-values) for ANN1 and ANN2 were 0.97 and 0.91, respectively, demonstrating the great accuracy of their generated tools.

The ongoing research in predictive modeling of thermally aged GFRP composites aims to improve the accuracy and reliability of these models. By further refining the understanding of degradation mechanisms and incorporating advanced modeling techniques, researchers strive to provide valuable tools for predicting the behavior of GFRP composites throughout their service life.

In recent years, there has been an increasing interest in the use of data-driven modeling techniques, such as machine learning and artificial neural networks, to predict the effects of thermal aging on GFRP composites. These models utilize large datasets of experimental results to establish relationships between aging parameters and material properties, enabling accurate predictions of the composite behavior under different aging conditions (Zhang et al., 2023; Fazilat et al., 2012). These recent advancements in ANN and AI technologies have motivated the author to investigate the feasibility of developing the predictive model based on the discussed technologies. Although there are other techniques used in the predictive model like Image Processing and Regression Analysis; ANNs being a specialized and vast topic on its own, a theoretical background on the same has been incorporated.

2.11 Artificial Neural Networks

Neural networks and deep learning are trending topics in the realm of computer science and technology. Since the beginning of this century, the world has seen many developments in machine learning algorithms. Such algorithms are extremely complex and are often used for doing things that were thought to be impossible even as little as 40 years ago. Things like recognizing a face in a stadium full of thousands of people, driving a car through 9am traffic, playing chess with renowned grandmasters etc. are some of the accomplishments people have achieved with artificial intelligence and machine learning technology. This wonderful technology is modeled after probably the most complex object in the world that we often take for granted, and that is our brain.

The billions of neurons that make up the entire brain are interconnected in an endless web of complexity. There are roughly 1014–1015 of these connections, known as synapses, in a single brain. Most of the time, they allow humans to learn from nature, adapt to it, and gain control of it. A neuron's fundamental form consists of a cell body with a few tiny branches attached to it. These branches are known as dendrites. The axon, a long, unique

item that resembles a wire and is joined to the cell body, is another component. Information is transmitted from the cell body to the next neuron via the dendrites of the axon. This connection between the two neurons is called a synapse. After we are born, we start to learn both consciously and subconsciously.

Our brain receives data from our nerve endings and uses connections between neurons to analyze or recall them. Most of the time, walking does not require us to pay much attention to it. We don't calculate each step and perform the required activities. When we were taught to walk as children, our brains had to acquire the technique after numerous futile efforts. Our brain's synapses "remember" these unsuccessful attempts and change the way our leg muscles work so that we can continue walking without falling. It should come as no surprise that Artificial Intelligence, the force behind modern technology, is based on what is considered to be the most sophisticated system to man—our brain (Doblies et al., 2019).

2.11.1 Basic Structure of Nural Networks

Similar to the brain, neurons are a basic component of a neural network. It takes in data from the preceding neurons, analyses it, and then delivers it to the subsequent neuron. As shown in Figure 2.14, information from the prior neurons is received as numerical values (x0, x1, x2, etc.). The "weights" (w0, w1, w2, etc.), which are still another set of numerical values allocated to the connections, are multiplied by these. The cell body then adds up and processes the multiplied values of these weights (w0, w1, w2, etc.) and input values (x0, x1, x2, etc.), together with another numerical value assigned to each neuron, called the bias (b), using an activation function. The following neuron receives the processed value after that. A comparison of biological neurons with ANNs and their synapse is shown in Figure 2.14.

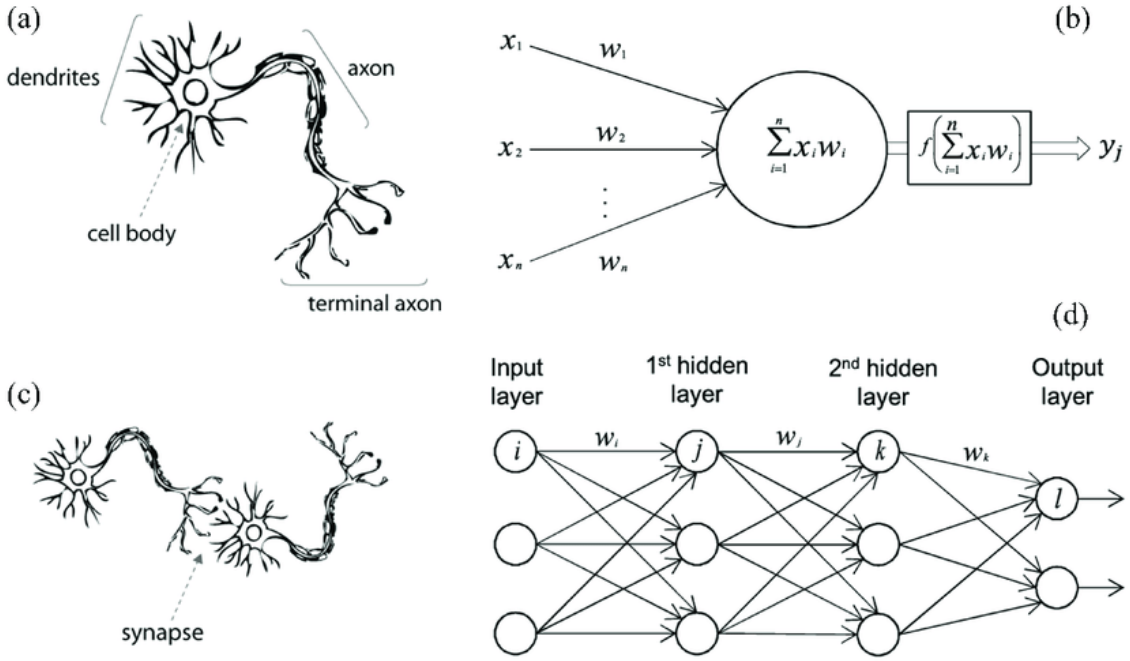

Fig. 2.14: A biological neuron in comparison to an artificial neural network (a) human neuron, (b) artificial neuron, (c) biological synapse and (d) ANN synapses (Meng et al., 2020).

Several activation functions are used to get output from each neuron. Purelin function, Sigmoid function, hyperbolic tan (tanh) and rectified linear unit (ReLU) are some of the most widely used activation functions in neural networks. Purelin and Sigmoid functions have been used as activation functions in this research.

2.11.2 Types of Neural Networks

There are many types of neural networks and each of them have their applications along with a set of advantages and disadvantages. The models that are mostly used include:

Feedforward fully connected neural network: A feedforward fully connected neural network is a type of artificial neural network in which there are no cycles, or repetitions of connections between the neurons. In this network, information only flows in one direction through the neurons. Information travels from the input neurons in the input layers, via the hidden nodes in the hidden layer (if any), and to the output nodes in the output layer during the forward stroke or forward movement of data. No neuron's output becomes an input to the neuron that came before it. Similarly, during training of the network, the network parameters are updated sequentially in a reverse direction. This starts from the output layer,

goes through all the hidden layers and ends with the input layer. The input layer takes input and the output layer generates output. Each neuron in each layer is connected to all the neurons in the previous layer; hence, the name is “Fully connected neural network”. In a feedforward fully connected neural network, the connections between the neurons do not recur, or, to put it another way, there are no cycles. In this network, information travels only one way through the neurons. The input neurons in the input layers send information to the output nodes in the output layer via the hidden nodes in the hidden layer, if any, during the forward stroke or forward movement of data. Any neuron's output is not ultimately used as an input by the neuron that comes before it (Le, 2020; Kim and Oh, 2021).

Convolutional neural network: Different principles govern how convolutional neural networks operate. Usually, these networks are applied to image categorization issues. Convolution neural networks do not have fully connected neurons or nodes, in contrast to fully connected neural networks. Not all pixels are connected to the network's next layer when dealing with image classification difficulties, and the input neurons reflect the color value of the pixels that make up the image. Instead, the image is split up into different areas, each of which has a separate connection to a node in the layer below. The output layers and the outermost concealed layers are both fully connected layers (Kim and Oh, 2021).

Recurrent neural network: In recurrent neural networks, the neurons or nodes in one layer and the layer before it are directly connected. In recurrent networks, which differ from feedforward networks in which information only travels in one direction, cycles can be visible at various stages of the network, allowing the network to feed information straight from a given layer to its previous layer. These networks are frequently used to forecast power demand in global electric grid systems (Kim and Oh, 2021).

2.11.3 Activation Functions

The mathematical modeling of neural networks also has features that replicate the brain and enable a neuron to "fire," or transfer data from one neuron to another, using the notion that a neuron can "fire" or transmit information from one neuron to another within our brain. The fact that these neurons are interconnected causes the data to flow from one neuron to the next to form a complex network chain, allowing the network as a whole to be described in a way that allows it to recall input values and recreate which neurons to fire. The

processes known as activation functions are those that cause neurons to fire. In neural networks, a variety of activation functions are employed. Some of the most used activation functions are shown in Figure 2.15.

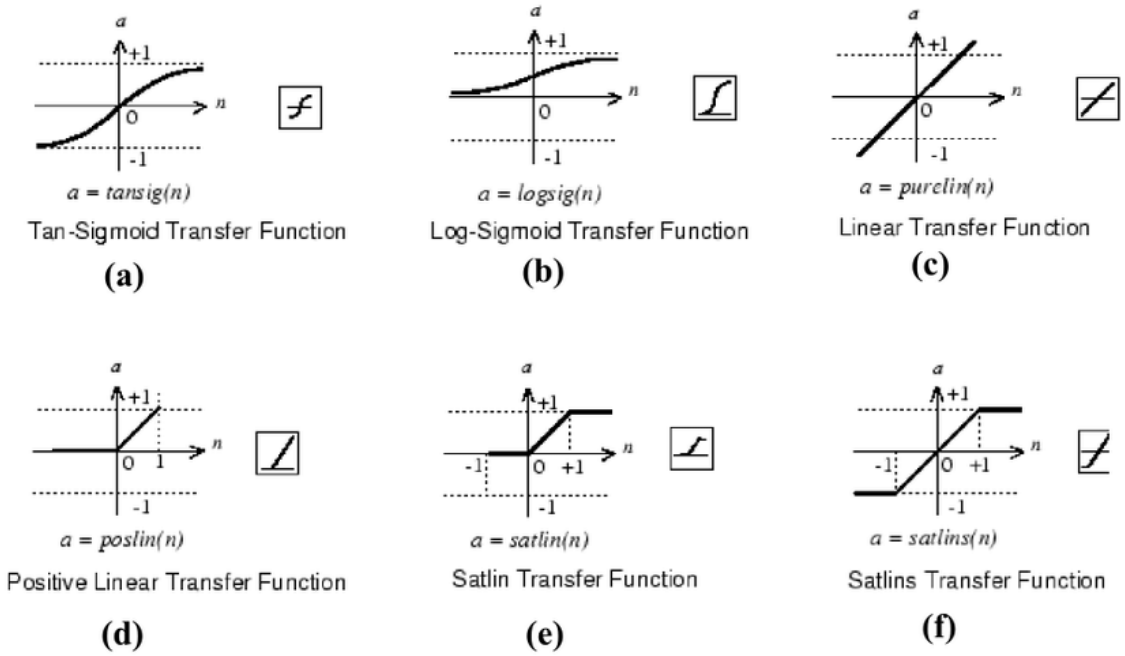

Fig. 2.15: Commonly used activation functions (a) tansig, (b) logsig, (c) purelin, (d) rectilin, (e) satlin and (f) satlins (Le, 2020).

Sigmoid function: The sigmoid function is a well-known mathematical function that can take any numerical value and output a value ranging from 0 to 1. The sigmoid function can be written as (Meng et al., 2020):

$$sigmoid(x) = \frac{1}{1 + e^{-x}} \tag{2.1}$$

The key benefit of utilizing a sigmoid activation function is that it consistently generates an output in the range of 0 to 1. All of the neurons in all of the network's layers can have a controlled and effective flow of information thanks to this data processing. In classification issues, when the output neurons just need to produce a number close to 0 or 1 to reflect the input data being classified between various classes, sigmoid functions play a significant role. A neural network, which is intended to distinguish between handwritten numbers, is a nice illustration of this. There are ten numbers in the typical 10-based numbering system and so this network can have 10 neurons in the output layer. If only the first neuron

produces a value close to 1 and other neurons produce values close to 0, the input number can be classified as a “0”. So the output from the output layer may look like “1000000000” for “0”. Similarly, for “1”, the output layer may look like “0100000000” and for “9”, the output layer may look like “0000000001”.

Hyperbolic tan function: The hyperbolic tan or tanh(x) is closely related to the sigmoid function in terms of the output it can generate based on the inputs it receives. Its output ranges from -1 to 1 as opposed to the 0 to 1 range of the sigmoid function. The hyperbolic tan function can be written as (Mishra et al., 2019):

$$\tanh(x) = \frac{e^{x} - e^{-x}}{e^{x} + e^{-x}} \tag{2.2}$$

Rectified linear unit (ReLU) function: The ReLU function is one of the most used activation functions of a neural network. It takes an input and outputs a 0 if the input is 0 or negative and outputs the input value unchanged if it is positive. It can be written as (Mishra et al., 2019):

$$ReLU(x) = \begin{cases} 0, if\ x \leq 0 \\ x, if\ x > 0 \end{cases} \tag{2.3}$$

ReLU function is used quite often in neural network models as it takes less computational time and power to calculate. But unlike sigmoid or tanh function, ReLU function cannot crunch the data between two numerical values and can generate values ranging from 0 to infinity.

Purelin function: Purelin is the simplest transfer function. Transfer functions calculate a layer's output from its net input. The purelin function can be written as (Mishra et al., 2019):

$$purelin(x) = x \tag{2.4}$$

2.11.4 Neural Network Learning

Neural network learning involves several sequential steps. Setting up a neural network with known inputs and outputs, choosing random values for the weights and biases, and then using an algorithm called the back-propagation algorithm to adjust the weights are the

major steps in the learning process. This is done so that the known inputs can produce the known outputs as accurately as possible (Doblies et al., 2019).

The learning rate is regarded as the most crucial hyper-parameter of a neural network architecture since it determines how quickly the network learns new information. Although it will take a very long time, a learning rate that is too low will lead to the weights being fine-tuned. A too-high learning rate will speed up training, but the outcomes will typically contain more mistakes. The goal is to identify the optimal learning rate that will allow the neural network model to acquire accurate knowledge as quickly as feasible.

2.11.5 Neural Network Testing

Typically, neural networks are tested to determine what kind of output they can produce with certain unknown input values. The neural networks' accuracy is determined by this. A similar process is employed in the research methodology. The Red, Green and Blue color values of thermally aged GFRP samples serve as the known input, and the known output is the thermal aging time and temperature of thermally aged GFRP. The efficiency of the neural networks is then assessed by testing them on a collection of Red, Green and Blue color values of thermally aged GFRP samples that they have never been trained on.

CHAPTER 3
MATERIALS AND METHODOLOGY

3.1 Introduction

This chapter discusses the materials and methodology used for this research work. The objective of this chapter is to aid in the validation of the results in case the study is to be repeated by another researcher. Experimental setup both the experimental and computational part of the work is discussed here. The experimental part discussed GFRP fabrication, machining, thermal Aging and mechanical property testing. The computational part discusses using image processing, ANNs and regression analysis using MATLAB and Minitab. Complete details of the materials used, specifications of the lab equipment, software tools and other experimental setup are presented. Some information has also been referred to the appendices.

3.2 Materials Used

Commercially available 1100 GSM high silica ($SiO2 \geq 96\%$) woven Glass fiber cloth was selected as the reinforcing element for preparing the GFRP composite material. This glass fiber cloth was purchased from Jiangnan Company and originated in Jiangsu, China. The glass fiber fabric has a thickness of 1.2 mm and a thread count of 15 for WEFT and 20 for WARP. Two different orientation of glass fiber cloth was chosen for this research.

As the matrix material, Araldite AW 106 IN epoxy resin and HV 953 U hardener were used. According to the manufacturer's recommendations, 100R/80H by weight of resin and hardener was utilized. The viscosity (cP) at 25°C is 50000 and 35000, respectively, while the specific gravities of the hardener and resin are 1.17 and 0.92, respectively. Appendix M shows the photos of the reinforcement and matrix material.

3.3 Methodology

The methodology used for this study involved 10 interrelated steps. The first 5 steps were part of the experimental work which dealt with fabrication and characterization of the GFRP. The other 5 steps were part of the computational work which dealt with predictive modeling. The step-by-step graphical methodology is shown in Figure 3.1 as follows.

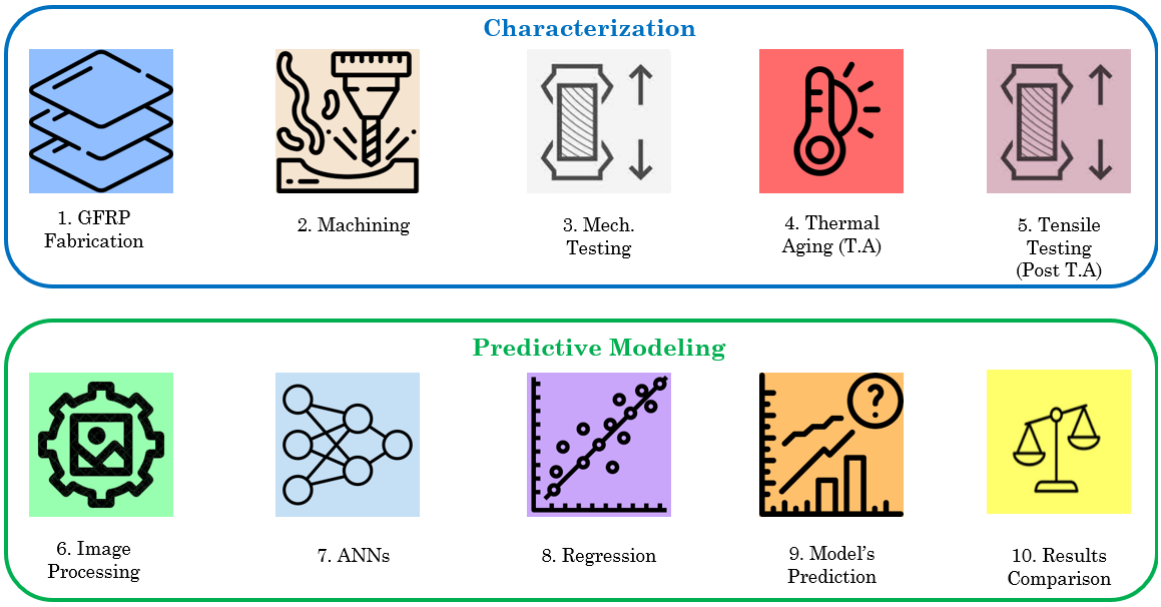

Fig. 3.1: Graphical methodology of this research.

The details of the 10-step methodology is as follows:

i. GFRP Composites were fabricated using woven and random glass fibers by hand-layup method.

ii. Samples for mechanical testing were prepared as per ASTM standards by mechanical cutting and laser cutting.

iii. These unaged samples underwent tensile test, flexural test, microhardness test and SEM imaging to find the effect of fiber orientation and machining on the mechanical properties.

iv. Tensile test Samples were thermally aged at different temperatures and times. Their distinct color changes at elevated temperatures were identified and photographed.

v. Thermally aged Samples were mechanically tested as per ASTM standards and results including Ultimate Tensile Strength (UTS), Yield Strength, Maximum Strain, Elastic Modulus and Tangent Modulus were recorded.

vi. An image processing algorithm identified the color changes of the thermally aged samples (from the photos taken in step iv) and gave the most consistent Red, Green and Blue (RGB) color values as the output.

vii. Two ANNs were trained which took input of the RGB values and predicted the thermal aging variables (aging temperature and time) the samples underwent.

viii. A regression analysis was performed to correlate UTS and thermal aging variables (aging temperature and time).

ix. The ANN-predicted aging temperature and time were used to predict the UTS value using the regression equation developed in step viii. This was the final output of the predictive model.

x. UTS from the experimental result (step v) and estimations of the predictive model (step ix) were analyzed and compared.

3.4 Fabrication of GFRP

The GFRP composite material was fabricated using the hand layup technique. The hand layup method is one of the traditional and widely used techniques for fabricating composite materials. It involves the manual placement of reinforcement fibers, such as fiberglass, in a mold, followed by the application of a resin matrix. Figure 3.2 shows the process of the handlayup method.

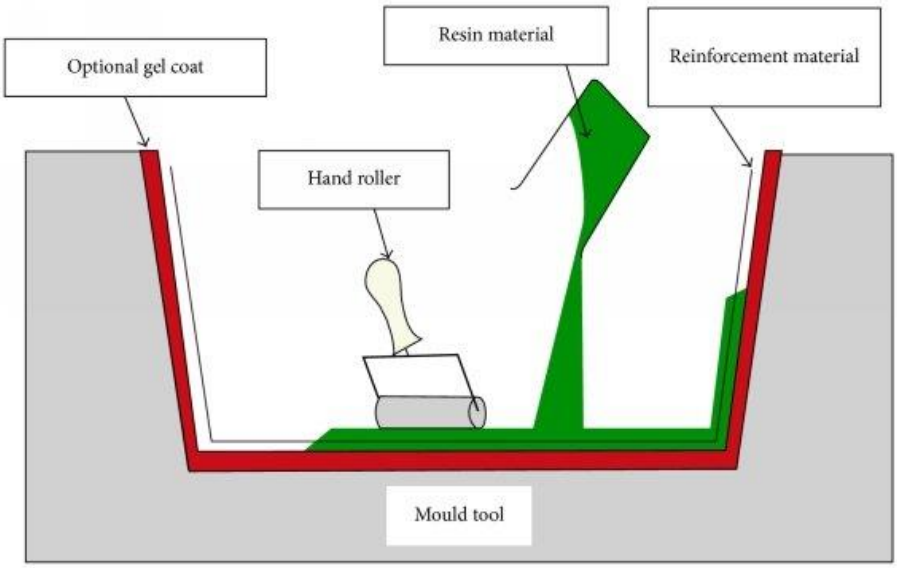

Fig. 3.2: Handlayup method of composite fabrication
(Udupi and Lester Raj Rodrigues, 2016).

GFRP sheets were prepared from both woven glass fibers and randomly oriented glass fibers. A plywood mold with the dimensions of 325 mm × 325 mm x 10 mm was employed. To create one composite slab, two layers of glass fibers were sliced into 325mm x 325mm squares from both woven fiber GFRP and random fiber GFRP. A clear plastic release sheet was positioned at the bottom and coated with wax to make the removal procedure easier after production. To prevent air entrapment, the resin-hardener mixture was first placed in one layer and spread uniformly with a spatula. Then, one layer of the resin-hardener

combination was put between two layers of glass fiber. The topmost layer was then filled with the resin-hardener combination and protected by a transparent plastic release film. Using a roller, gentle pressure was applied above the release film to release any trapped air. As soon as the topmost layer of resin-hardener was placed, the joint parts were clamped. The composite was then allowed to cure for 12 hours at room temperature under the weight of a 17 kg plywood sheet. The constructed composite slab had a 3mm thickness. Table 3.1 and 3.2 shows the composition of fabricated GFRP slab using woven and random glass fibers respectively.

Table 3.1: Composition of the woven GFRP composite slab

Material	Weight (gm)	Weight (%)
Glass Fiber Cloth	206	45
Epoxy Resin	138	30
Hardener	111	25
Total	456	100

Table 3.2: Composition of the random GFRP composite slab

Material	Weight (gm)	Weight (%)
Glass Fiber Cloth	150	45
Epoxy Resin	100	30
Hardener	80	25
Total	330	100

A total of 5 layers of reinforcement and matrix were laid up in the GFRP slab for both woven and random glass fibers. Figure 3.3 shows the arrangement of reinforcement and matrix layers in the GFRP slab.

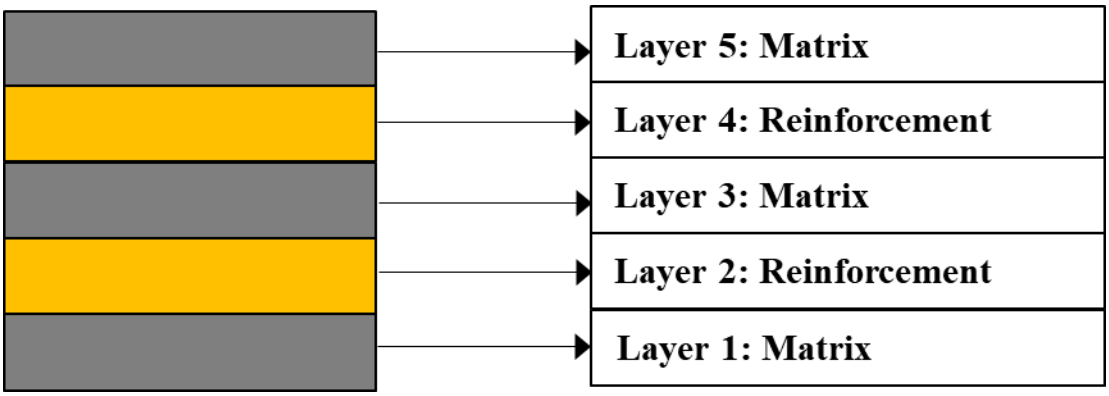

Fig. 3.3: Arrangement of layers in GFRP composite sheet.

After the curing time was finished, loads were removed from the GFRP mold. The GFRP slab was carefully removed from the protective polyurethane film to ensure a good surface finish. Figure 3.4 shows the fabricated GFRP composite slabs after curing.

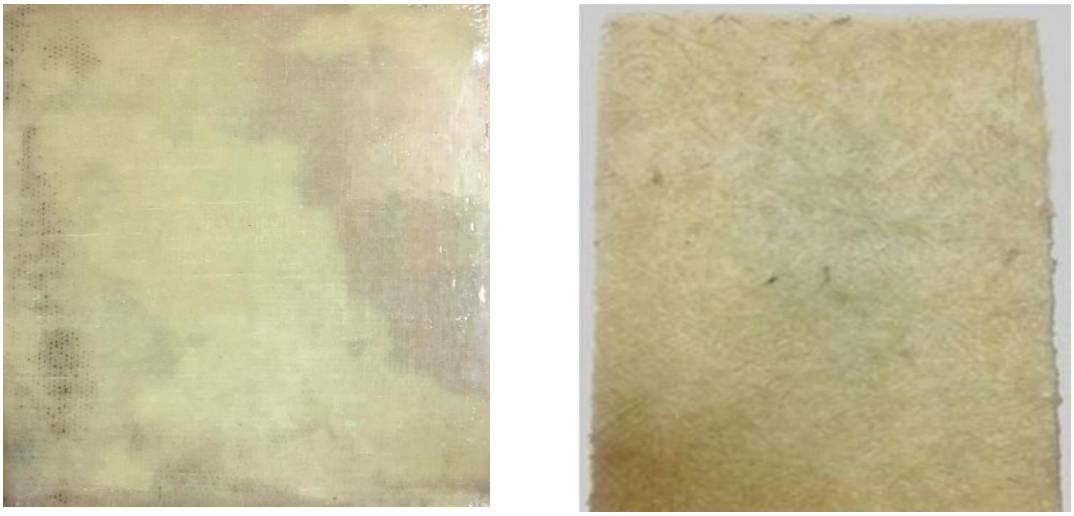

(a) (b)

Fig. 3.4: Fabricated Woven GFRP Sheet (a) Woven GFRP, (b) Random GFRP.

3.5 Machining of GFRP

The prepared composite slabs were both mechanically cut and laser cut to prepare the samples for mechanical testing. For mechanical cutting, Bosch GWS 900-100 professional angle grinder with TJWELD 1.2 mm thickness cutting wheel was used.

For laser cutting, CO_2 laser cutting machine model STJ1530M was employed. The laser power of this machine is 220w. The laser was used at 80% power (176w) with a 5 mm/s speed. It took two runs of the laser to completely cut the 3mm thickness of the sample. The

maximum temperature of the laser beam was 558°C. Although it varied around 450°C during the cutting process. This temperature was measured using UNI-T Pro UTI 260B professional thermal imager. Figure 3.5 shows the maximum temperature measurement of the laser beam.

Fig. 3.5: Measurement of laser beam temperature.

Using Mechanical and Laser machining, GFRP samples were prepared for mechanical testing as per ASTM standards. Table 3.3 shows the sample sizes as per ASTM standards for tensile, flexural and microhardness testing.

Table 3.3: GFRP sample dimensions of tensile, flexural and microhardness testing

Test Name	Sample Size (mm)	Ref Standard
Tensile Test	250 x 25 x 3	ASTM D3039 Standard Test Method for Tensile Properties of Polymer Matrix Composite Materials
Flexural Test (3 point)	125 x 12.7 x 3	ASTM D790 Standard test Methods for Flexural Properties of Unreinforced and reinforced Plastics and Electrical Insulating Materials
Microhardness Test	30 x 30 x 3	ASTM E-384 Standard Test Method for Micro indentation Hardness of Materials

A total of 80 samples were prepared for testing the tensile, flexural, microhardness (HV) properties and SEM imaging at room temperature. Also, a total of 48 samples were prepared for the tensile test of thermally aged GFRP. A grand total of 128 samples were prepared and tested including the 80 unaged samples and 48 thermally aged samples. Table 3.4 and 3.5 shows the sample count for Unaged and Thermally aged samples respectively.

Table 3.4: Unaged GFRP sample count

Fiber Orientation	Machining	Mechanical Property Testing				Total
		Tensile	Flexural	HV	SEM	
Woven Fiber	MC	5	5	5	5	20
	LC	5	5	5	5	20
Random Fiber	MC	5	5	5	5	20
	LC	5	5	5	5	20
Total		20	20	20	20	80

Table 3.5: Thermally aged GFRP sample count

	Time (mins)	Temperature (°C)				Total
		50	100	150	200	
Tensile Test	30	3	3	3	3	12
	60	3	3	3	3	12
	90	3	3	3	3	12
	120	3	3	3	3	12
Total		12	12	12	12	48

The prepared GFRP samples subjected to mechanical and laser cutting showed distinctive surface finishing. Figures 3.6, 3.7 and 3.8 shows the GFRP samples prepared using mechanical and laser cutting for tensile, flexural and microhardness tests respectively.

(a)

(b)

Fig. 3.6: Tensile test Samples (a) Mechanically cut, (b) Laser cut.

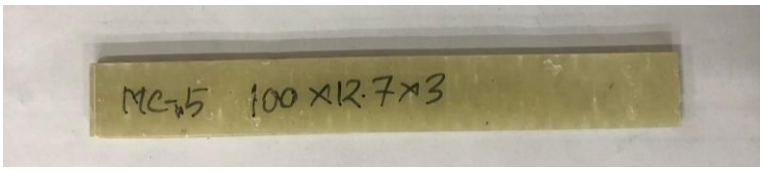

(a)

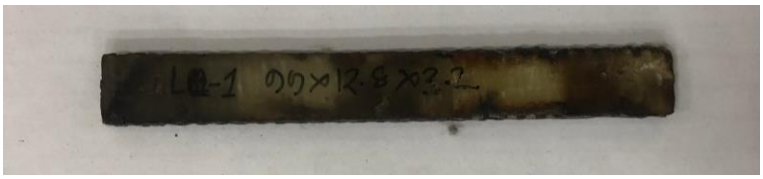

(b)

Fig. 3.7: Flexural test Samples (a) Mechanically cut, (b) Laser cut.

(a) (b)

Fig. 3.8: Microhardness test samples (a) Mechanically cut, (b) Laser cut.

3.6 Mechanical Property Testing

Mechanical property testing plays a crucial role in assessing and characterizing the performance of glass fiber reinforced composites. These tests provide valuable information about the strength, stiffness, toughness, and other mechanical properties of the composite material. By conducting rigorous mechanical property testing, engineers and researchers can evaluate the suitability of glass fiber reinforced composites for various applications and optimize their design and manufacturing processes.

In this research, tensile, flexural and microhardness tests were carried out. The prepared GFRP samples were machined and samples were prepared as per the dimensions specified in the respective ASTM standards. SEM imaging was also performed along the machined

edges and tensile fractured edges. Appendix N shows the photos of tensile, flexural, microhardness and SEM test equipment used for this study. Table 3.6 shows the GFRP sample size, ASTM standard and equipment used for tensile, flexural and microhardness testing.

Table 3.6: GFRP sample size, ASTM standard and equipment used for tensile, flexural and microhardness testing

Test Name	Equipment	Sample Size (mm)	Ref Standard
Tensile Test	HST Kason PLS 100 UTM Machine	250 x 25 x 3	ASTM D3039 Standard Test Method for Tensile Properties of Polymer Matrix Composite Materials
Flexural Test (3 point)	HST Kason PLS 100 UTM Machine	100 x 12.7 x 3	ASTM D790 Standard test Methods for Flexural Properties of Unreinforced and reinforced Plastics and Electrical Insulating Materials
Microhardness Test	TMTECK-10MDT Auto Turret Vickers Microhardness Tester	30 x 30 x 30	ASTM E-384 Standard Test Method for Micro indentation Hardness of Materials
SEM Imaging	JSM-7610F Field Emission SEM	3 x 3 x 3 (approximate)	As per OEM

3.6.1 Tensile Test

Tensile testing is a fundamental method used to evaluate the mechanical properties of glass fiber reinforced composites. This test provides valuable information about the tensile strength, modulus, and elongation characteristics of the material. Understanding these properties is crucial for assessing the performance and suitability of glass fiber reinforced composites in various applications.

During a tensile test, a test specimen of the composite material is subjected to an axial load in a controlled manner until it fractures. The test measures the force applied to the specimen and the corresponding deformation, allowing for the determination of key tensile properties. The ultimate tensile strength represents the maximum load the specimen can withstand before failure, indicating the material's resistance to tensile forces. The elastic modulus, also known as Young's modulus, represents the stiffness of the material and is determined from the initial linear portion of the stress-strain curve.

Tensile testing provides insights into the failure behavior of glass fiber reinforced composites. The fracture pattern and the presence of specific failure modes, such as fiber pull-out or fiber breakage, can be analyzed to understand the composite's performance under tension. Additionally, the strain at failure or elongation at break provides information about the material's ductility or brittleness.

The tensile test was performed on flat samples as per ASTM D3039 standard (“Standard Test Method for Tensile Properties of Polymer Matrix Composite Materials,” 2014). Samples are cut into 250mm x 25mm x 3mm sizes with end tabs. The test was performed in the universal testing machine (UTM) PLS100 with a crosshead speed of 5mm/min. The flat samples were fixed between the grips of each head of the testing machine. The grip was set up in such a way that the direction of force applied to the sample was coincident with the longitudinal axis of the sample. Fig 3.9 and 3.10 shows the tensile test samples following the tensile failure during the test for woven and random samples respectively.

(a)

(b)

Fig. 3.9: Woven GFRP samples after tensile test (a) Mechanically cut, (b) Laser cut.

(a)

(b)

Fig. 3.10: Random GFRP samples after tensile test (a) Mechanically cut, (b) Laser cut.

The Tensile test was performed for a total of 51 samples from 17 SGNs with 3 samples in each SGN. At first, 03 thermally unaged samples underwent tensile testing. From the tensile test data, max strain (%), UTS (MPa), yield strength (MPa), elastic modulus (MPa) and tangent modulus (MPa) were calculated. Afterward, 48 thermally aged samples underwent tensile testing. The average values of the 3 samples in each group were considered for the respective group. Finally, a total of 17 sets of tensile test data was obtained including UTS, Max Strain and Yield Strength.

3.6.2 Flexural Test

Flexural testing is a crucial method for evaluating the mechanical properties of glass fiber reinforced composites, particularly their strength and stiffness under bending loads. This test provides valuable information about the flexural modulus, flexural strength, and fracture behavior of the material, which are important considerations for structural applications.

In a flexural test, a test specimen of the glass fiber reinforced composite is subjected to a three-point or four-point bending load. The specimen is supported on two points or three points, respectively, and a load is applied at the midpoint. As the load increases, the specimen undergoes bending, and the resulting stress and strain are measured. This test allows for the determination of the flexural modulus, which represents the material's resistance to deformation under bending, and the flexural strength, which represents the maximum stress the material can withstand before failure.

Flexural testing provides insights into the performance of glass fiber reinforced composites under bending loads, which are common in structural applications. It helps assess the material's ability to withstand bending stresses and provides information about its resistance to fracture and deformation. The fracture behavior observed during the test, such as fiber breakage or delamination, can be analyzed to understand the failure mechanisms and improve the composite's design and manufacturing processes.

The flexural test was performed utilizing a three-point loading system applied to a simply supported flat GFRP specimen as per ASTM standard D790 (“Standard Test Methods for Flexural Properties of Unreinforced and Reinforced Plastics and Electrical Insulating Materials,” 2017). This test was employed by a universal testing machine (UTM) PLS100 with a crosshead speed of 5 mm/min. Samples were cut into 100mm x 12.7mm x 3mm size. The support span size was 60mm. The flat samples were placed between the support span. The load was applied to the samples at the center of the support span and the load-deflection characteristics were investigated from the flexural test of the GFRP samples. Detailed data from the tensile test was analyzed to calculate Ultimate Flexural Strength (UFS) and Flexural Modulus. The test was performed on five samples and the average values along with standard deviations were calculated for each data. Figure 3.11 and 3.12 shows the

flexural test samples following the flexural failure during test for woven and random samples respectively.

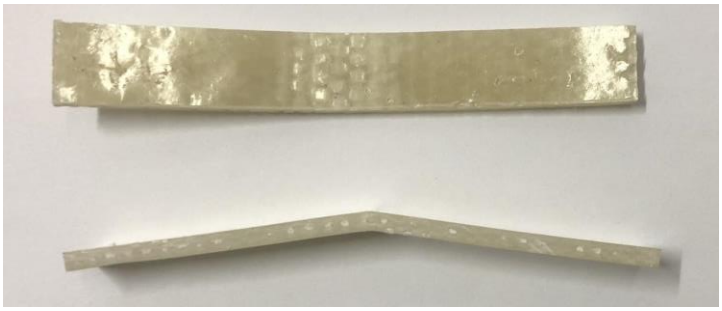

(a)

(b)

Fig. 3.11: Woven GFRP samples after flexural test (a) Mechanically cut, (b) Laser cut.

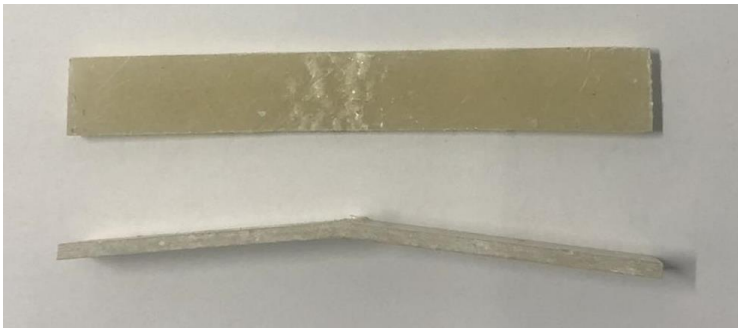

(a)

(b)

Fig. 3.12: Random GFRP samples after flexural test (a) Mechanically cut, (b) Laser cut.

3.6.3 Microhardness Test

Vickers microhardness testing is a valuable method for evaluating the hardness and mechanical properties of glass fiber reinforced composites at a microscopic scale. This test provides information about the material's resistance to indentation, which can be indicative of its strength and toughness.

In Vickers microhardness testing, a pyramidal-shaped indenter with a square base is pressed into the surface of the glass fiber reinforced composite under a specific load. The indentation size is measured, typically using an optical microscope, and the Vickers hardness number (HV) is calculated based on the applied load and the surface area of the indentation. Unlike traditional hardness tests, such as Rockwell or Brinell, Vickers microhardness testing allows for smaller indentations and provides more localized hardness measurements.

Vickers microhardness testing is particularly useful for characterizing the hardness variations within a glass fiber reinforced composite. It can help identify differences in hardness between the matrix and the reinforcement, as well as variations in different regions of the composite structure. By mapping the hardness distribution, researchers can gain insights into the material's microstructure, such as the degree of fiber-matrix bonding or the presence of defects.

Several studies have utilized Vickers microhardness testing to investigate the mechanical properties of glass fiber reinforced composites (Zhou et al., 2007; Pan, 2022). The results obtained from these tests contribute to understanding the material's response to localized loading and aid in the optimization of composite fabrication processes. Standards and guidelines, such as ASTM E384 (“Standard Test Method for Microindentation Hardness of Materials,” 2022), provide standardized procedures and recommendations for conducting Vickers microhardness testing on a wide range of materials, including glass fiber reinforced composites. These standards ensure consistency and accuracy in testing methodologies, allowing for reliable comparison of results across different studies.

Vickers Micro Hardness testing machine TMHV-10MDT manufactured by TMTeck Instrument Company Ltd. was used in this experiment. This machine has a diamond indenter of a pyramid shape at an angle of 136°. Samples were cut into a 30mm x 30mm x

3mm size and tested on the aforementioned tester as per ASTM standard E384. The test load was selected as 300 grams. During the test, the pyramid indenter presses on the sample with the prescribed test load. Accordingly, a pyramid shape indentation is made on the sample. Attached microscopes are then used to measure the two diagonals of the pyramid shape. Then the Vickers Micro Hardness value (HV) is calculated and displayed in the machine. Five samples had been tested from both mechanically cut and laser cut GFRP. Ten HV readings were taken from each sample to calculate the average HV and standard deviation for each sample.

3.6.4 Scanning Electron Microscope (SEM) Observation

Scanning electron microscope (SEM) testing is a powerful technique used to analyze the microstructure and surface morphology of glass fiber reinforced composites. This method provides detailed information about the fiber-matrix interface, fiber distribution, and the presence of defects or damage within the composite material.

In SEM testing, a focused electron beam scans the surface of the composite, and the interactions between the beam and the material produce various signals, such as secondary electrons, backscattered electrons, and X-rays. These signals are detected and processed to generate high-resolution images and elemental composition maps of the sample.

SEM imaging allows for the observation of the composite's microstructure at high magnification, revealing details about the fiber arrangement, fiber-matrix bonding, and the presence of voids, cracks, or delamination. It provides insights into the quality of the composite fabrication process and the effectiveness of interfacial bonding between the glass fibers and the matrix.

Additionally, SEM testing can be coupled with energy-dispersive X-ray spectroscopy (EDS) analysis, which enables the identification and mapping of elemental compositions within the composite. This information helps in understanding the distribution of elements and the chemical interactions at the fiber-matrix interface.

Numerous studies have employed SEM testing to investigate the microstructural characteristics of glass fiber reinforced composites. The results obtained from SEM analysis contribute to the understanding of the material's failure mechanisms, the

optimization of fabrication processes, and the development of advanced composite materials. SEM testing is typically conducted following proper sample preparation, including sample mounting, polishing, and coating to enhance conductivity and minimize charging effects.

The machined surface of one sample each from mechanically cut and laser cut composites was examined using Scanning Electron Microscope (SEM) model JSM-7610F. Micrographs of the machined surface are taken in 150x, 300x and 700x magnification at 15 kV setting. The tensile fractured surface of one sample each from mechanically cut and laser cut composites had also been studied using Scanning Electron Microscope (SEM) model JSM-7610F. Micrographs of the tensile fractured surface were taken in 150x, 300x and 700x magnification and 15 kV setting.

3.7 Thermal Aging

As this study involves thermal aging, the elevated temperature properties of the reinforcement and the matrix were very important considerations. The glass fiber cloth used in this study can reportedly withstand operating temperatures of up to 1100°C and has a melting point of 1700°C, according to the manufacturer. The glass transition temperature (Tg) of the resin-hardener is 63°C as reported by the manufacturer. The specification highlighting the Tg of the epoxy resin and hardener is shown in Appendix J.

The Glass Transition Temperature (Tg) is one of the most important properties of any epoxy and is the temperature region where the polymer transitions from hard, glassy material to a soft, rubbery material. For comparison with room temperature mechanical properties, 3 samples were also tested. These room-temperature samples are not thermally aged in ovens and are hereafter referred to as “Unaged” samples.

Temperature and time were the two variables selected for the thermal aging of the samples. For thermal aging, specific temperatures and aging times were chosen considering the problem statement in aerospace applications and Tg of the epoxy. ATR 72-212A aircraft is certified for 120 mins Extended Twin Engine Operations (ETOPS). The relevant type certificate document is presented in Appendix K. It means that with only one out of two engines serviceable, this aircraft can fly a maximum of 120 mins. Single-engine operations put maximum stress on the engine. For this reason, the temperature in the GFRP bleed ducts

is the highest in this condition. Also, as per the Airconditioning system schematic of ATR 72-212A aircraft, the maximum allowable bleed temperature is 204°C. The ATR 72-212A air conditioning system schematic is presented in Appendix L. Beyond this temperature, the bleed is shut off. Hence, during the operations, the most extreme situations can occur in terms of thermal aging in bleed ducts at 200°C for 120 mins. Again, to study the effect of thermal aging below but near the Tg temperature of 63°C is also required.

As such The selected thermal aging temperatures were 50°C, 100°C, 150°C and 200°C while the thermal aging time were 30 mins, 60 mins, 90 mins and 120 mins. Such temperatures and exposure times are frequently encountered in the case of Air-conditioning bleed ducts of commercial aircraft and UAV operations and as well.

Tensile testing samples were thermally aged in Carbolite Gero CWF 13/13 furnace. As per the manufacturer's specifications, this furnace can reach the maximum temperature of 1300°C in 121 minutes with a maximum continuous operating temperature of 1200°C. The internal dimension of the furnace chamber is 200 mm x 200 mm x 325 mm which is sufficient to accommodate several tensile testing samples at once.

For each one of the thermal aging temperatures, samples were aged at all the above aging times. As such, a total of 16 combinations of thermal aging were performed in the ovens. With the addition of the unaged samples, the total number of combinations were 17. These 17 combinations were labeled as sample group numbers (SGN). Each of the sample groups had 3 samples making a total of 51 samples for 17 groups. Table 3.7 shows the sample group numbers and associated thermal aging variables.

Table 3.7: Sample group numbers and associated thermal aging variables

Sample group number (SGN)	Aging temperature	Aging time	Number of samples in the group
1	Unaged	Unaged	3
2	50°C	30 mins	3
3	50°C	60 mins	3
4	50°C	90 mins	3
5	50°C	120 mins	3
6	100°C	30 mins	3
7	100°C	60 mins	3
8	100°C	90 mins	3
9	100°C	120 mins	3
10	150°C	30 mins	3
11	150°C	60 mins	3
12	150°C	90 mins	3
13	150°C	120 mins	3
14	200°C	30 mins	3
15	200°C	60 mins	3
16	200°C	90 mins	3
17	200°C	120 mins	3

3.8 Computational Work

The computational work relies on the data obtained from the experimental work. This work was done in MATLAB and Minitab software. Three parts of the computational model namely, image processing, ANNS and regression analysis was done separately in respective software. Image processing and ANNs were developed in MATLAB while Regression was done in Minitab. Standard library functions were used to perform the calculations. However, all the data processing, standardization and sequencing were done with codes specifically written for the model. Finally, a master code was developed to integrate the results of the three parts of the model and provide the final output. The model was able to predict the UTS value of thermally aged GFRP from a photograph of the sample.

3.8.1 Image Processing

A MATLAB image processing program using 'imread' function was developed which can read and identify the color changes of the samples. The `imread` function in MATLAB is a powerful tool for reading and importing digital images into the MATLAB environment. It allows users to access and manipulate image data for various applications, including image processing, computer vision, and data analysis.

The `imread` function is part of the Image Processing Toolbox in MATLAB and provides a straightforward syntax for loading images in different formats, such as JPEG, PNG, BMP, and TIFF. By specifying the file name or path as the input parameter, `imread` reads the image file and returns a matrix representation of the image data. ("Read image from graphics file - MATLAB imread," n.d.)

One of the key advantages of the `imread` function is its ability to handle both grayscale and color images. Grayscale images are represented as 2D matrices, where each element corresponds to the intensity value of a pixel. Color images, on the other hand, are represented as 3D matrices, with each element containing the RGB (Red, Green, Blue) color values of a pixel.

Researchers and practitioners in various fields have utilized the `imread` function in numerous applications. For instance, in image processing, `imread` is commonly used for image enhancement, noise reduction, and feature extraction tasks. In computer vision, it aids in object detection, image recognition, and tracking algorithms. Additionally, in

scientific research, `imread` enables the analysis of images captured in experiments or simulations. (Gonzalez, R. C., & Woods, R. E. 2002)

The photos of the thermally aged samples were uploaded to the 'imread' function within the MATLAB program. The program performed calculations and gave the most consistent value of the Red, Green and Blue color (RGB) values in a matrix form for each of the samples. The code was optimized in such a way that even if there was some slight variation of color throughout different areas of the sample, the code was able to Figure out the most consistent value.

All of the photos of the samples were taken on the same day by keeping the lighting conditions same. This was an important criterion as large variations of light exposure have the possibility of distorting the color values and thus de-normalizing the dataset of the image processing algorithm. Figure 3.13 shows the pseudocode used for the image processing algorithms in MATLAB. Figure 3.14 shows the MATLAB 'imread' function.

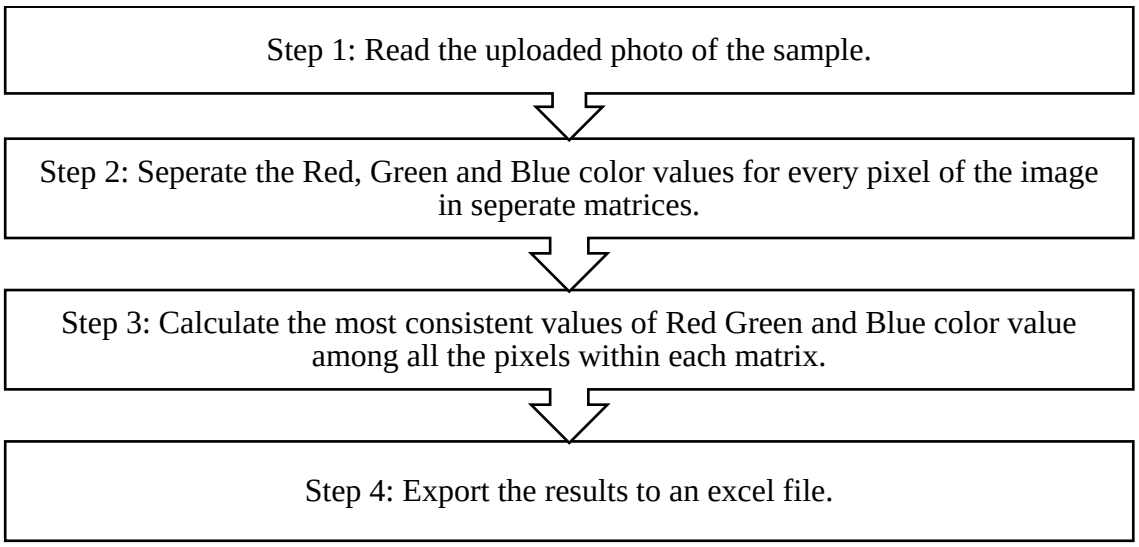

Fig. 3.13: MATLAB pseudocode of the image processing algorithm.

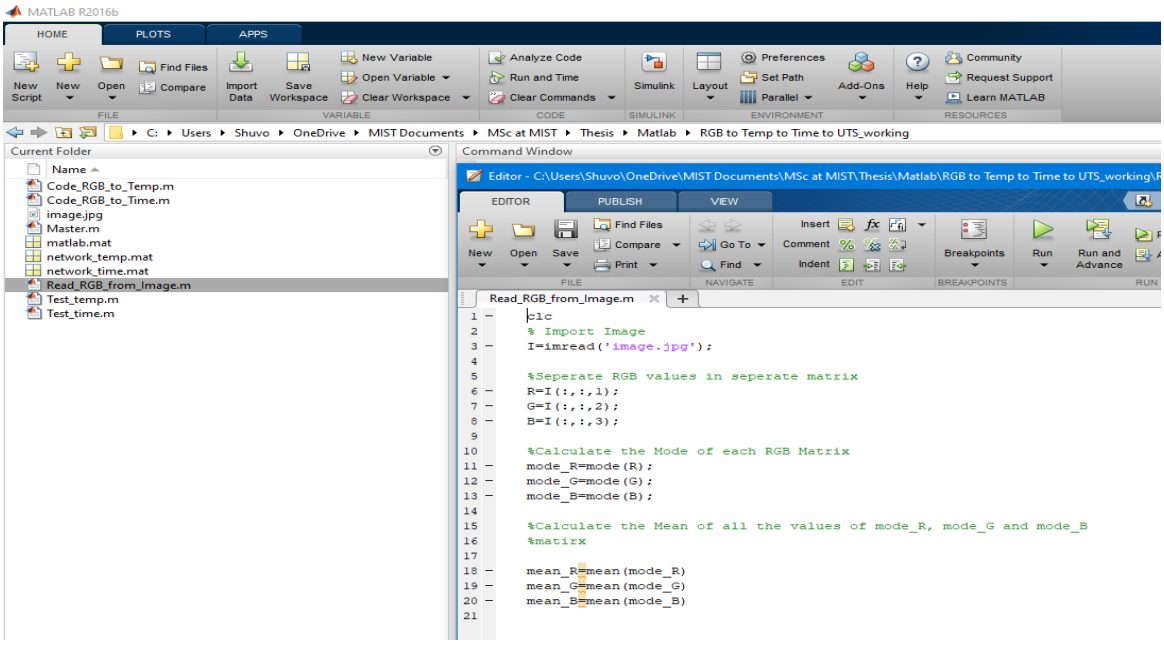

Fig. 3.14: MATLAB image processing algorithm with ‘imread’ function.

3.8.2 Artificial Neural Networks

Artificial Neural Networks (ANN) is a biologically-inspired computational method. It is one of many Artificial Intelligence algorithms and techniques. The ANN technique is based on a group of interconnected units or nodes called artificial neurons. The architecture of ANN consists of an input layer, one or several hidden layers and an output layer. As their name suggests, the input layer provides the input parameters to the ANN and the output layer provides the desired output. The calculations are performed by the hidden layers using weights and biases. The overall structure loosely models the neurons in a biological brain.

The nntool is a powerful graphical user interface (GUI) tool in MATLAB that facilitates the design, training, and evaluation of artificial neural networks (ANNs). It provides a user-friendly environment for constructing and fine-tuning neural network architectures for various applications, such as pattern recognition, classification, and regression.

In MATLAB, the nntool can be accessed through the Neural Network Toolbox, which offers a comprehensive set of functions and tools for neural network analysis. The nntool allows users to define the network architecture by specifying the number of layers, the number of neurons in each layer, and the activation functions. It provides flexibility in choosing various network types, including feedforward networks, recurrent networks, and radial basis function networks.

The nntool in MATLAB also enables users to train the neural network using different algorithms, such as backpropagation, Levenberg-Marquardt, and resilient backpropagation. It provides options for setting training parameters, including the number of epochs, learning rate, and momentum. Users can monitor the training progress through visualizations, such as error curves and weight updates. (Haykin, S. 2009)

Furthermore, the nntool allows users to evaluate the performance of the trained network using test data. It provides measures like mean squared error, classification accuracy, and confusion matrices to assess the network's accuracy and generalization capabilities. Additionally, the nntool supports visualization of the network structure, weight matrices, and activation profiles, aiding in the interpretation and analysis of the network's behavior. (“Deep Learning ToolboxDocumentation,” n.d.)

Selecting the number of hidden layers and neurons in an Artificial Neural Network (ANN) is an important task, as it directly impacts the network's learning capability and performance. While there isn't a definitive rule for determining the optimal number of hidden layers and neurons, there are some approaches can be followed. Some problems may require more complex architectures with multiple hidden layers, while others can be adequately addressed with a simpler network. Training and evaluating the network using appropriate evaluation metrics is also an approach. If the model is underfitting (has high training and validation errors), it might be considered to increase the complexity by adding more hidden layers or neurons. On the other hand, if the model is overfitting (performs well on training data but poorly on unseen data), it may be needed to reduce the number of hidden layers or neurons, or use regularization techniques like dropout or L1/L2 regularization. That there is no one-size-fits-all solution, and finding the optimal architecture often requires experimentation and iteration. It's essential to strike a balance between model complexity, computational resources, and the available dataset's generally recommended to start with a smaller architecture and gradually increase its complexity if needed. As such, the number of layers, amount of neurons and transfer functions are chosen through trial and error to achieve a balance between accuracy, computational time and architectural complexity. The ‘nntool’ toolbox of MATLAB is shown in Figure 3.15.

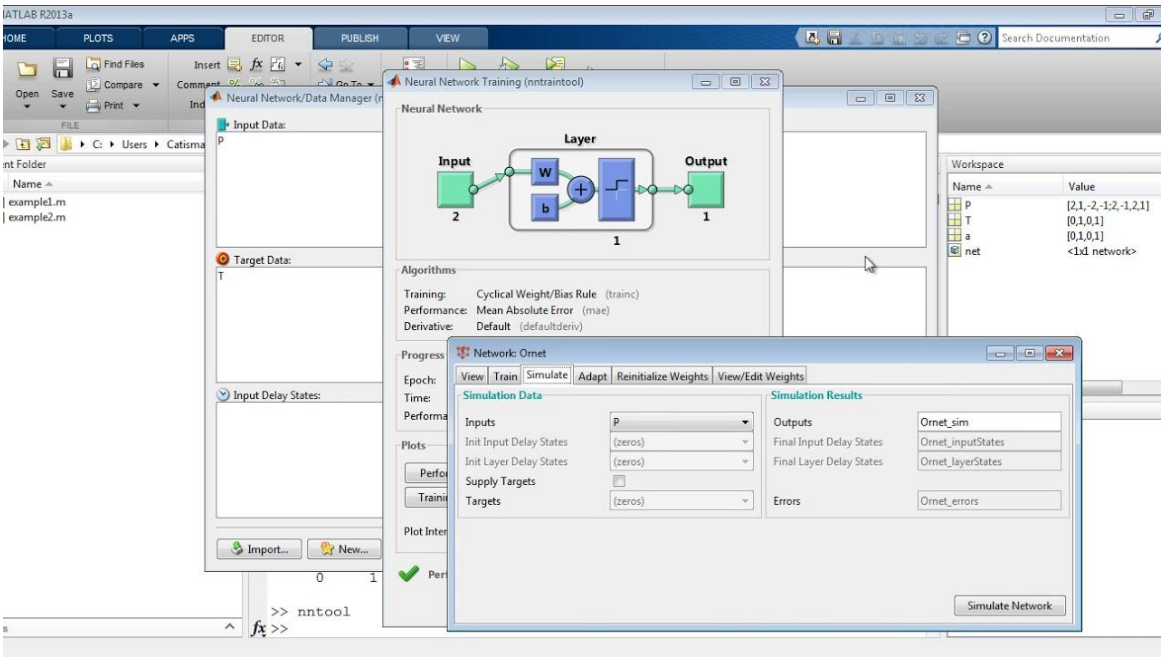

Fig. 3.15: nntool toolbox in MATLAB.

Using MATLAB, two ANNs were used in series to predict the thermal aging temperature and time. ANN1 took 3 inputs as the RGB values and gave the thermal aging temperature as the output x_1. ANN2 takes 4 inputs including the same 3 previous RGB values and the output of the first ANN, x_1. The output of the second ANN is the thermal aging time x_2. Both ANNs consist of two layers including one hidden layer and one output layer. The hidden layer has 10 neurons and the output layer has 1 neuron. The transfer function of the hidden layer is chosen as tansigmoid while the transfer function of the output layer is chosen as purelin.

A lot of trial and error was performed in selecting the number of layers, neurons and the transfer functions. Increasing the number of layers and neurons have the potential of increasing the accuracy at the cost of processing power and time. However, this outcome is also heavily dependent on the composition of the dataset and its inter-relationship. After testing different combinations of many layers and neurons, the architecture of the ANNs were finalized at the chosen configuration. Regarding the transfer function, tansig was chosen to have all the color values normalized within +1 and -1. This reduced the propagation of errors in the image-processing algorithm. The transfer function of the output layer was kept as purelin to simplify the model and develop a linear relationship. Figure 3.16 shows the architecture of the two ANNs.

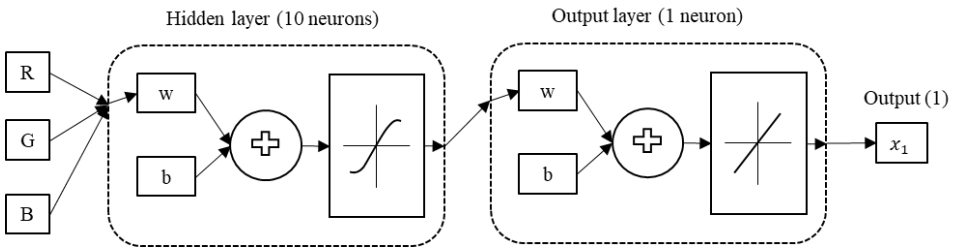

(a)

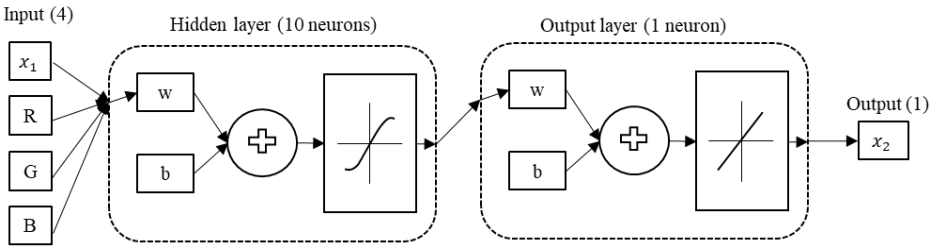

(b)

Fig 3.16: The architecture of the two ANNs (a) ANN1, (b) ANN2.

Total 24 sets of thermal aging data were used for the training and testing of the two ANNs. Among the 24 sets, 19 set were used for the training and the remaining 5 sets were used for testing. These datasets are presented in Appendix G and Appendix H respectively.

3.8.3 Regression Analysis

A multi-regression analysis was performed in Minitab software. The regression analysis developed an equation to estimate the UTS values from the thermal aging variables. The tensile testing dataset of SGN 1-17 shown in table 3 was used to perform the regression. The thermal aging temperature and time were considered as the two independent variables. UTS was the dependent variable. The two cascaded ANNs estimated the thermal aging temperature.

Multiple regression analysis is a statistical technique used to examine the relationship between a dependent variable and two or more independent variables. It is a powerful tool for analyzing complex data sets and identifying the most influential factors that impact the outcome of interest. Minitab, a popular statistical software package, provides robust capabilities for conducting multiple regression analyses.

In Minitab, the multiple regression analysis is performed using the "Regression" menu, which allows users to specify the dependent variable and select the independent variables

for analysis. Minitab automatically fits the regression model, estimates the coefficients, and provides various statistical measures, such as the coefficient of determination (R-squared), significance levels, and confidence intervals (Montgomery et al., 2012).

CHAPTER 4
CHARACTERIZATION OF GFRP

4.1 Introduction

This chapter discusses the characterization the fabricated GFRP composites by performing tensile, flexural and microhardness tests. SEM imaging is also performed to investigate the effect of machining on the machined surface. SEM of the tensile fracture surface is also performed to determine the nature of the tensile failure. Thermal aging of tensile test samples is performed to study the effect on the appearance and tensile properties. Comparison with material specifications and relevant literature is presented as a validation of the experimental work. Finally, A dataset of UTS values with corresponding thermal aging conditions is developed for subsequent use in the predictive model.

4.2 Effect of Fiber Orientation and Machining on Surface

The machined surface of one sample each from mechanically cut and laser cut composites was studied to identify the effect of machining on GFRP. Scanning Electron Microscope (SEM) model JSM-7610F was used to study the micrographs of the machined surface of both woven GFRP and random GFRP samples.

For woven GFRP, it is noted that the laser cut samples have burn spots all the way through the thickness of the machined edge of the composite for both woven and random GFRP. Whereas the mechanically cut samples exhibit no such observation. The reason behind these burn marks is the thermal damage of the laser beam. Figure 4.1 shows mechanically cut and laser cut samples and their machined edge.

(a) Mechanically cut

(b) Laser cut

Fig. 4.1: Photo of machined edge of woven GFRP samples
(a) Mechanically cut, (b) Laser cut.

SEM Micrographs of the machined surface are taken in 150x, 300x and 700x magnification at 15 kV setting. From Figure 4.2, a comparison of surface finishing pattern and quality between mechanically cut and laser cut samples can be observed. Figure 4.2(a) shows the surface smoothness and uniformity, good adhesion and uniformly axially aligned fibers in the mechanically cut sample. In contrast, Figure 4.2 (b) shows burnt and rough surfaces, potholes and coagulation of burnt matrix in the laser-cut sample.

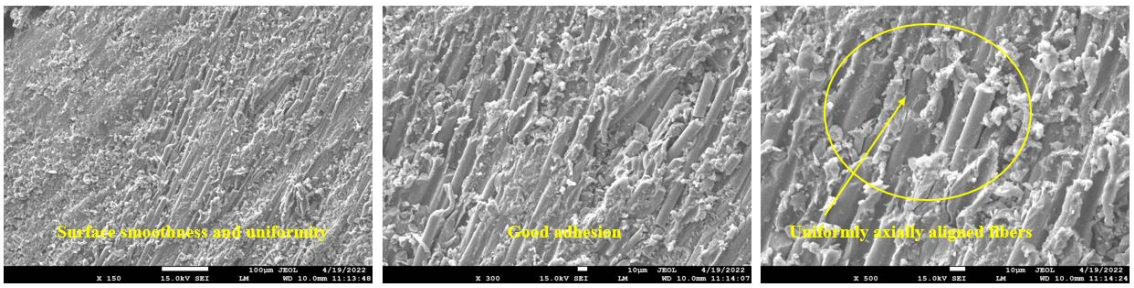

(a)

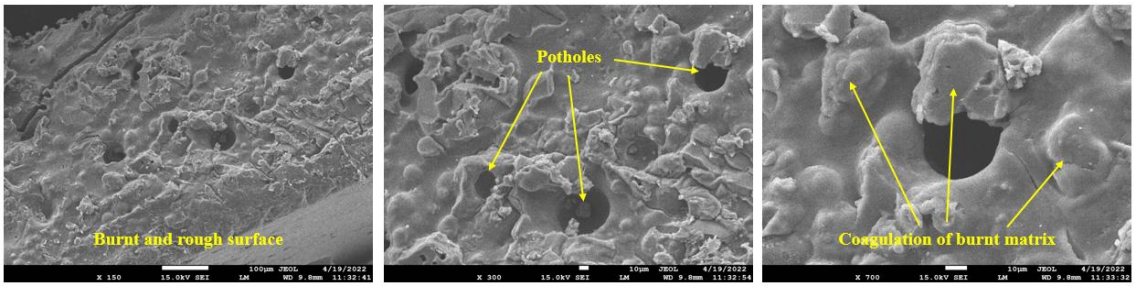

(b)

Fig. 4.2: SEM of woven GFRP machined surfaces
(a) Mechanically cut, (b) Laser cut.

Similar to woven GFRP. Additionally, it was observed that both woven and random GFRP samples from laser cutting include burn spots that extend all the way to the thickness of the composite's machined edge. The mechanically cut samples, however, do not show such a finding. The laser beam's thermal damage is the cause of these burn marks. Figure 4.3 shows mechanically cut and laser cut samples and their machined edge.

(a)

(b)

Fig. 4.3. Photo of Machined edge of random GFRP samples

(a) Mechanically cut, (b) Laser cut.

SEM Micrographs of the random GFRP machined surface are acquired at 10 keV at magnifications of 150x, 300x, and 500x. Figure 6.4 shows a comparison of surface finishing pattern and quality between mechanically cut and laser cut samples. Figure 4.4 (a) shows the surface smoothness and uniformity, randomly aligned fibers and good adhesion in the mechanically cut sample. In contrast, Figure 4.4 (b) shows surface roughness and non-uniformity, potholes and coagulation of the burnt matrix in the laser cut sample.

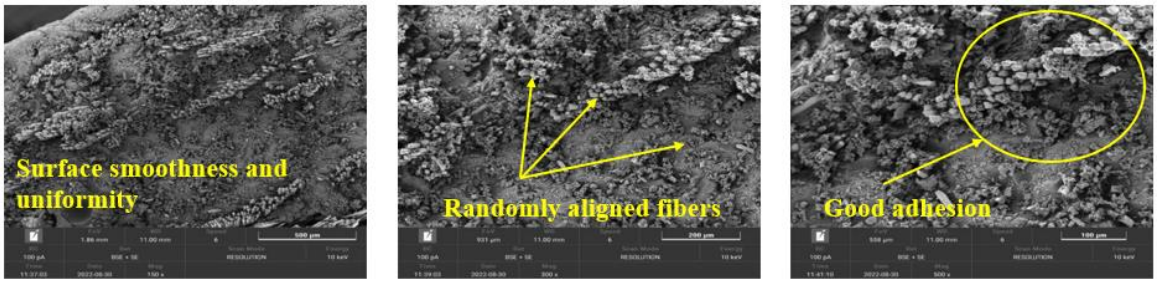

(a)

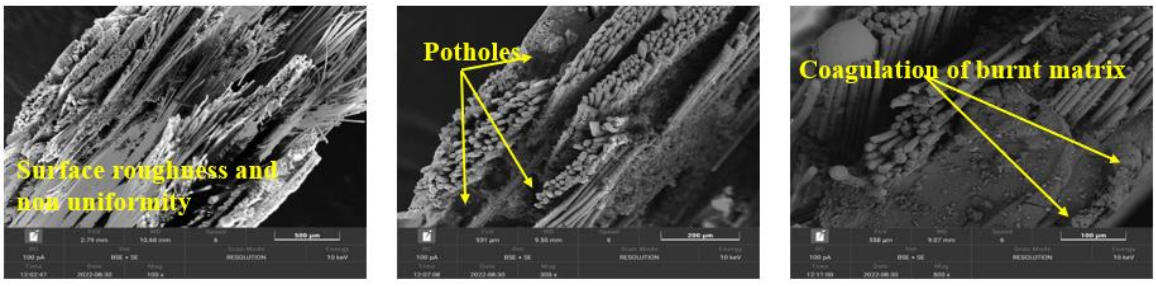

(b)

Fig. 4.4: SEM of random GFRP machined surfaces

(a) Mechanically cut, (b) Laser cut.

From the SEM imaging of both woven and random GFRP, it is evident that the laser beam has caused thermal damage to the surface, compromising its integrity. Due to high

temperature up to 598°C, the epoxy melted and subsequently re-hardened creating voids and potholes. Also, during the re-hardening, the matrix was rearranged in a random matter creating irregular and rough surface finishing.

By comparing this study with the literature shows similar findings regarding the effect of laser cutting on machined surface of FRP composites in general. Figure X shows burn marks, Heat Affected Zone (HAZ) and fiber pullout which is consistent with the findings of this work presented in Figure 4.5.

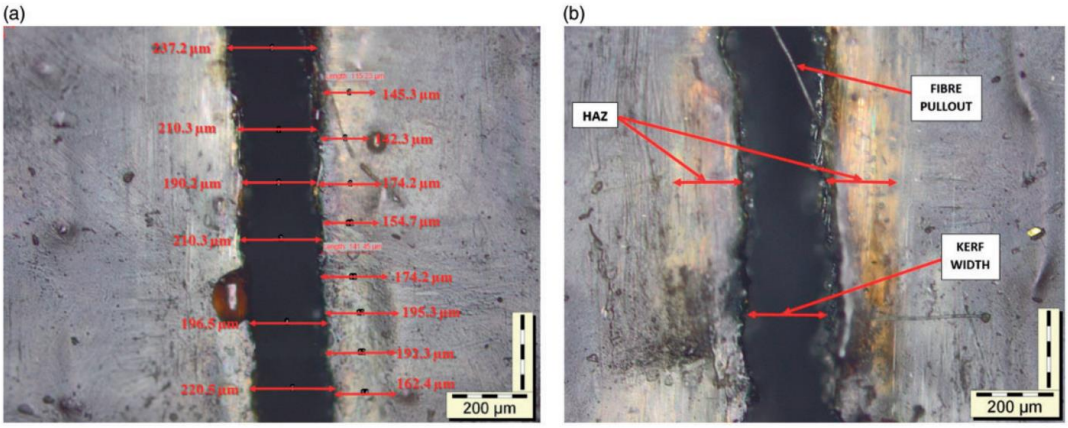

Fig. 4.5: Effect of laser cutting on CFRP composite from literature (Rao B et al., 2018).

In Figure 4.6, an SEM image comparing GFRP machined surface subjected to mechanical and laser cutting is shown which is referred to existing literature. The mechanical cutting shows good surface smoothness and adhesion. While laser cutting imparts delamination, potholes, and surface roughness. Both these findings from the literature are in agreement with the findings of this study.

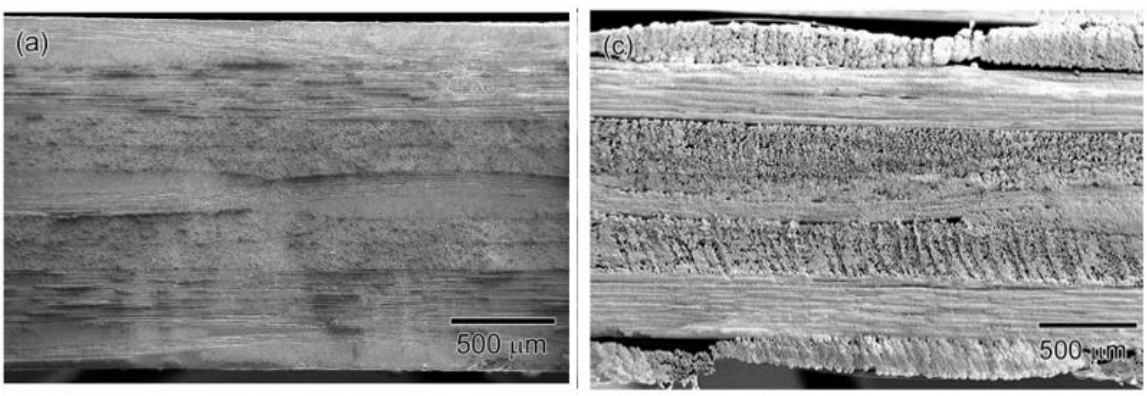

Fig. 4.6: SEM Image of CFRP machined surface from literature
(a) Mechanical Cutting, (b) Laser Cutting (Harada et al., 2012).

4.3 Effect of Fiber Orientation and Machining on Tensile Behavior

The load-deflection characteristics are investigated from the standard tensile test of unaged GFRP samples. The characteristics of both mechanically cutting and laser cutting samples are then expressed in terms of conventional stress-strain curves. The results are presented for Woven and Random GFRP separately.

For Woven GFRP, Figures 4.7 and 4.8 present stress-strain relations of mechanically and laser cut samples for woven and random GFRP respectively. Also, the average values from both mechanically cutting and laser cutting have been shown comparatively to highlight the differences in stress-strain behavior.

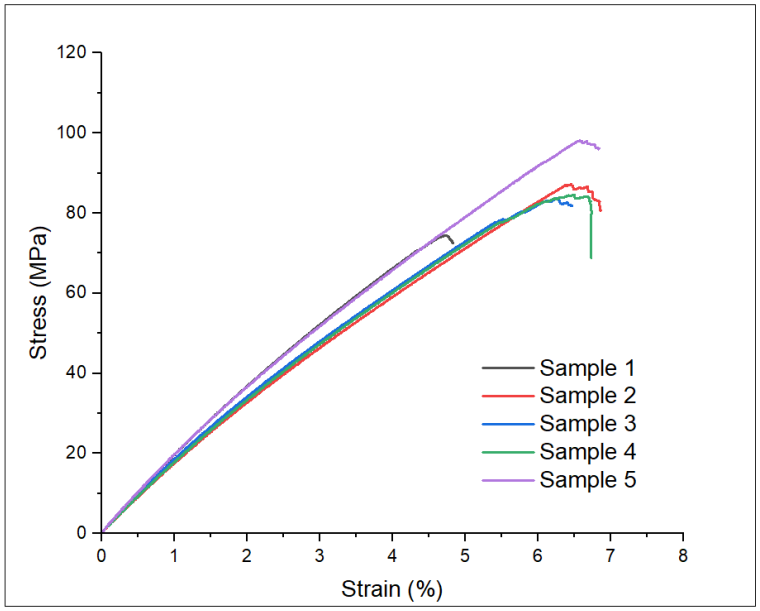

(a)

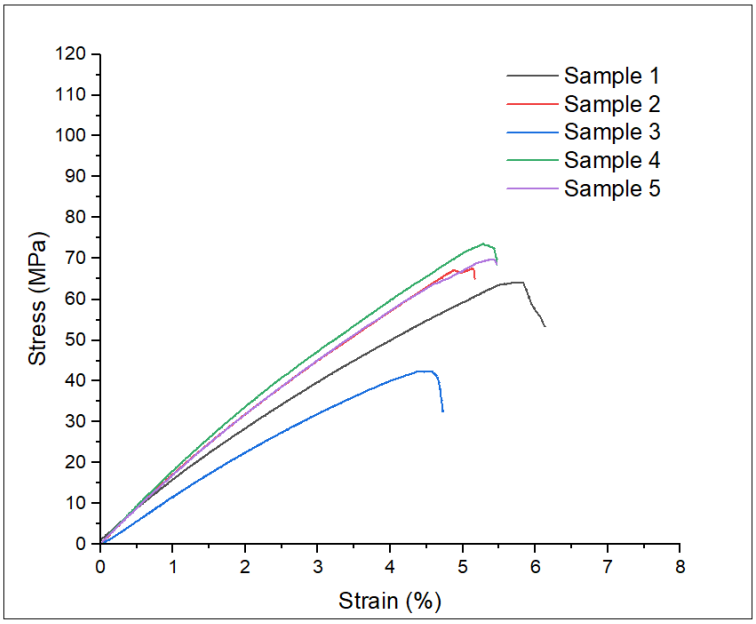

(b)

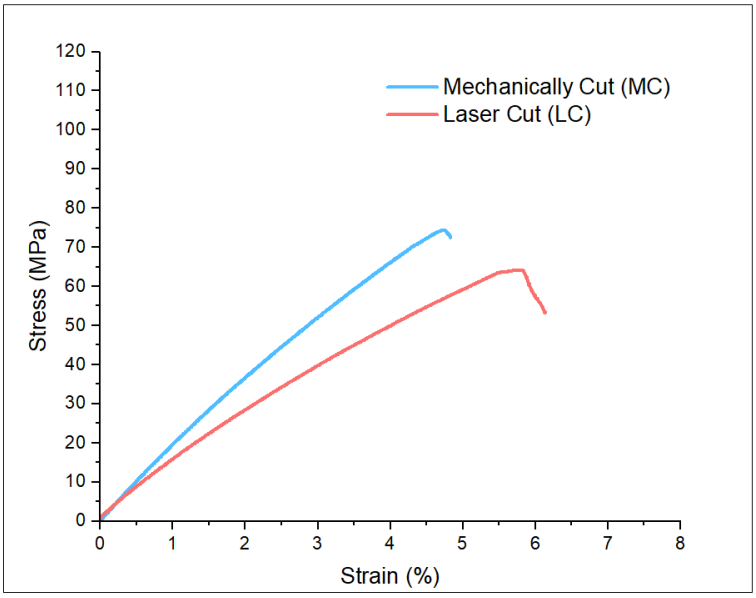

(c)

Fig. 4.7: Tensile stress-strain behavior of woven GFRP composites (a) Mechanically cut, (b) Laser cut and (c) Mechanically cut vs Laser cut (on average values).

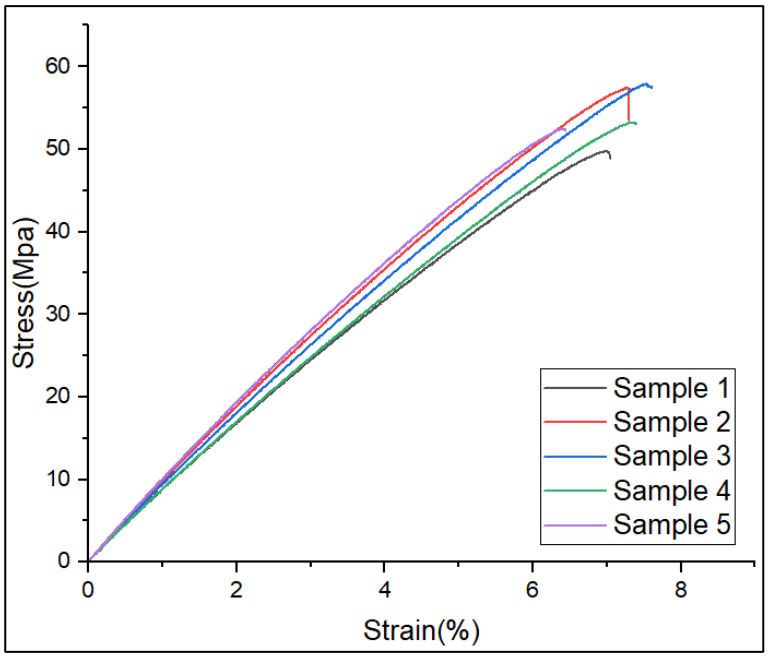
Stress(Mpa)
Strain(%)
0
10
20
30
40
50
60
0
2
4
6
8
Sample 1
Sample 2
Sample 3
Sample 4
Sample 5

(a)

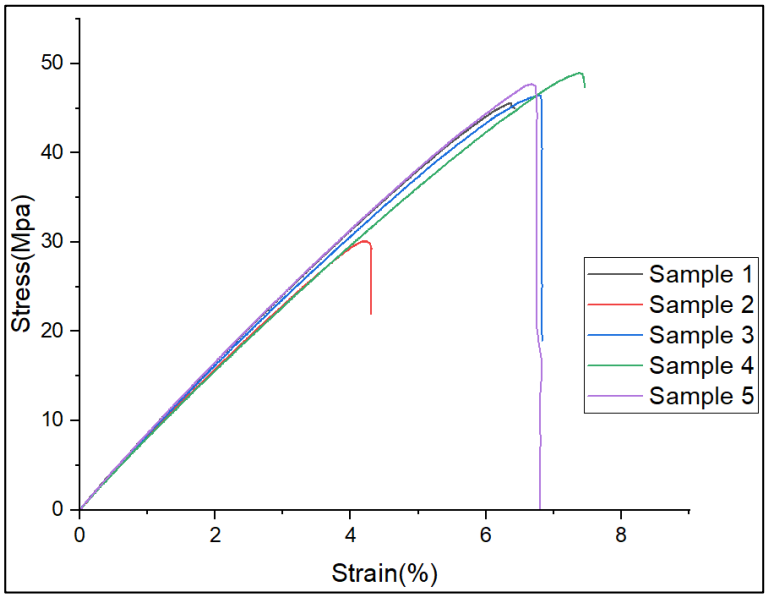
Stress(Mpa)
Strain(%)
0
10
20
30
40
50
0
2
4
6
8
Sample 1
Sample 2
Sample 3
Sample 4
Sample 5

(b)

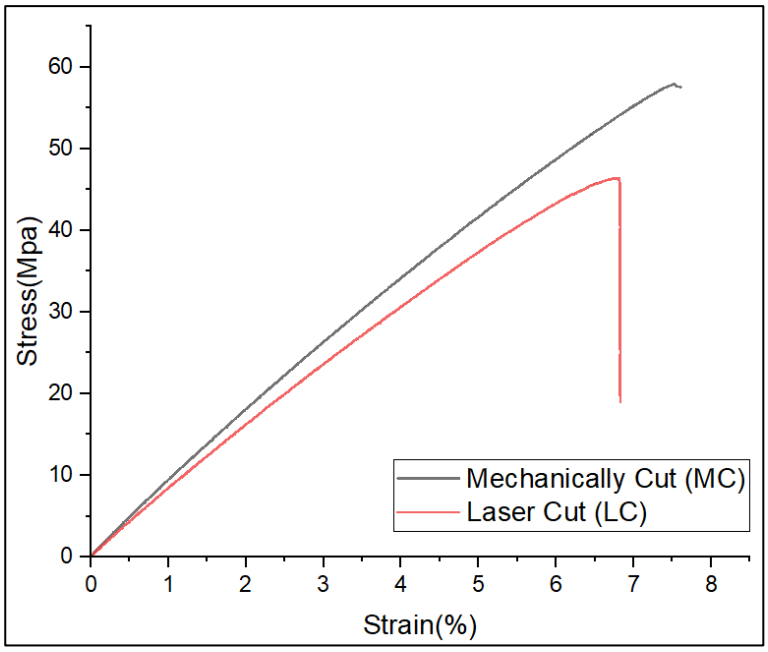

(c)

Fig. 4.8: Tensile stress-strain behavior of random GFRP composites (a) Mechanically cut, (b) Laser cut and (c) Mechanically cut vs Laser cut (on average values).

From Figure 4.8 above, it is evident that the mechanically cut samples reached a higher Ultimate Tensile Strength (UTS) value before failure in comparison to laser-cut samples. This phenomenon is common for both woven and random GFRP. Due to the epoxy thermal damage during laser cutting, mechanical strength at the machined surface got reduced. This peripheral phenomenon had a detrimental effect on the overall strength of the sample. All the curves show that the relationships among the stress and strain are almost linearly rising, followed by quick fall and fracture after the UTS value is reached indicating a brittle mode of failure. This brittle mode failure is consistent with the SEM micrographs of the tensile failure surface. In the SEM it was observed that the individual fibers experienced brittle failure which is characterized by a flat and blunt fiber cutoff.

The UTS, yield strength and elastic modulus are obtained from the tensile test report. Detailed data is shown in Appendix O. The average values along with standard deviations were calculated for each data obtained from several repeated tests. UTS is the maximum stress experienced by samples before breaking. Yield strength is the maximum stress the sample can withstand without permanent deformation. For Woven GFRP, the UTS and yield strength were 85.6 MPa and 25.60 MPa respectively for mechanical cutting while for laser cutting it was 63.4 and 19 MPa respectively. For Random GFRP, the UTS and yield

strength was 54.2 MPa and 16.20 MPa respectively for mechanical cutting while for laser cutting it was 43.8 and 13.20 MPa respectively. Figure 4.9 shows the comparison of woven GFRP UTS and yield strength with error bars for mechanically cut and laser cut samples. Figure 4.10 shows the same information for random GFRP.

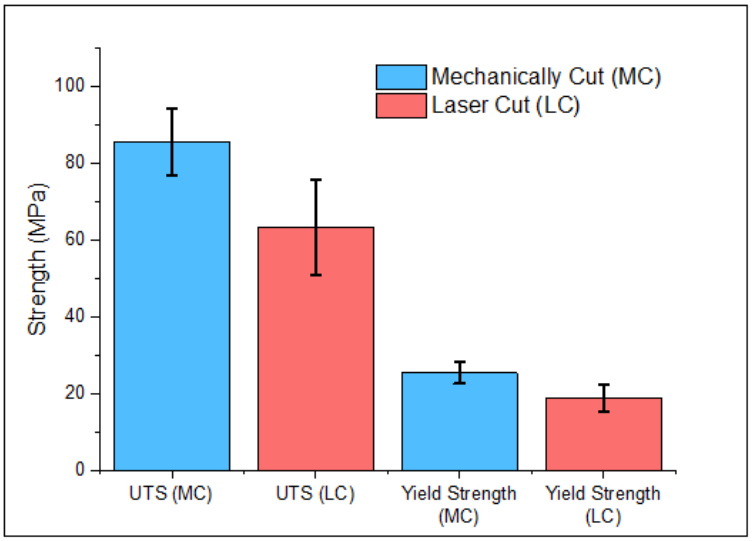

Fig. 4.9: UTS and Yield strength of woven GFRP.

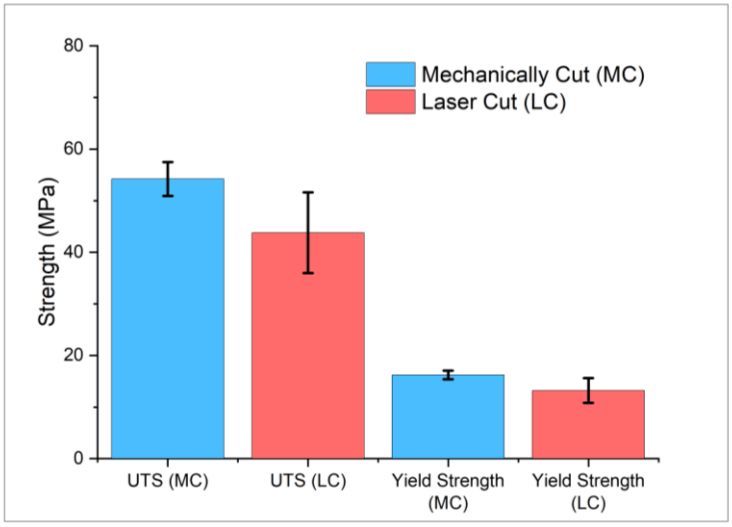

Fig. 4.10: UTS and Yield Strength of random GFRP.

It is observed that for woven GFRP, both UTS and yield strength decreased by 25.93% and 26.4% respectively in laser-cut samples compared to mechanically cut samples. For random GFRP, The UTS and yield strength of laser-cut samples fell by 19.19% and 18.52%, respectively, as compared to mechanically cut samples. The trend of reduction in UTS and

yield strength is similar for both woven and random GFRP where laser cutting caused a reduction in the mechanical properties. The reduction of UTS and yield strength is due to the thermal damage at the machined edge which was also noted during the SEM investigation. The thermal damage during laser cutting deteriorated the bonding between the fibers and the matrix which rendered the machined edge less capable of bearing the tensile stress. As a shole, woven GFRP exhibited higher UTS and yield strength compared to random GFRP as the close-knit configuration of fibers supported each other during the tensile test which ultimately enabled woven GFRP to endure higher UTS before failure.

The Elastic Modulus is the slope of a sample's stress–strain curve in the elastic deformation region. A stiffer material will have a higher elastic modulus. In our study the elastic modulus I obtained directly from the tensile test report. For woven GFRP, the Elastic modulus was 1.47 GPa and 1.30 GPa respectively for mechanical cutting. For Random GFRP, the Elastic modulus was 0.80 GPa and 0.74 GPa respectively for mechanical cutting Figure 4.11 shows the Elastic modulus for woven and random GFRP.

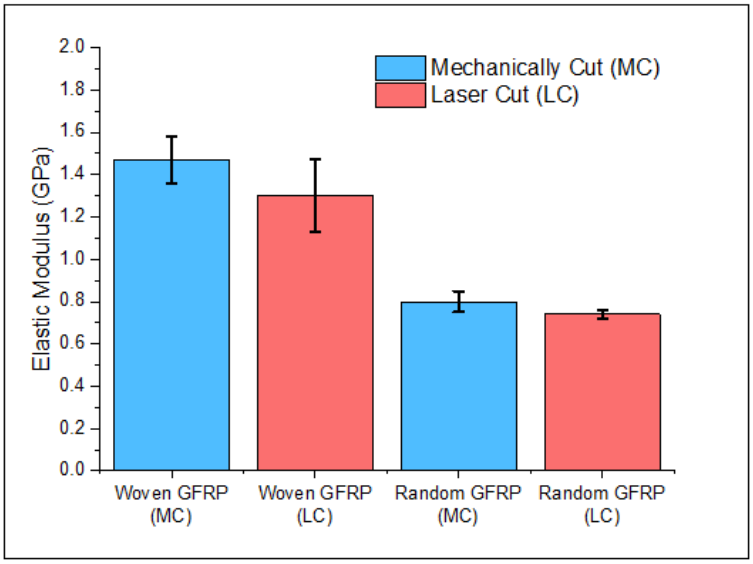

Fig. 4.11: Elastic modulus of woven and random GFRP.

From the above graph it is evident that for Woven and Random GFRP, the elastic modulus decreased by 12% and 7.96% respectively when the material was subjected to laser cutting. This reduction of Elastic modulus is mainly due to the reduced UTS value due to laser cutting. As the elastic modulus is the ratio of stress and strain, the reduction of the stress

value has a linear relationship with the elastic modulus. In general, random GFRP exhibited less elastic modulus than woven GFRP for the same reason.

For validation od results, comparison was made with the material specifications and existing literature. At first, the results of the tensile test was compared with the material specification of the glass fiber and the matrix presented in Appexdix I and Appendix J respectively. In the specifications, the maximum strength of the fiber and matrix was given. The comparison was done for woven GFRP as the specification particularly mentioned the number of fibers in tensile and flexural directions. This comparison in not accurately possible for random GFRP as the number of fibers are not consistent and the fiber orientation is random. Table 4.1 shows the comparison of the results with the specifications.

Table 4.1: Comparison of woven GFRP tensile test results with the specifications.

Direction	Woven Fiber Cloth Strength (MPa) As per Spec	Epoxy Strength (Mpa) As per Spec	GFRP Strength (Mpa) As per Experiment
Tensile (51 Threads per Inch)	86.95	33	85.6

From the table, it is seen that the woven GFRP had a maximum tensile strength of 86.65 MPa as per specification while the experimental result was 85.6. The strength of the epoxy was 33 MPa which acted as a medium for adhesion and load transfer. The experimental result is very close to the specification which affirms the validation of the experimental work.

The UTS value of the GFRP was of utmost interest for this study as this data was used for the development of the predictive model. The validation of this data directly affects the validation of the model. As such, the UTS and Elastic modulus values were also compared to existing literature for validation purpose. Figure 4.12 shows GFRP UTS and elastic modulus from literature.

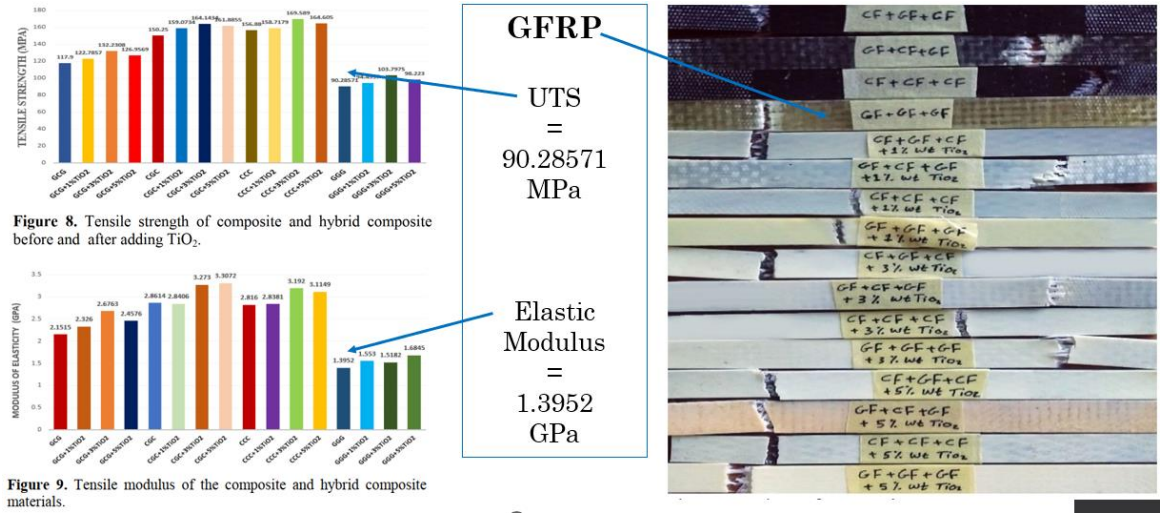

Figure 8. Tensile strength of composite and hybrid composite before and after adding TiO_2.

Figure 9. Tensile modulus of the composite and hybrid composite materials.

Fig. 4.12: UTS and elastic modulus of GFRP from literature (Abass et al., 2021).

The study above was conducted on GFRP composite prepared using materials of similar specifications as this study. From the two graphs, the UTS and Elastic modulus is found as 90.28571 MPa and 1.3952 GPa. In our study, the UTS and Elastic modulus was found as 85.6 MPa and 1.47 GPa. The values from the literature and this study are very close.

The findings of reduced tensile properties due to laser cutting was also compared to the literature. Harada et al investigated the effect of laser cutting on Carbon Fiber Reinforced Plastics (CFRP). Figure 4.13 shows the effect of laser cutting CFRP tensile properties.

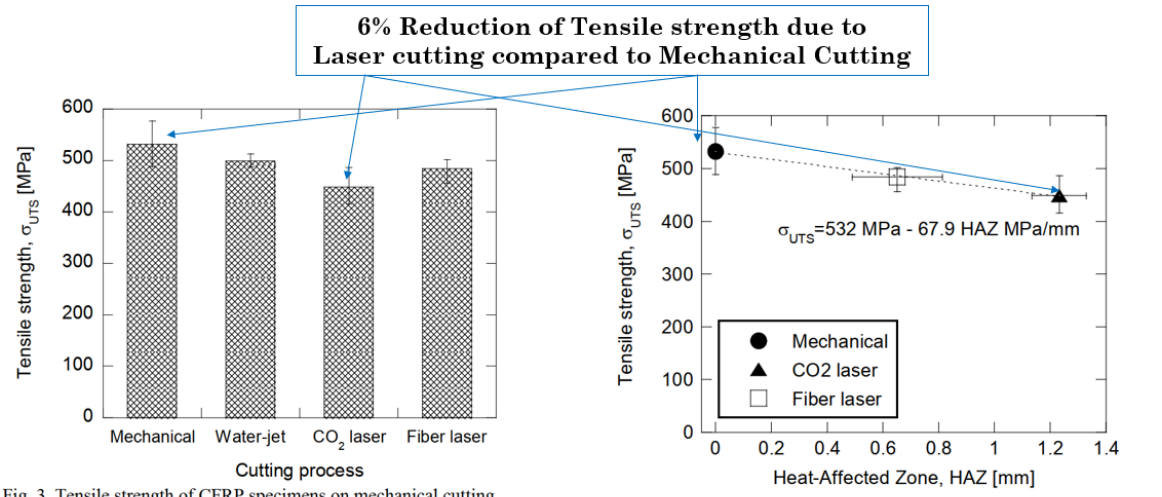

Fig. 3 Tensile strength of CFRP specimens on mechanical cutting, water-jet cutting, CO_2 gas laser cutting and CW single-mode fiber laser cutting.

4 Tensile strength of the tested CFRP, depending on HAZ for laser cutting specimens.

Fig. 4.13: Effect of laser cutting in CFRP from literature (Harada et al., 2012).

The above study was conducted on carbon fiber which has higher UTS values compared to GFRP. However, the effect of laser cutting had similar effect as this study. A 6% decrease of UTS was observed which is consistent with the findings of this study.

4.4 Effect of Fiber Orientation and Machining on Flexural Behavior

The flexural test has been performed utilizing a three-point loading system applied to a simply supported flat GFRP specimen as per ASTM standard D790. Universal testing machine (UTM) PLS100 with a crosshead speed of 5 mm/min was employed to perform this test. Samples were cut into 100mm x 12.7mm x 3mm size. The support span size was 60mm. The flat samples were placed between the support span. The load was applied to the samples at the center of the support span and the load-deflection characteristics were investigated from the flexural test of the GFRP samples. Detailed data from the flexural test was analyzed to calculate Ultimate Flexural Strength (UFS) and Flexural Modulus as per ASTM D790 standard. The test was performed on five samples and the average values along with standard deviations were calculated for each data.

For Woven GFRP, Figures 4.14 and 4.15 present flexural load-deflection behavior of mechanically and laser cut samples for woven and random GFRP respectively. Also, the average values from both mechanically cutting and laser cutting have been shown comparatively to highlight the differences in stress-strain behavior.

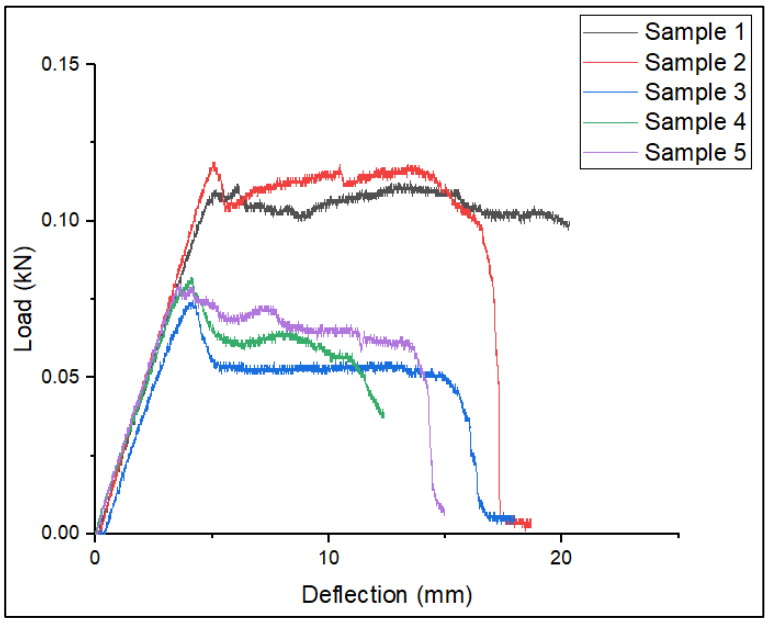

(a)

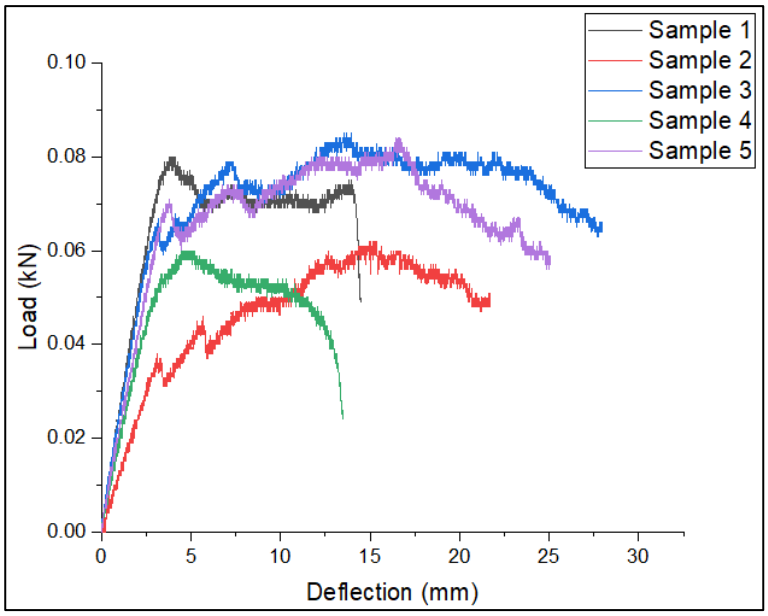

(b)

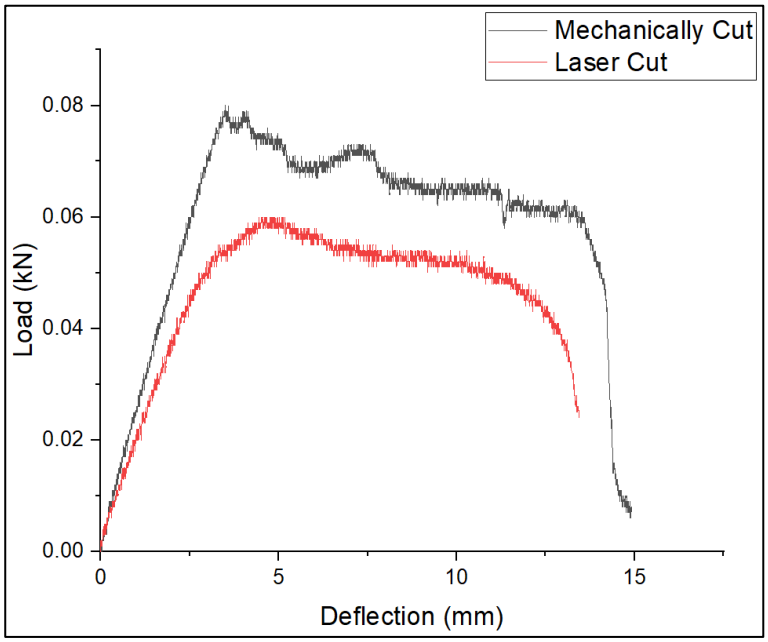

(c)

Fig. 4.14: Flexural load-deflection behavior of woven GFRP composites (a) Mechanically cut, (b) Laser cut and (c) Mechanically cut vs Laser cut (on average values).

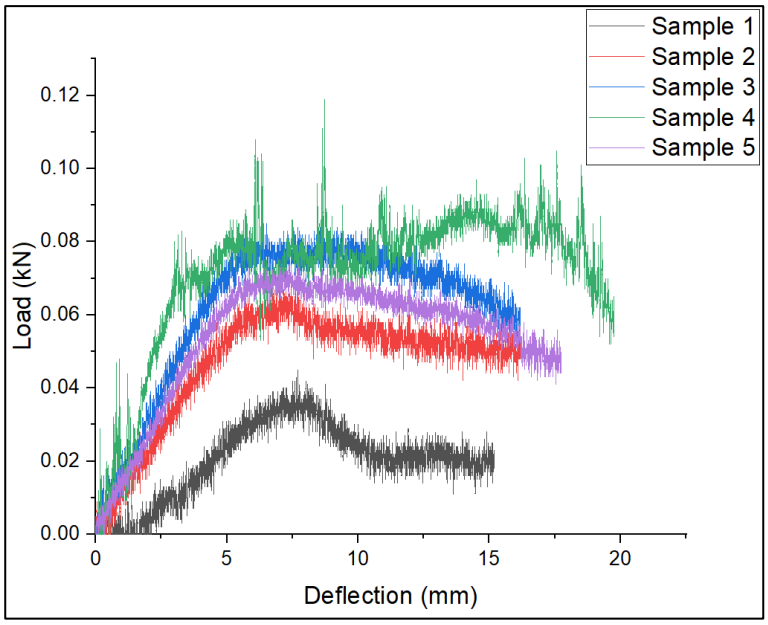
Sample 1
Sample 2
Sample 3
Sample 4
Sample 5
Load (kN)
0.00
0.02
0.04
0.06
0.08
0.10
0.12
0
5
10
15
20
Deflection (mm)

(a)

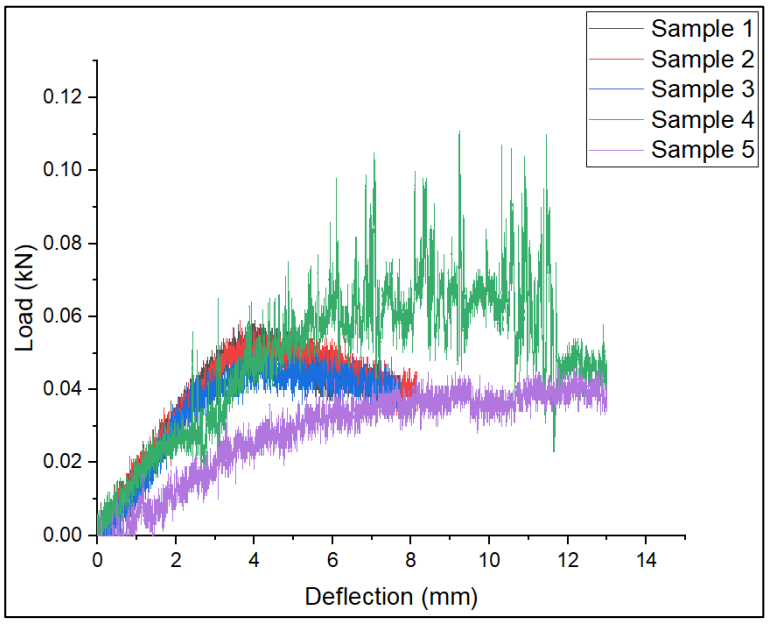
Sample 1
Sample 2
Sample 3
Sample 4
Sample 5
Load (kN)
0.00
0.02
0.04
0.06
0.08
0.10
0.12
0
2
4
6
8
10
12
14
Deflection (mm)

(b)

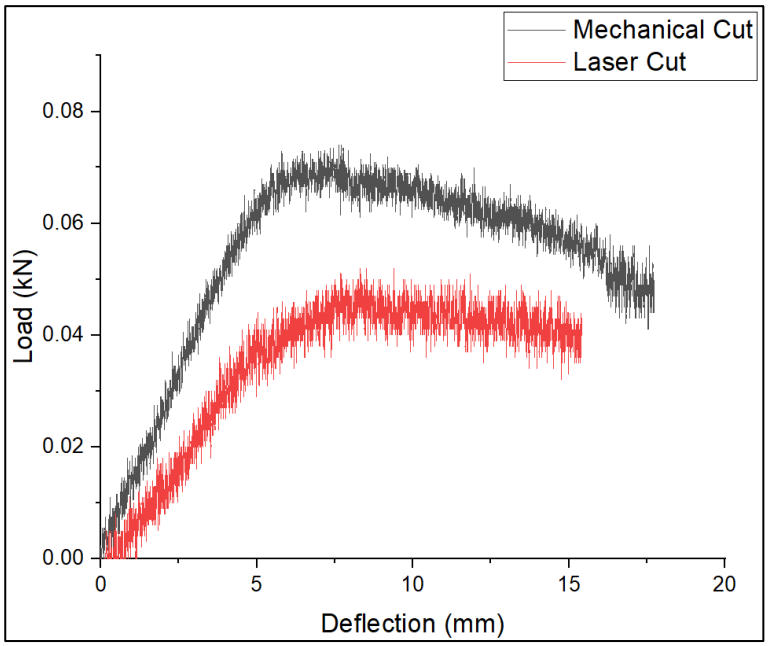

(c)

Fig. 4.15: Flexural load-deflection behavior of random GFRP composites (a) Mechanically cut, (b) Laser cut and (c) Mechanically cut vs Laser cut (on average values).

One clear observation from the load-deflection graphs is that, for random GFRP, a significantly high amount of load value fluctuations are noted compared to woven GFRP. This is visualized by the fuzzy appearance of the random GFRP graphs. The reason behind this is that in this case, the fibers are randomly oriented and separated from each other without a weave. Hence, when the load is applied, the fibers break without any synchronization in a random direction. Unlike the woven GFRP, the fibers are not knit together. In the woven GFRP, the closely knit fibers share the load and when they ultimately break, it happens in groups and in the direction of the fiber weave. Hence, in woven GFRP there is significantly lower load fluctuations. From the comparative average value figures, it is evident that on average, the mechanically cut samples reached a higher load value before failure in comparison to laser-cut samples. This phenomenon is common for both woven and random GFRP. Similar to our findings during the tensile test, due to the epoxy thermal damage during laser cutting, mechanical strength at the machined surface got reduced. This peripheral phenomenon had a detrimental effect on the overall strength of the sample.

Data from the flexural test was used to calculate the Ultimate Flexural Strength (UFS) and Flexural Modulus. Both of these properties were calculated as per the guidelines established in ASTM D790. The average values along with standard deviations were calculated for each data obtained from several repeated tests. UFS is a material property, defined as the maximum stress in a material just before it yields in a flexural test. The formula for calculating UFS is given below:

$$\sigma = \frac{3PL}{2bd^2} \tag{4.1}$$

Where:

σ = UFS (MPa)

P = Maximum load on the load deflection curve (N)

L = Length of support span (mm)

b = Width of sample (mm)

d = Thickness of beam (mm)

For Woven GFRP, the UFS was 73.66 MPa and 56.63 MPa for mechanical cutting and laser cutting respectively. For Random GFRP, the UFS was 52.43 MPa and 41.34 MPa for mechanical cutting and laser cutting respectively. Figure 4.16 shows the UFS of Woven and Random GFRP.

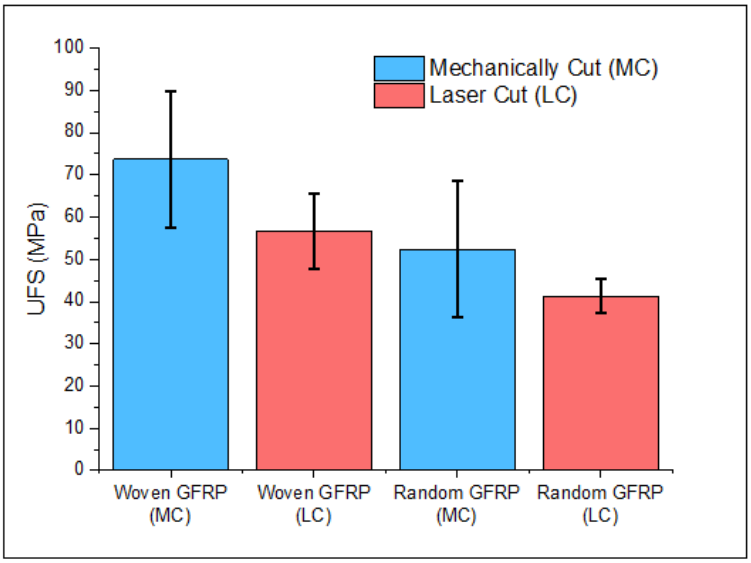

Fig. 4.16: UFS of woven and random GFRP.

It is noted that for woven GFRP, UFS decreased by 23% in laser-cut samples compared to mechanically cut samples. For random GFRP, this decrease was 21%. Similar to tensile test, the reduction of UFS and yield strength is due to the thermal damage at the machined edge which was also noted during the SEM investigation. The thermal damage during laser cutting deteriorated the bonding between the fibers and the matrix which rendered the machined edge less capable of bearing the flexural stress. Again, woven GFRP exhibited higher UFS and yield strength compared to random GFRP as the close knit configuration of fibers supported each other during this which ultimately enabled woven GFRP to endure higher UTS before failure.

The flexural modulus or bending modulus is an intensive property that is computed as the ratio of stress to strain in flexural deformation, or the tendency for a material to resist bending. The formula for flexural modulus is given below:

$$E = \frac{L^3 m}{4bd^3} \tag{4.2}$$

Where:

E = Flexural Modulus (MPa)

L = Length of support span (mm)

b = Width of sample (mm)

d = Thickness of beam (mm)

m = Slope of the tangent to the initial straight-line portion of the load-deflection curve, (N/mm)

For woven GFRP , the flexural modulus was 3.41 GPa and 2.91 GPa for mechanical cutting and laser cutting respectively. For Random GFRP, the flexural modulus was 2.14 GPa and 2.09 GPa for mechanical cutting and laser cutting respectively. Figure 4.17 shows the Flexural Modulus of Woven and Random GFRP.

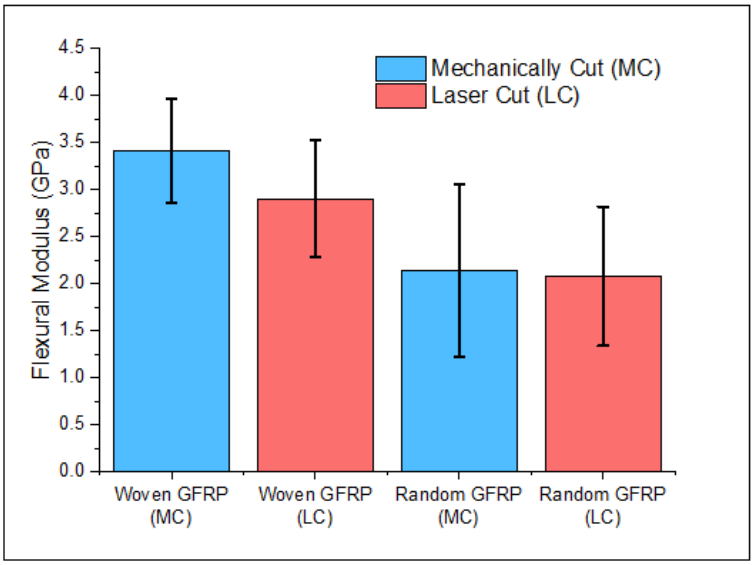

Fig. 4.17: Flexural modulus of woven and random GFRP.

From the above graph it is found that for Woven and Random GFRP, the flexural modulus decreased by 15% and 2% respectively when the material was subjected to laser cutting. This reduction of flexural modulus is mainly due to the reduced UFS value due to laser cutting. As the elastic modulus is the ratio of stress and strain, the reduction of the stress value has a linear relationship with the flexural modulus. In general, random GFRP exhibited less flexural modulus than woven GFRP for the same reason.

For validation purpose, the results of the flexural test was compared with the material specification of the glass fiber and the matrix presented in Appendix I and Appendix J respectively. In the specifications, the maximum strength of the fiber and matrix was given. The comparison was done for woven GFRP as the specification particularly mentioned the number of fibers in tensile and flexural directions. This comparison in not accurately possible for random GFRP as the number of fibers are not consistent and the fiber orientation is random. Table 4.2 shows the comparison of the results with the specifications.

Table 4.2: Comparison of woven GFRP flexural test results with material specifications.

Direction	Woven Fiber Cloth Strength (MPa) As per Spec	Epoxy Strength (Mpa) As per Spec	GFRP Strength (Mpa) As per Experiment
Flexural (38 Threads per Inch)	53.01	33	73.66

For the flexural strength, the experimental value was 73.66 MPa where as per specification, the fiber cloth and the epoxy has the strength of 53.01 MPa and 33 MPa respectively. It is to be noted that the glass fiber cloth had more fibers in the tensile direction (51 threads per inch) compared to the flexural direction (38 threads per inch). Also, due to the woven nature of the glass fiber cloth, the threads in the flexural direction are also suppored by the threads of the tensile direction. As such, the experimental value of the flexural strength was found more than the maximum strength of the fibers only. This also affirms that the fibers are the main load bearing members of the GFRP while the matrix provides adhesion and load transfer.

Several researchers have also experimented with the flexural behaviors of GFRP. They have prepared GFRP samples with different reinforcements and matrix along with the addition of micro and nano fillers. Hence, there are a lot of literature reporting different results for different compositions. The research conducted by Kaleg et al. specifically explored the flexural properties of GFRP with similar composition as this study. Their results are shows in Figure 4.18.

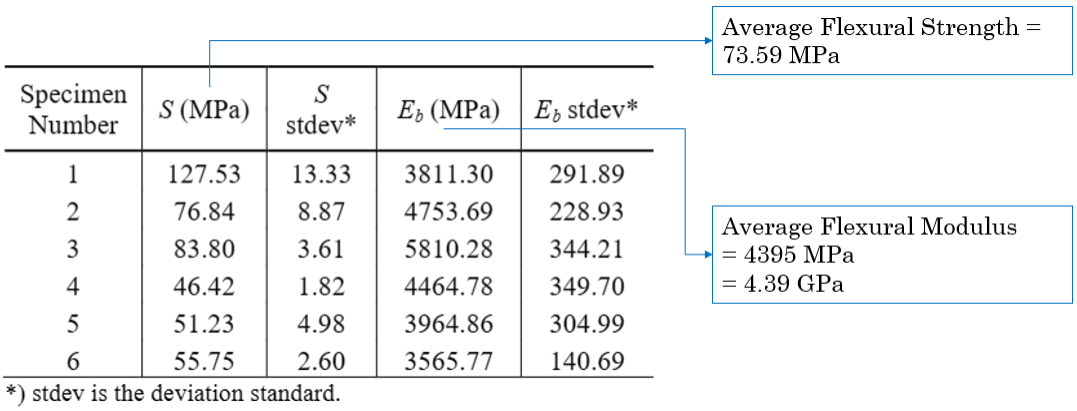

Specimen Number	S (MPa)	S stdev*	E_b (MPa)	E_b stdev*
1	127.53	13.33	3811.30	291.89
2	76.84	8.87	4753.69	228.93
3	83.80	3.61	5810.28	344.21
4	46.42	1.82	4464.78	349.70
5	51.23	4.98	3964.86	304.99
6	55.75	2.60	3565.77	140.69

*) stdev is the deviation standard.

Fig. 4.18: GFRP flexural properties from literature (Kaleg et al., 2018).

From the above results it is seen that the researchers found GFRP flexural strength as 73.59 MPa and Flexural Modulus as 4.39 GPa. Their findings are within the ballpark of the findings of this study.

4.5 Effect of Fiber Orientation and Machining on Microhardness

Vickers Micro Hardness testing machine TMHV-10MDT manufactured by TMTeck Instrument Company Ltd. was used in this experiment. This machine has a diamond indenter of pyramid shape at an angle of 136°. Samples were cut into a 30mm x 30mm x 3mm size and tested on the tester as per ASTM standard E384. The test load was selected as 300 grams. During the test, the pyramid indenter presses on the sample with the prescribed test load. Accordingly, a pyramid shape indentation is made on the sample. Attached microscopes are then used to measure the two diagonals of the pyramid shape. Then the Vickers Micro Hardness value (HV) is calculated and displayed in the machine. Five samples had been tested from both mechanically cut and laser cut GFRP. Ten HV readings are taken from each sample to calculate the average HV and standard deviation for each sample. Readings were taken at various locations of the sample. Some readings were taken at close proximity to the machine edge while some readings were taken at the center. Figure 4.19 shows the Vickers microhardness results of woven and random GFRP.

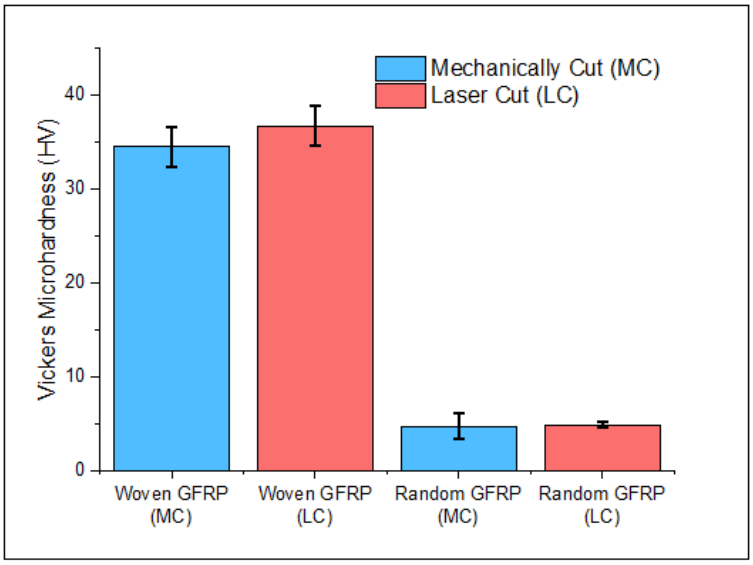

Fig. 4.19: Vickers microhardness results of woven and random GFRP.

For woven GFRP, it is observed that for mechanically cut samples average HV and standard deviation are 34.54 and 2.14 respectively. And for laser cut samples average HV and

standard deviation for are 36.71 and 2.11 respectively. For Random GFRP, mechanically cut samples' average HV and standard deviation are 4.82 and 1.37 respectively. And for laser cut samples average HV and standard deviation for are 4.97 and 0.34 respectively.

It is evident that for both woven GFRP and random GFRP, the HV values for mechanically cut and laser cut samples are similar. This is because the laser cutting only had a peripheral effect on the material and did not affect the material substrate. Also, woven GFRP exhibited significantly increased hardness value compared to random GFRP. This is due to the close-knit configuration of woven GFRP where the fibers provide resistance to the indenter. For random GFRP, the fibers are randomly oriented and have gaps within them. Unlike the woven GFRP, the random GFRP fibers do not provide such resistance to the indenter as they are not closely knit. As such, random GFRP exhibits lower hardness value.

From the literature review, it is discovered that the Vickers microhardness varies from 20 HV to 200 HV for different compositions and fillers. The study conducted by Ghani and Mahmud experimented with similar GFRP and similar methodology as this study. Their results are shown in Figure 4.20. From the figure, it can be inferred that they found average microhardness value of GFRP as 65.12 HV.

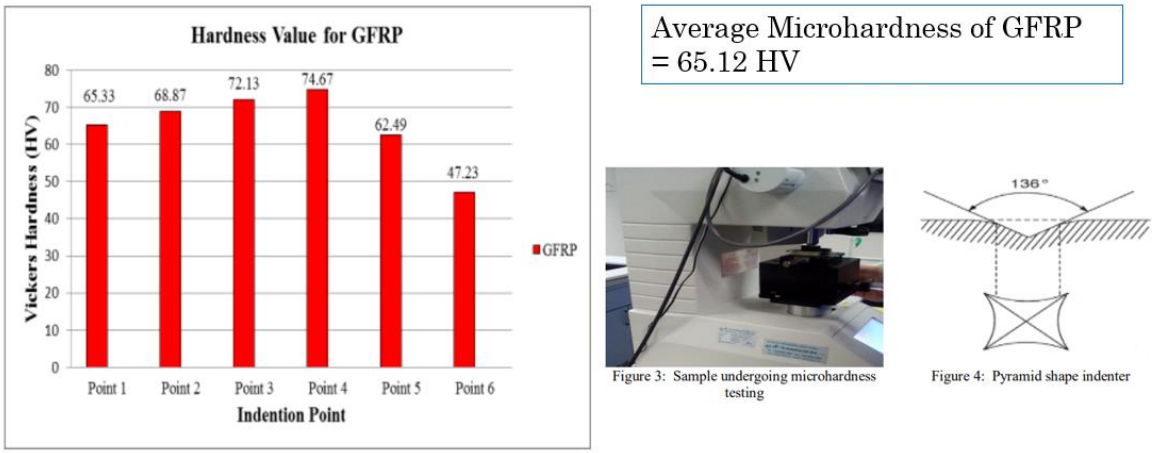

Figure 3: Sample undergoing microhardness testing

Figure 4: Pyramid shape indenter

Fig. 4.20: GFRP microhardness value from literature (Ghani and Mahmud, 2017).

Another study conducted by Mohamed et al explored the effect of cellulose nanocrystal reinforcement in GFRP they also varied the microhardness test for different indenter loading. Figure 4.21 shows the results of their study.

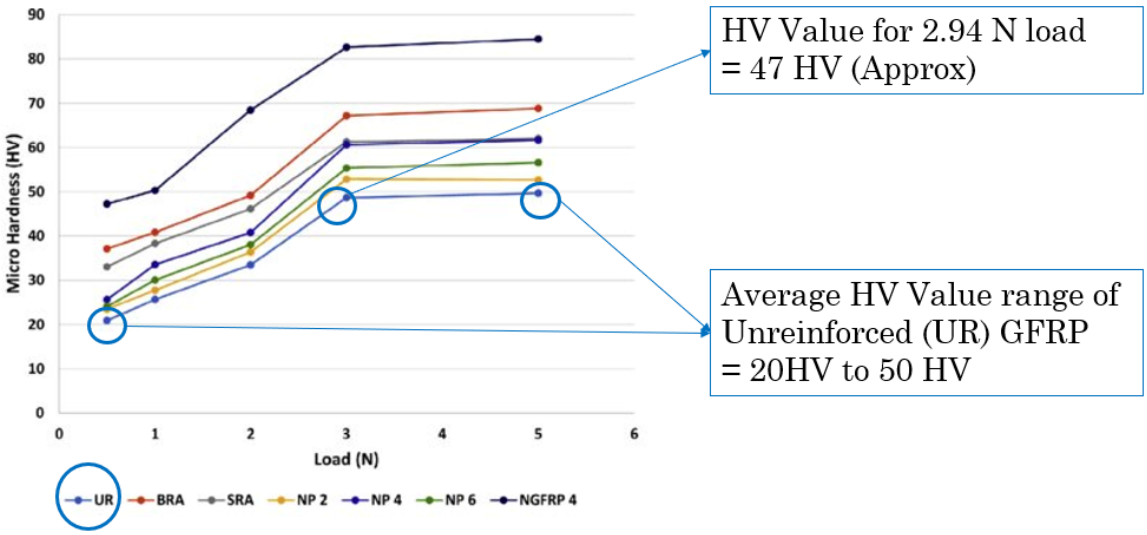

Fig. 4.21: GFRP microhardness value from literature with different load (Mohamed et al., 2018).

It is seen from the graph that the average GV value of plain GFRP indicated by UR; which means unreinforced by any cellulose nanocrystals, had HV values ranging from 20 – 50 for different indenter loading. For direct comparison to our study, the load value of 2.94 is referred (Our selected load was 300g which equates to 2.94N) and the corresponding HV value is found as 47 HV.

Both the above studies present results which are somewhat nearby to our results of 34.54 HV. The variations in results can be contributed to several different factors including production flaws, curing condition, material condition, fiber weave and many more.

4.6 Effect of Fiber Orientation and Machining on Tensile Fracture

For Woven GFRP, SEM Micrographs of the tensile fractured surface are taken in 150x, 300x and 700x magnification and 15 kV setting. For Random GFRP, The tensile fractured surface was micrographed at 150x, 300x, and 500x magnification at 10 keV. The individual configurations are chosen to have the best possible image clarity and magnification. Figure 4.22 shows the SEM image of the tensile fracture surface of mechanical and laser-cut samples for woven GFRP. Figure 4.23 shows the same information for random GFRP.

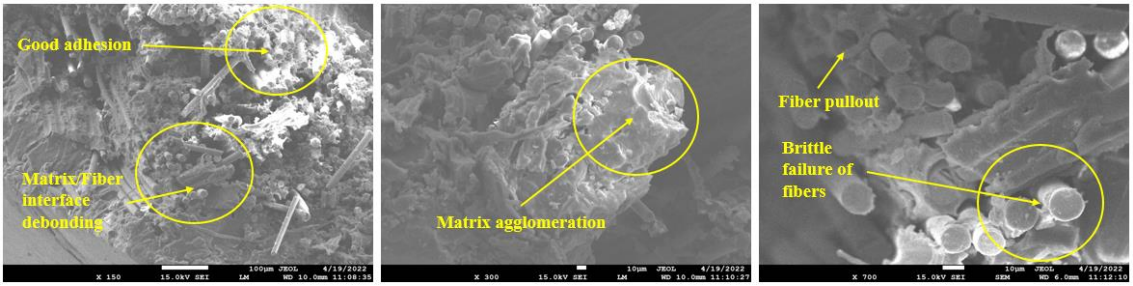

(a)

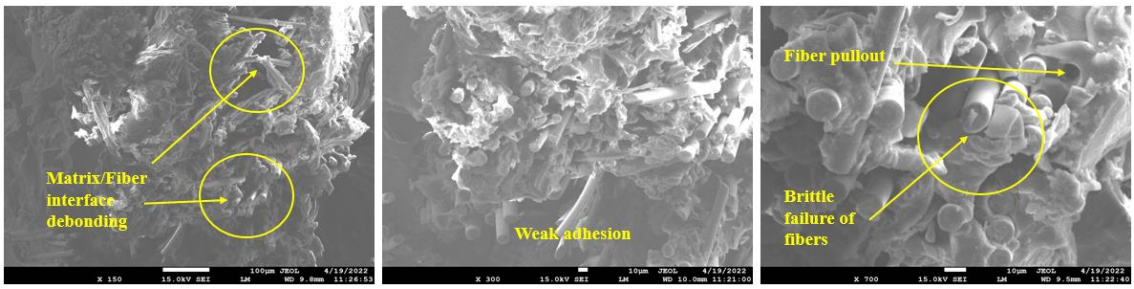

(b)

Fig. 4.22: SEM micrographs of woven GFRP tensile fractured surface

(a) Mechanically cut, (b) Laser cut.

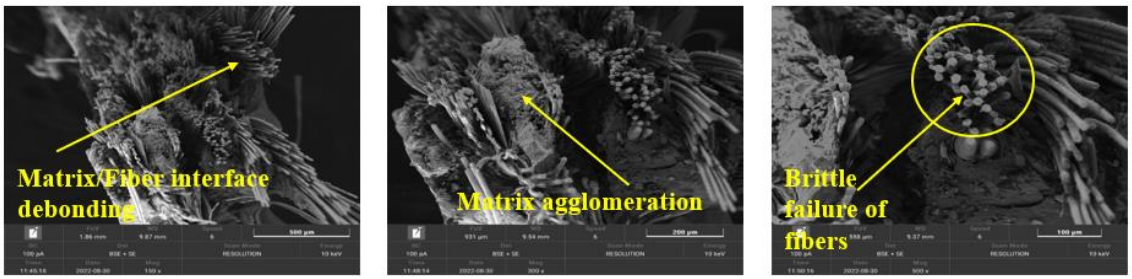

(a)

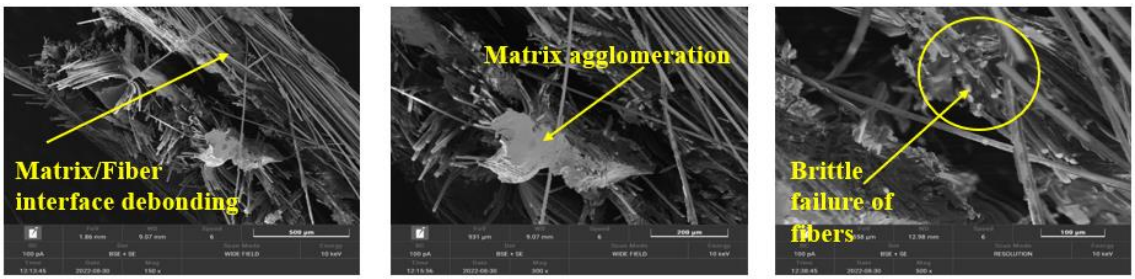

(b)

Fig. 4.23: SEM micrographs of random GFRP tensile fractured surface

(a) Mechanically cut, (b) Laser cut.

From the above Figures, it is observed that in both types of machining, the predominant reason for tensile fracture of the composite is matrix/fiber interface debonding, brittle fracture of fibers and fiber pullout. Also, in the laser-cut sample, some areas of weaker adhesion are observed compared to the mechanically cut sample. In general, the nature of tensile fracture is similar in both mechanical and laser cutting. These observations are common for woven and random GFRP. These findings are in agreement with the findings of microhardness behavior where it was evident that the laser cutting did not affect the material substrate. Accordingly, the nature of tensile fracture remained similar.

There is significant literature on the SEM analysis of GFRP tensile fracture. The results reported by the researchers remain in unison in terms of fiber pullout and the brittle more of failure. Although the fiber orientation and matrix cracking largely depends on material selection and production method used. Figure 4.24 shows the SEM micrographs of GFRP tensile failure from relevant literature. The images show findings similar to this study.

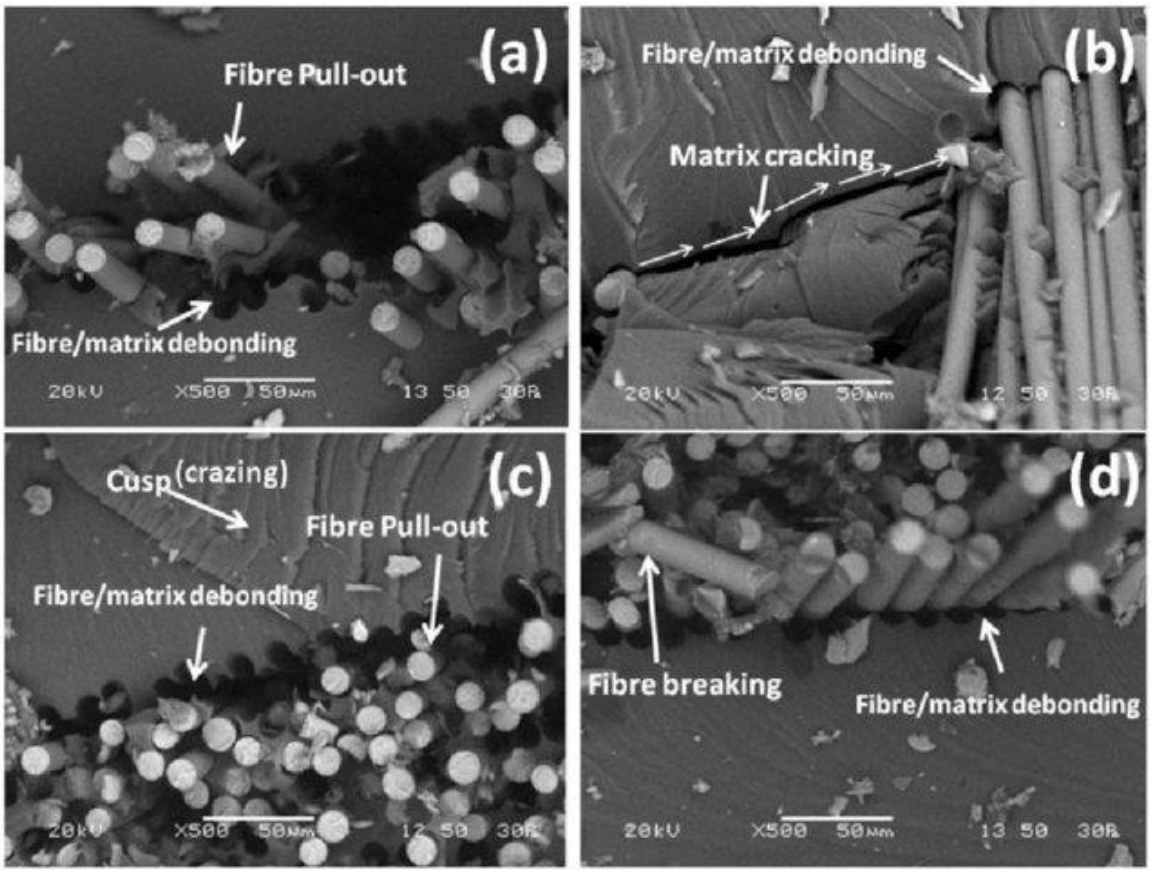

Fig. 4.24: SEM micrographs of GFRP tensile fracture surface from literature (Beura et al., 2018).

4.7 Effect of Thermal Aging on GFRP Color

During the thermal aging process at 100°C (SGN 6,7,8 and 9), very mild smoke and a burning smell were noticed. This smoke and smell effect became more noticeable at 150°C (SGN 10,11,12 and 13). At 200°C (SGN 14,15,16 and 17) the smoke and burning smell were clearly noticeable. This was expected as the glass transition temperature (Tg) of the epoxy is 63°C.

Also, at 150°C (SGN 10,11,12 and 13), the tensile test samples started to show color changes with the introduction of very slight shades of brown. At 200°C (SGN 14,15,16 and 17) this color change effect became apparent. In SGN 14, the color was light brown. As the thermal aging time increased, the brown color became progressively darker in SGN 15, 16 and 17. The burning smell and color changes are mainly related to the oxidation process. The color change effect due to thermal aging is shown in Figure 4.25.

SGN (Left to Right) and associated thermal aging variables:
2 = 50°C 30 mins
3 = 50°C 60 mins
4 = 50°C 90 mins
5 = 50°C 120 mins

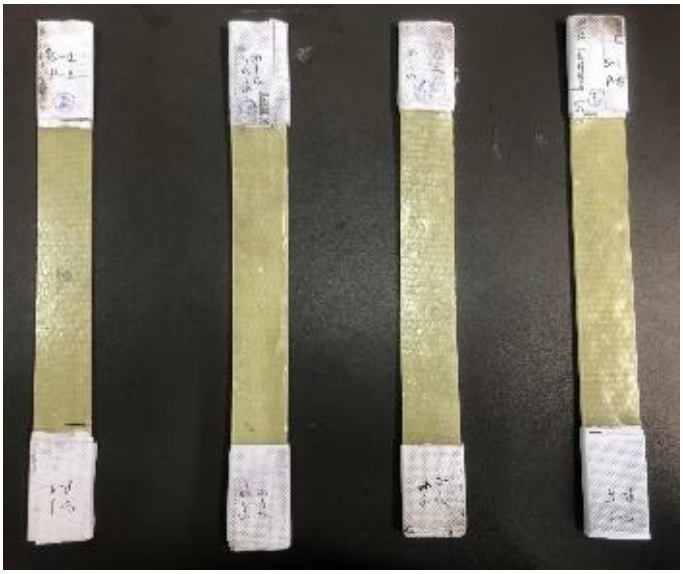

(a)

SGN (Left to Right) and associated thermal aging variables:

6 = 100°C 30 mins

7 = 100°C 60 mins

8 = 100°C 90 mins

9 = 100°C 120 mins

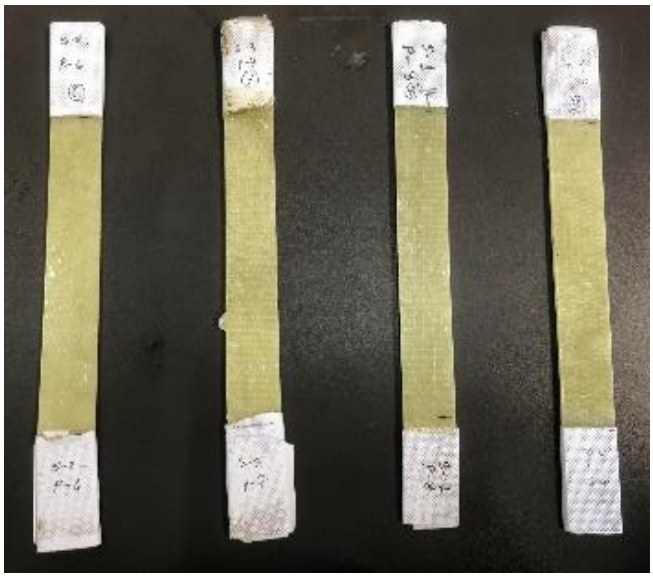

(b)

SGN (Left to Right) and associated thermal aging variables:

6 = 150°C 30 mins

7 = 150°C 60 mins

8 = 150°C 90 mins

9 = 150°C 120 mins

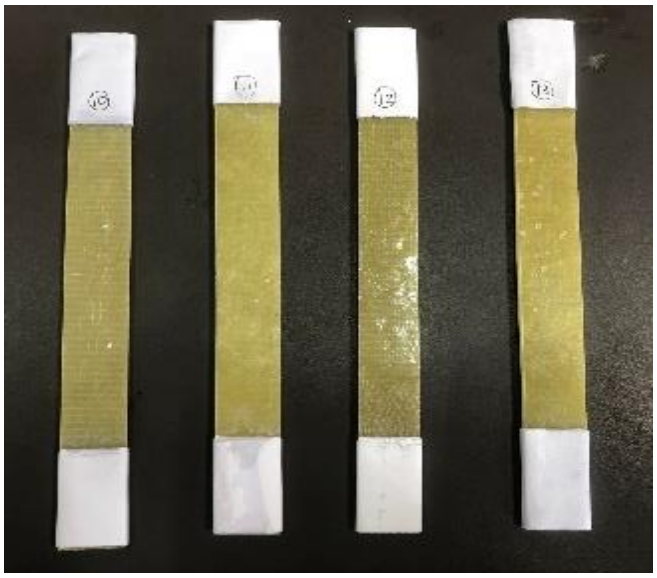

(c)

SGN (Left to Right) and associated thermal aging variables:

14 = 200°C 30 mins

15 = 200°C 60 mins

16 = 200°C 90 mins

17 = 200°C 120 mins

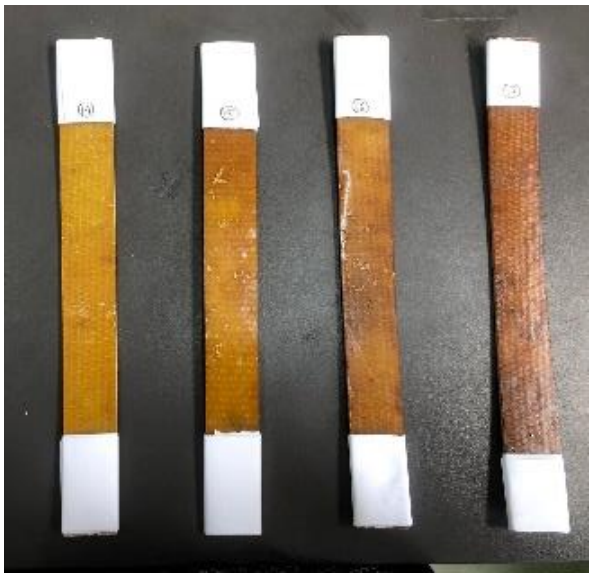

(d)

Fig. 4.25: GFRP color change effect due to thermal aging
(a) SGN 2-5, (b) SGN 6-9, (c) SGN 10-13 and (d) SGN 14-17.

Several researchers have experimented with the thermal aging of GFRP. But one researcher in particular put emphasis on the color change of epoxies due to thermal aging and used this as an identifier to develop a predictive model. This particular study done by Doblies et al. is of interest to our work. Figure 4.26 shows this color change due to the thermal aging of epoxy.

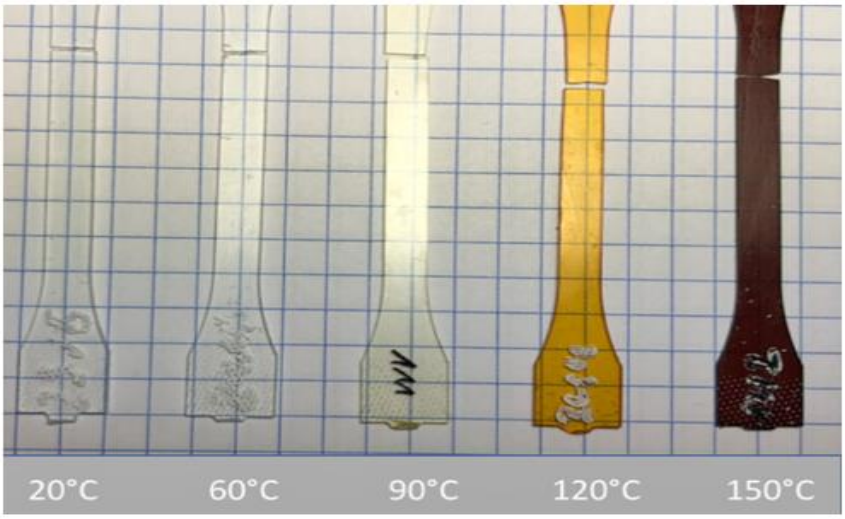

Fig. 4.26: Color change of epoxy due to thermal aging from literature (Doblies et al., 2019).

In the above study, only epoxy was used in the absence of a reinforcing element. It is observed that the epoxy demonstrates a clear yellowing at 120°C. As the temperature is increased to 150°C the yellowing color becomes dark brown. This trend of color change is in agreement with our findings. Also, according to the existing literature, a higher temperature and longer exposure time typically result in a darker color. (Lan et al., 2022). Although, the complete details are not fully understood yet (Bellenger and Verdu, 1985; Krauklis and Echtermeyer, 2018). Researchers have proposed reactive sites and respective reactions to chemically explain the micro phenomena. Most notably; the carbonyl formation in the epoxy backbone due to thermo-oxidation as the cause for the yellowing of the material is similar to our study (Krauklis and Echtermeyer, 2018).

4.8 Effect of Thermal Aging on GFRP Tensile Properties

With three samples in each SGN, a total of 51 samples from 17 SGNs underwent the tensile test. 03 thermally unaged samples were first put through tensile testing. From the tensile test data, max strain (%), UTS (MPa), yield strength (MPa), elastic modulus (MPa) and tangent modulus (MPa) were calculated. Afterward, 48 thermally aged samples underwent tensile testing. The average values of the 3 samples in each group were considered for the respective group. Finally, a total of 17 sets of tensile test data was gathered comprising UTS, Max Strain and Yield Strength. This dataset is presented in Appendix R. From this dataset the effect of thermal aging on UTS, Max Strain and Yield Strength is shown individually with varying SGN.

In the present work, Ultimate Tensile Strength (UTS) is the mechanical property of interest. As such, it is analyzed with much deliberation. Figure X shows the change of UTS due to thermal aging. The Figure is divided into 5 separate graphs to aid the visualization of the thermal aging effect due to a fixed temperature and increasing aging time. Finally, graph 4.27 (e) shows the effect with all sample group numbers sequentially. The black bar in this graph represents the UTS value for unaged samples.

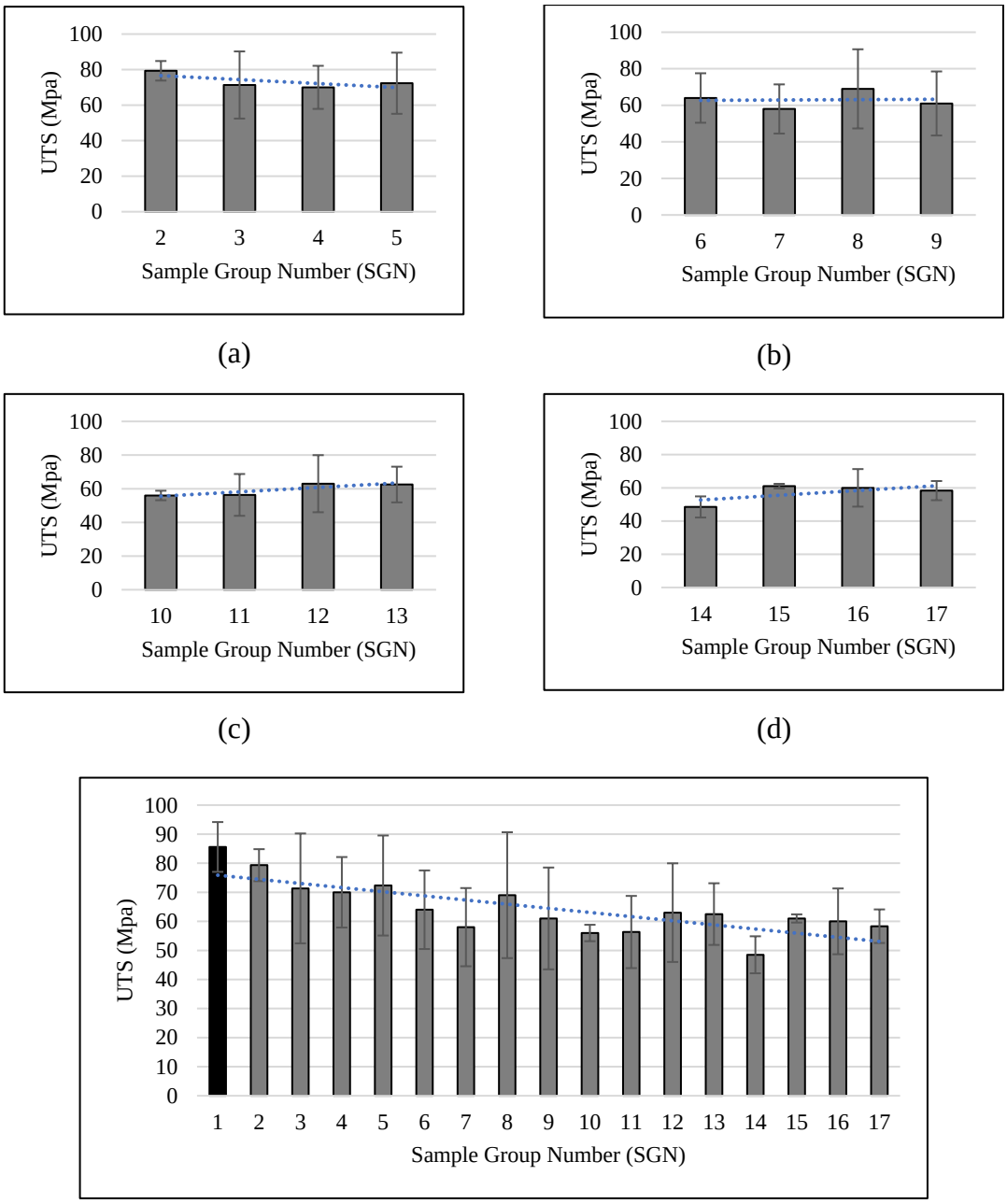

Fig. 4.27: Change of UTS due to thermal aging for different SGN
(a) SGN 2-5, (b) SGN 6-9, (c) SGN 10-13, (d) SGN 14-17 and (e) SGN 1-17.

It is observed that for SGN 2-5 a decreasing UTS, a clear trend is observed. SGN 6-9 shows a more consistent rend with UTS values increase and decrease in an oscillating manner. For SGN 10-13 the UTS values slowly increase. For SGN 14-17, the UTS values increase initially but later reach a plateau. Finally, for graph (e) there is an overall trend of decreasing UTS is observed although there are noticeable variations as mentioned earlier. These variations in UTS due to different thermal aging are consistent with the literature. The initial

decrease in UTS below and slightly over the Tg is expected due to the epoxy being rubbery and causing voids inside the material substrate. However, the increase in UTS at higher temperatures (SGN 11,12,13,15,16,17) is not fully understood by the auhor and and requires further research.

Similar to UTS, Figure 4.28 shows the change of Max Strain due to thermal aging. The Figure is divided into 5 separate graphs to aid the visualization of the thermal aging effect due to a fixed temperature and increasing aging time. Finally, graph 4.28 (e) shows the effect with all sample group numbers sequentially. The black bar in this graph represents the Max Strain value for unaged samples.

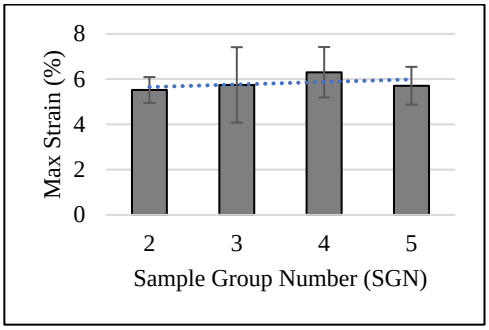

(a)

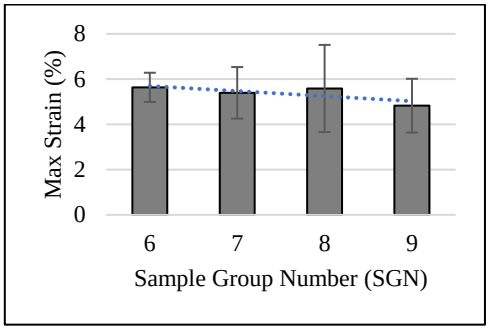

(b)

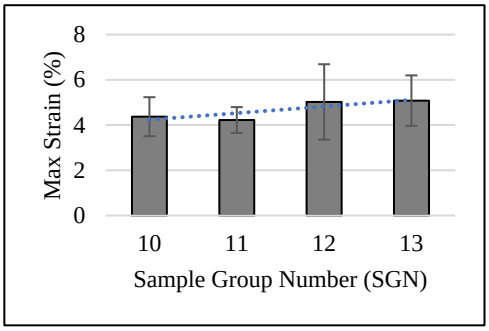

(c)

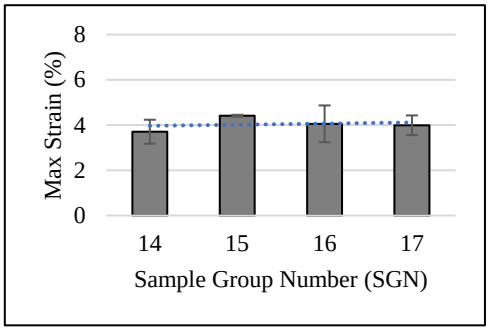

(d)

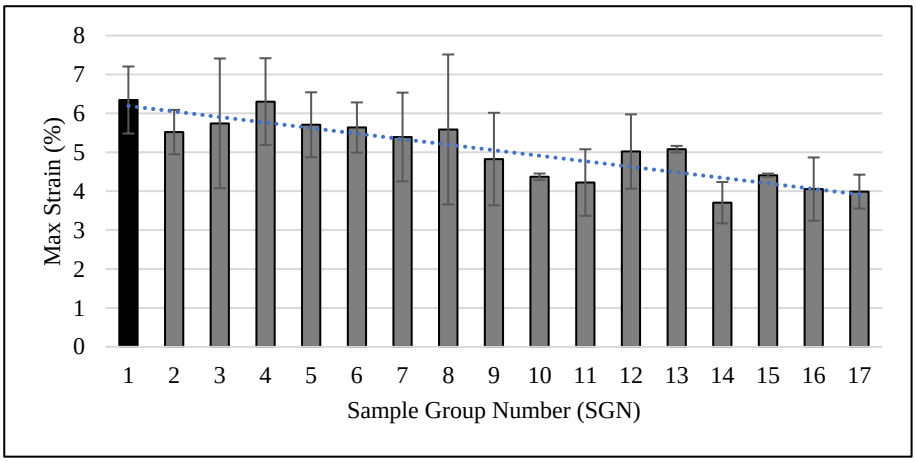

(e)

Fig. 4.28: Change of max strain (%) due to thermal aging for different SGN (a) SGN 2-5, (b) SGN 6-9, (c) SGN 10-13, (d) SGN 14-17 and (e) SGN 1-17.

Also, Figure 4.29 shows the change in Yield Strength due to thermal aging. The Figure is divided into 5 separate graphs to aid the visualization of the thermal aging effect due to a fixed temperature and increasing aging time. Finally, graph 4.29 (e) shows the effect with all sample group numbers sequentially. The black bar in this graph represents the Yield Strength value for unaged samples.

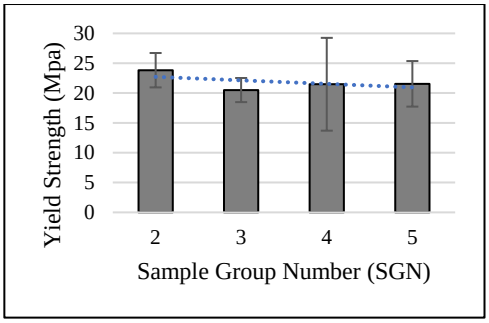

(a)

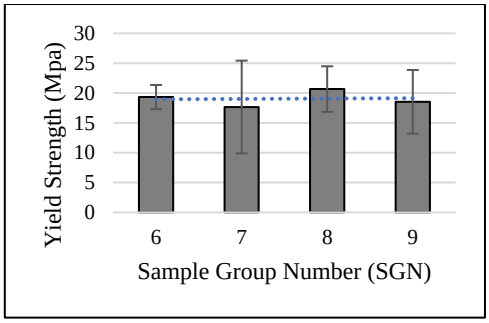

(b)

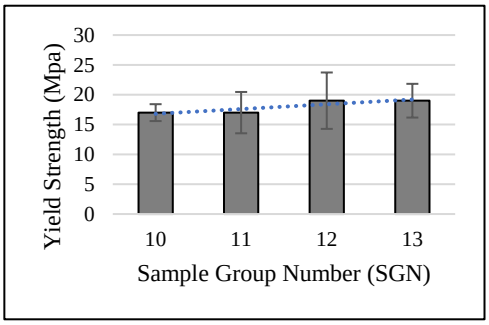

(c)

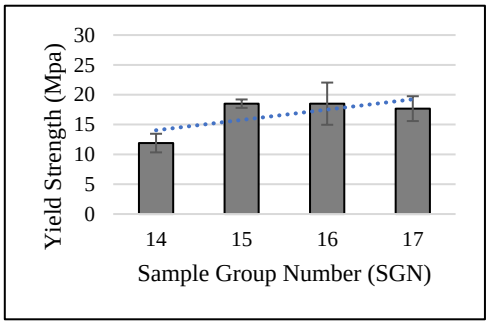

(d)

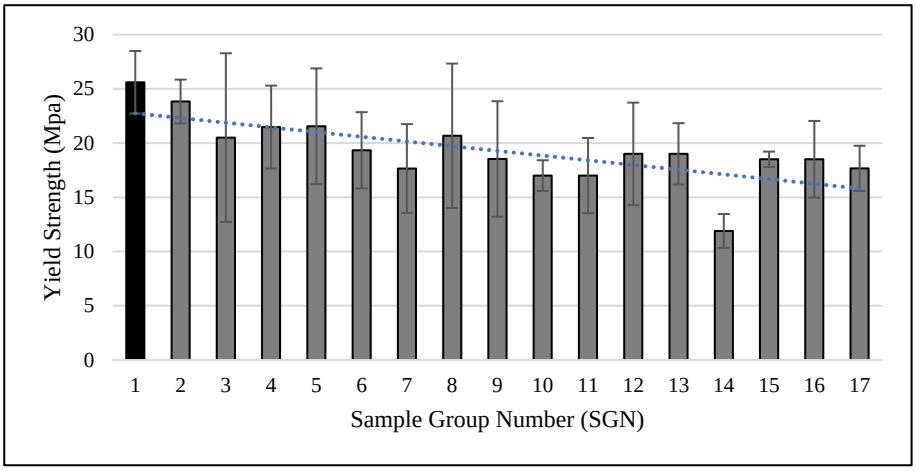

(e)

Fig. 4.29: Change of yield strength due to thermal aging for different SGN
(a) SGN 2-5, (b) SGN 6-9, (c) SGN 10-13, (d) SGN 14-17 and (e) SGN 1-17.

As a general observation, from Figure 4.15 to 4.17, it is revealed that a gradual decrease in UTS, Max Strain and Yield strength values occurred as samples were exposed to increasingly higher temperatures during the thermal aging process. The highest value was obtained from the unaged samples while the lowest value was found from the thermally aged samples at 200°C 30 mins. The percentile decreases of UTS, Max Strain and Yield strength values were 43.34%, 41.48% and 53.52% respectively between the two extremes. The high amount of scattering in the mechanical properties after thermal aging is consistent with the literature.

Further analysis of the dataset in Appendix R was performed to see variations in UTS of SGN 2 – 17, due to the variations in thermal aging temperature and time separately. Figure 4.30 shows the change of UTS due to thermal aging temperature and Figure 4.31 shows the change of UTS due to thermal aging time.

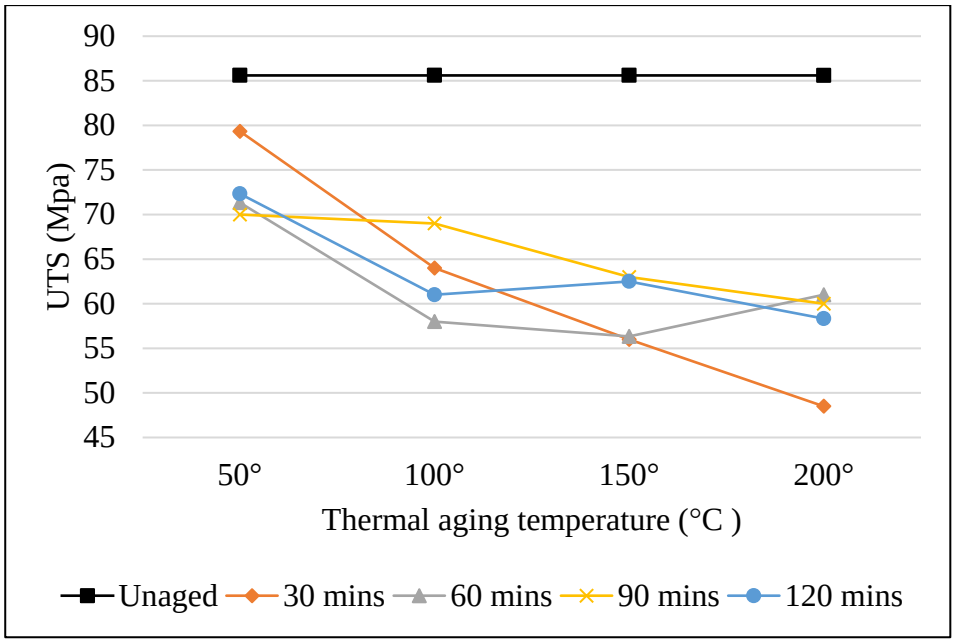

Fig. 4.30: Change of UTS due to thermal aging temperature.

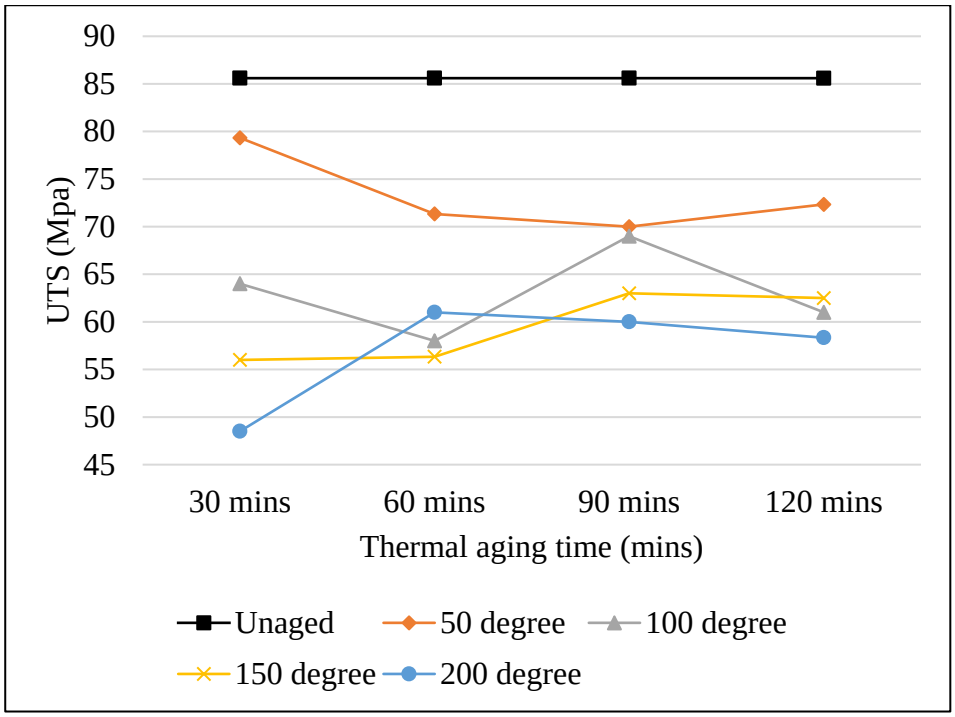

Fig 4.31: Change of UTS due to thermal aging time

From Figure 4.30, although there are some scatter and randomness in the mechanical properties after thermal aging consistent with the literature; the UTS of the thermally aged samples decreases as the thermal aging temperature increases. It is because the higher temperatures caused the epoxy to turn rubbery especially when the temperature is well beyond the Tg temperature. From Figure 4.31 however, no specific trend is observed as the

aging time increases for a specific temperature. In both cases, exposure to thermal aging always yields UTS values that are lower than the unaged UTS value. It confirms that even thermal aging below the Tg temperature cause a permanent loss of strength of GFRP.

Additionally, a Contour Surface plot was generated to understand the combined dependency of UTS of SGN 2 – 17 on thermal aging temperature and time. Figure 4.32 shows the contour plot of UTS.

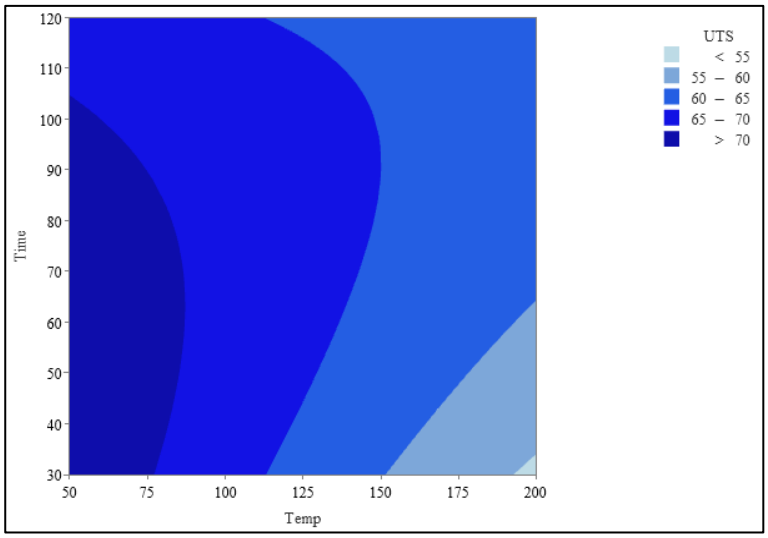

Fig. 4.32: Contour plot of UTS.

The contour plot shows the mapping of UTS values at various combinations of aging temperatures and time. In the plot, the UTS values are shown in 5 ranges which are represented by 5 shades of color. Darker shades represent higher values and lighter shades represent lower values. From the plot, the UTS decreases as temperatures reach higher values on the x-axis.

However, as the aging time increases for a specific temperature in the y-axis, no trend is observed. It also affirms the previous findings that the sensitivity of UTS reduction is more dependent on the change of thermal aging temperature rather than the thermal aging time between 30 mins and 120 mins. However, existing literature suggests that a reduction of UTS can result in case of longer thermal exposures in similar temperatures (Doblies et al., 2019). The variation of mechanical properties due to thermal aging time needs further research at higher aging periods to attain better understanding of the phenomenon.

Several researchers have investigated the effect of thermal aging on GFRP tensile properties. The work done by Doblies et al. is referred due to its relevance and similarity with this work. In the mentioned study the researchers experimented with tensile samples made with epoxy and thermally aged them it similar temperature ranges. Figure 4.33 shows the effect of Effect of thermal aging on GFRP tensile properties as per their study.

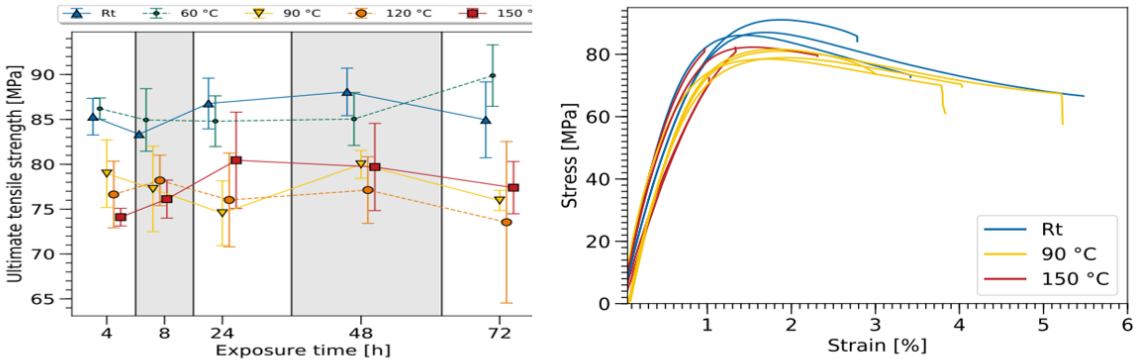

Table 2. UTS in MPa with standard deviation in MPa.

	4 h	8 h	24 h	48 h	72 h
20 °C	85.30 + 2.04	83.35 + 0	86.77 +2.82	88.06 + 2.64	84.95 + 4.23
60 °C	86.20 + 1.20	84.94 + 3.49	84.80 +2.83	85.04 + 2.94	89.88 + 3.42
90 °C	78.96 + 3.77	77.25 + 4.76	74.55 + 3.61	79.99 + 1.55	75.96 + 1.13
120 °C	76.64 + 3.71	78.20 + 2.82	76.02 + 5.22	77.13 + 3.71	73.54 + 9.0
150 °C	74.11 + 0.98	76.12 + 2.12	80.44 + 5.37	79.70 + 4.86	77.39 + 2.91

Fig. 4.33: Effect of thermal aging on GFRP tensile properties from literature (Doblies et al., 2019).

From the above findings, it is clear that the UTS of the epoxy decreased when exposed to thermal aging. Aging at the minimum 60 °C caused a permanent loss of UTS. Higher temperatures caused further loss of UTS although the data is scattered with high standard deviation. All these findings are similar to the findings of the present study.

CHAPTER 5
PREDICTIVE MODELING OF GFRP

5.1 Overview of the Predictive Model

The predictive model uses image processing, regression analysis and cascaded artificial neural networks (ANN) developed earlier to predict the Ultimate Tensile Strength (UTS) value with a photographic image of the sample. The model can also be customized to predict any mechanical properties with visually distinguishable identifiers dependent on thermal aging.

This model uses the color changes due to thermal aging from the photographic image as an identifier that allows it to estimate the UTS value without destructive testing. Firstly, the Image processing program reads the photographic image of the thermally aged samples and calculates the RGB color values. Two cascaded ANNs are used to estimate the thermal aging variables from the RGB color values. ANNs are used because this estimation follows a data-driven approach rather than a mathematical formulation. It involves several variables like the lighting conditions of the photo, image noise and sample precleaning which can impact the data accuracy of RGB values. With such scattered data, ANNs are found to be useful. Although the larger the dataset, the better. The regression analysis develops a mathematical equation to estimate the UTS values from the thermal aging temperature and time. The dataset in Appedix M is used for the regression analysis. Figure 5.1 shows the overview of the predictive model. The data source, input and output of elements within the predictive model is shown in Figure 5.2.

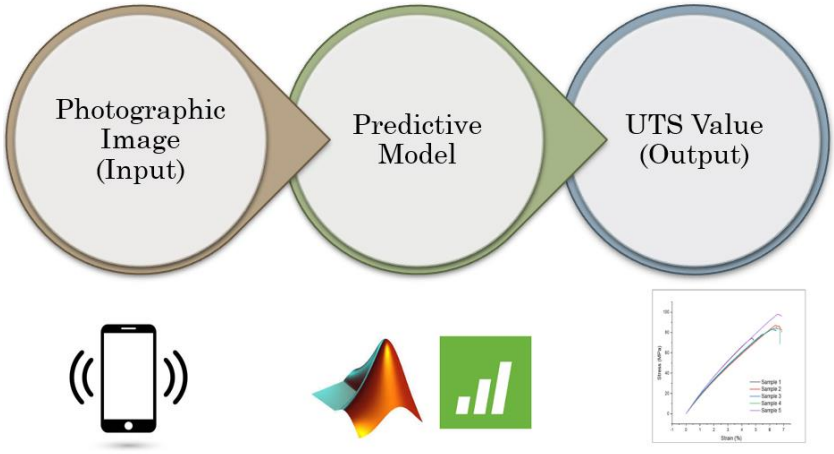

Fig. 5.1: Overview of the predictive model.

Data Source	Sample under study	Image Processing	Experimental work (at Lab)
Input	Photo of sample	RGB values	Thermal aging temperature and time
Output	RGB Values	Thermal aging temperature and time	UTS Value

Fig. 5.2: Data Source, input and output of elements within the predictive model.

5.2 Graphical Methodology of The Predictive Model

The Predictive Model was developed by combining the two separate parts of this research namely, the experimental work and then the development of the predictive model. Data obtained from the experimental work was used to develop the predictive model. Also, different stages of the predictive model received testing and training data from different stages of the experimental work. To aid the visualization of data flow between the experimental work and the predictive model, a graphical methodology has been prepared and shown in Figure 5.3.

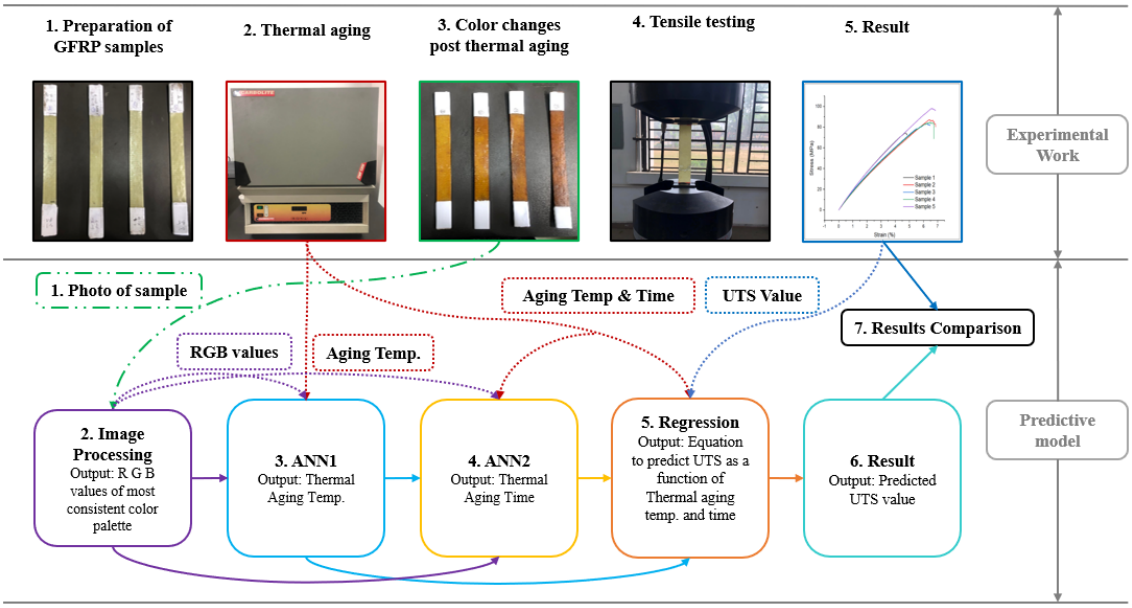

Fig 5.3. Graphical methodology of the predictive model.

The upper half of the Figure shows the experimental work. The work process has been shown in 5 sequential steps starting from preparation of GFRP sample, thermal aging in the oven, color changes post thermal aging, tensile testing and results. Step no 2, 3 and 5 has been shown in red, green and blue color respectively. This is done to better distinguish the flow of data from these steps to the predictive model.

The lower half shows the predictive model. There are 7 sequential steps starting from the photo of the sample, image processing, ANN1, ANN2, regression, result and results comparison. 3 types of lines have been shown in the graphical methodology. Continuous lines indicate the operational phase of the predictive model. Dotted lines indicate the training phase of the predictive model. Step 1 is common for both the operational and training phase of the model. It is indicated by 'long dash dot dot' line.

The three different techniques used in the predictive model serves three different purpose in the predictive model. The image processing part processes the image and prepares a dataset.

5.3 Image Processing

After the thermal aging was done, it was noted that the samples underwent a color change at 150°C and 200°C. This started at 150°C with a very slight shade of brown color which became more apparent at 200°C. Also, as the aging time increased, the shade of brown color became progressively darker. As such, this change of color could be used as an identifier to predict the thermal aging variables i.e., temperature and time.

To meet this purpose, A MATLAB image processing program was developed which can read and identify the color changes of the samples. SGN 10-17 were exposed to thermal aging at 150°C and 200°C. The photos of these SGN 10-17 were uploaded to the MATLAB program. The program performed calculations and gave the most consistent value of the Red, Green and Blue color (RGB) values in a matrix form for each of the samples. The code was optimized in such a way that even if there was some slight variation of color throughout different areas of the sample, the code was able to Figure out the most consistent value.

The Image processing program calculated the most consistent Red Green and Blue color values of all 51 samples. Then the average of these values for 3 samples within each sample group was taken to obtain the Red Green and Blue color values for a particular sample group number. Figure 5.4 shows the Red Green and Blue color values for SGN 1-17.

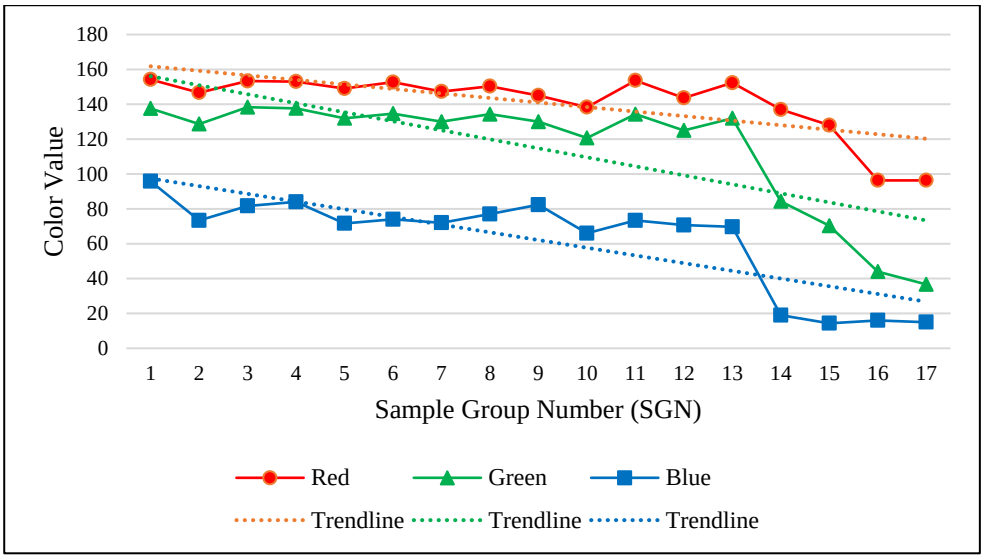

Fig 5.4. Red green and blue color values for SGN 1-17.

From the above Figure, it is observed that the RGB color values progressively decrease from SGN 1 to SGN 13. However, at SGN 14, when the thermal aging temperature reaches 200°C, the RGB color values decrease drastically. The overall trend of decreasing RGB color values is denoted by dotted lines for each respective color. The trend of decreasing RGB color values physically indicates the graduation darkening which ultimately reaches deep brown at SGN 17. This color change and the associated trend of RGB values agree with the color changes during thermal aging reported in Figure 4.25 from Chapter 4. These RGB values are used as an identifier for the ANNs.

5.4 Artificial Neural Networks (ANN)

A total of 24 sets of thermal aging data were used for the training and testing of the two ANNs. Among the 24 sets, 19 sets (80%) were used for the training and the remaining 5 sets (20%) were used for testing. Appendix G and appendix H shows the training and testing datasets for ANN1 and ANN2 respectively. The training performance of ANN1 and ANN2 is shown in Figure 5.5 and Figure 5.6 respectively.

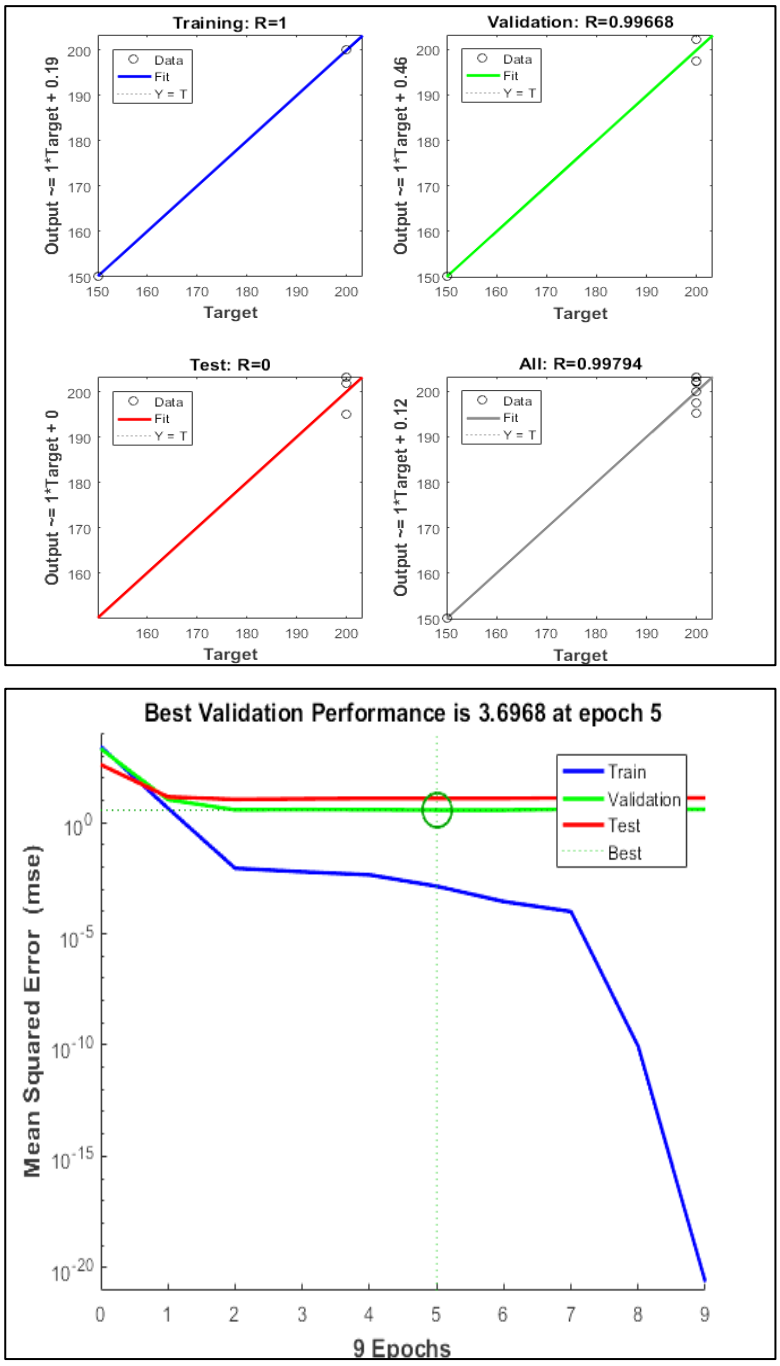

Fig 5.5: Training performance of ANN1.

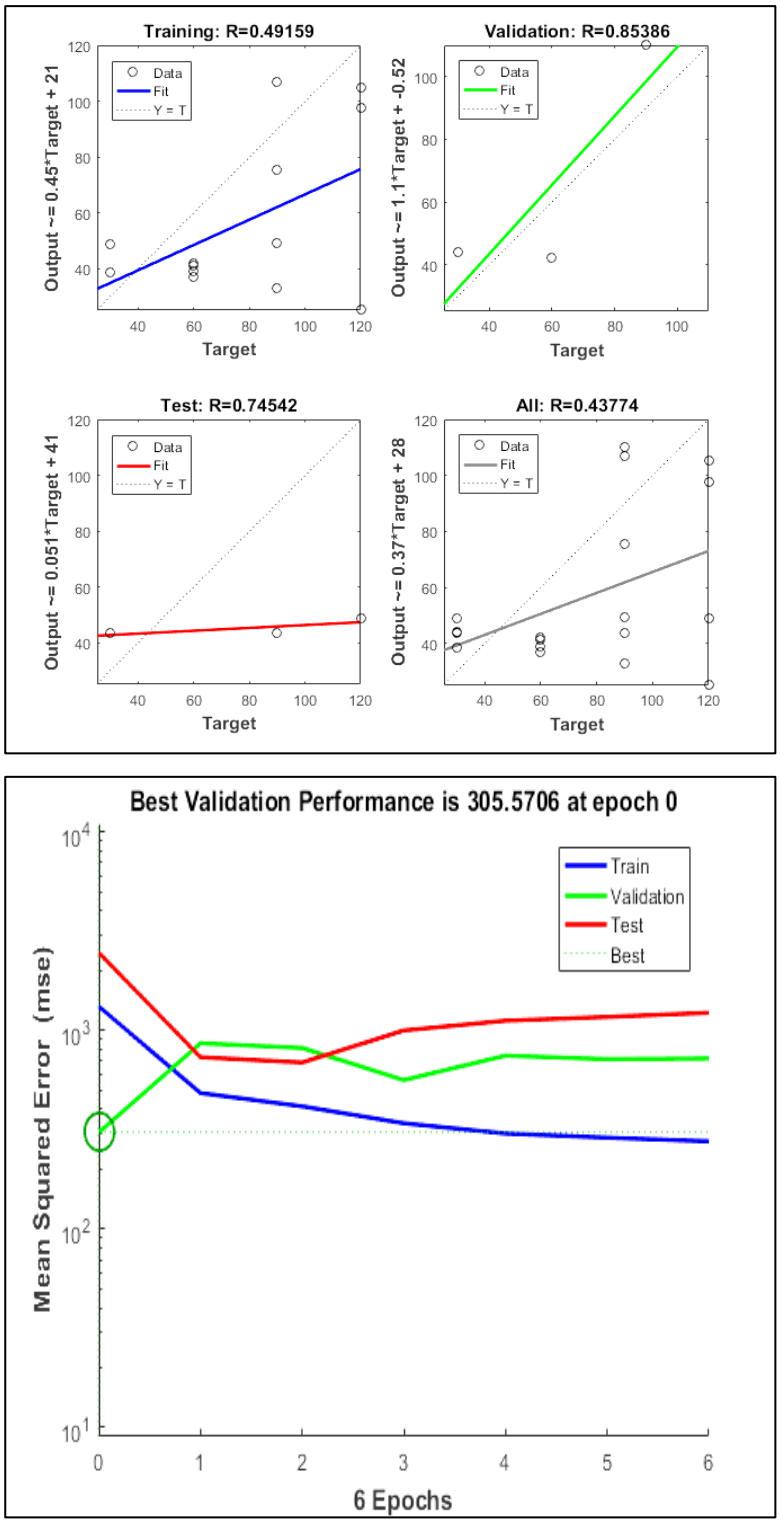

Fig 5.6: Training performance of ANN2.

From fig. 5.5, the overall R value for ANN1 is 0.99794 which indicates a good fit with the dataset. Generally, the closer the R value is to 1, the better in terms of an ANNs training befitting to the dataset. However, the overall R value for ANN2 is only 0.43774 which does

not indicate a good fit. The effect of the goodness of fit for ANN training is discovered during the testing phase.

When the training of the ANNs were complete, two neural networks were created in the MATLAB workspace. ANN1 was named as “network_temp.mat” and ANN2 was named as “network_time.mat”. Figure 5.7 shows the two trained networks in the MATLAB workspace.

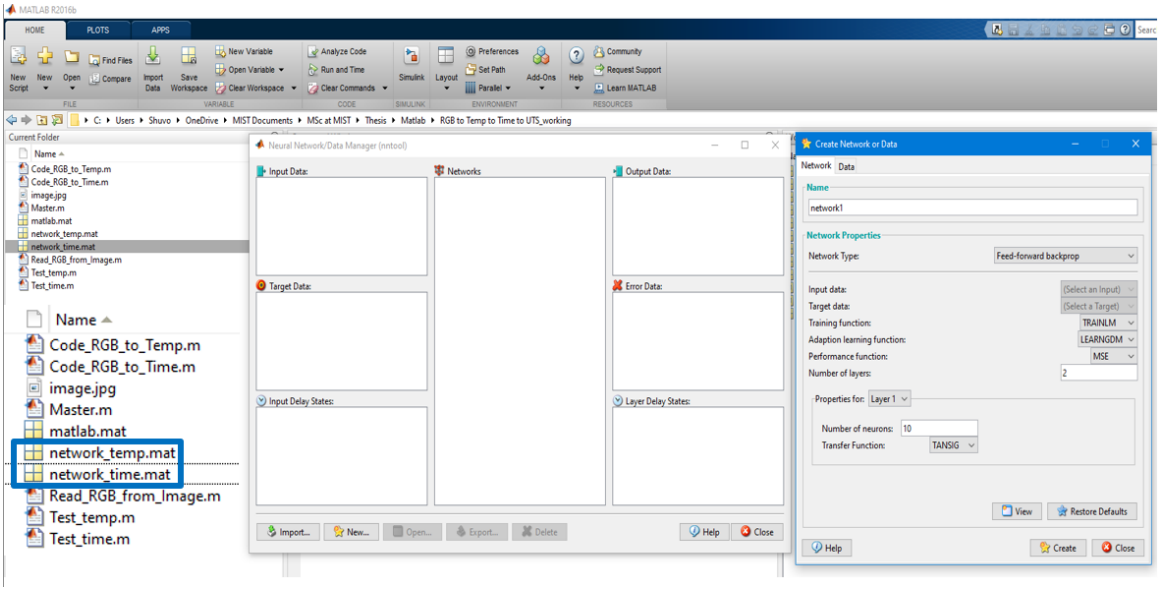

Fig. 5.7: Two trained ANNs in the MATLAB workspace.

The trained ANNs are tested with 5 sets of data each as per shown in Appendix G and Appendix H. The RGB values of the image processing program were given as input to the two cascaded ANNs to estimate the associated thermal aging temperature and time. The test performance of ANN1 and ANN2 is shown in Figure 5.8.

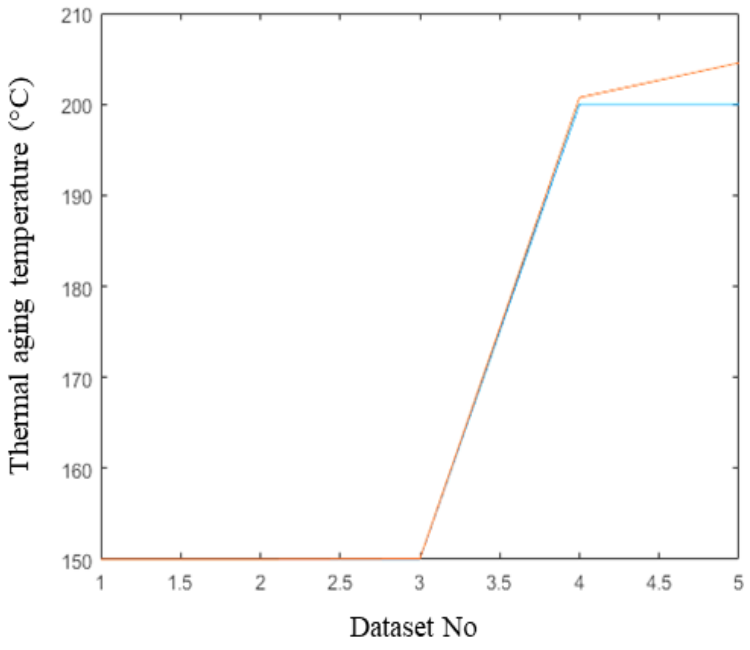

(a)

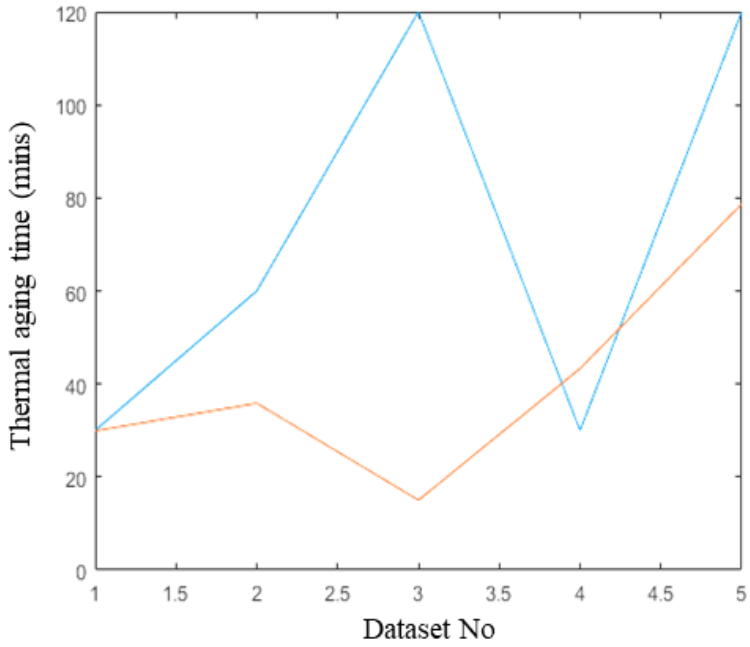

(b)

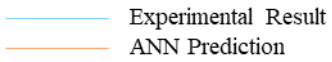

Fig 5.8: Testing performance of ANNs. (a) ANN1 (b) ANN2

From the above Figure, it is noted that ANN1 made very accurate estimations compared to the experimental results. This is relatable to the findings and analysis presented in of the experimental work Figure 4.30. As there was a trend of declining UTS with increasing

thermal aging time, ANN1 successfully followed the same. This was also expected as per the training performance of ANN1. However, ANN2 predictions have high errors. This is also relatable to the experimental work in Figure 4.31. In this case, there were no clear trends which led to ANN2 making high errors. This was also indicated during the training phase of ANN2. To achieve better results from ANN2, a much larger training dataset is required.

5.5 Regression Analysis

The final output of the regression analysis was an equation that establishes the relationship between the UTS value of the thermally aged GFRP and its associated thermal aging temperature and time. The tensile testing dataset of SGN 1-17 shown in Appendix R was used to perform the regression. Figure 9 shows the regression model and its various parameters.

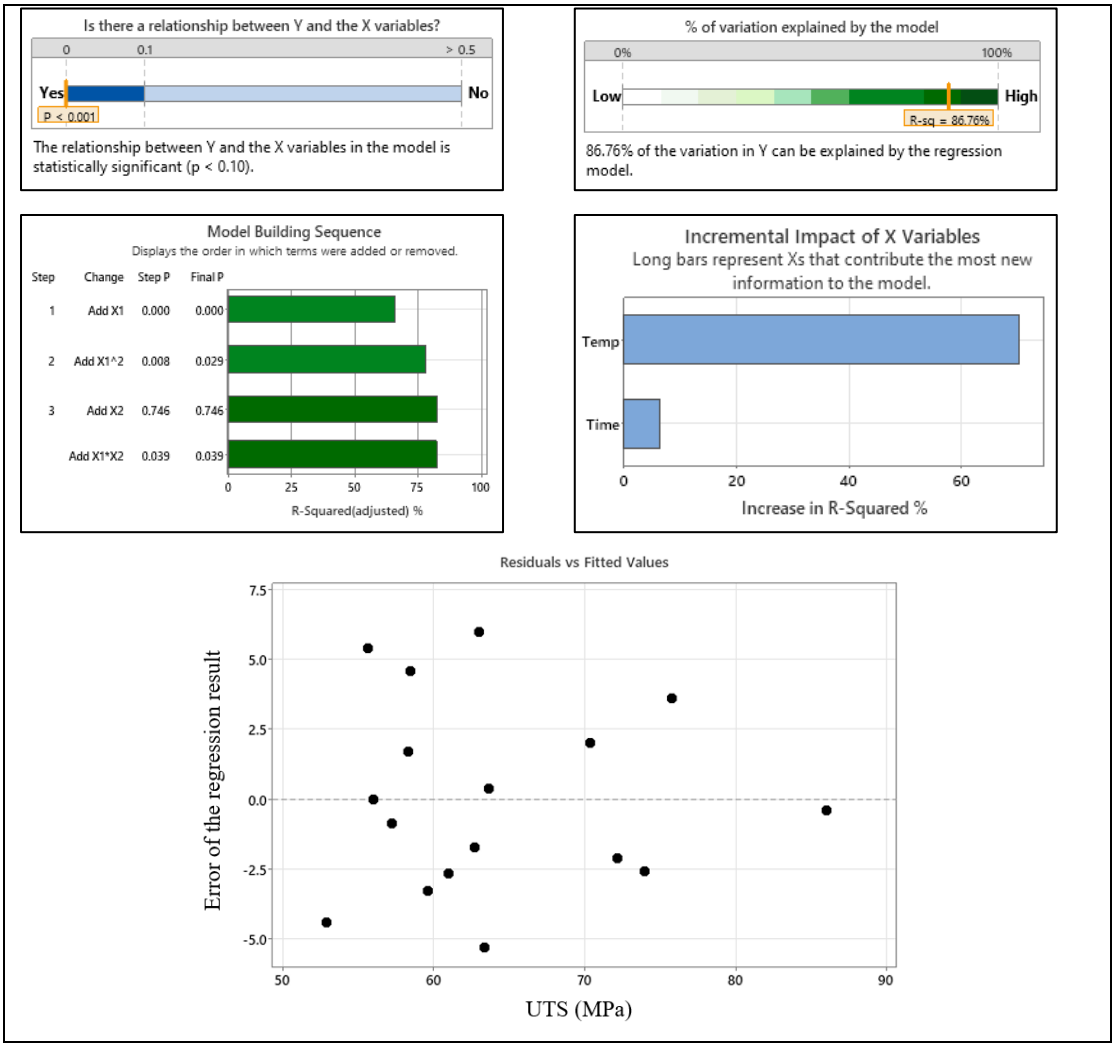

Fig 5.9. The regression model and its various parameters.

From the above Figures, it is observed that the p-value of the regression model was less than 0.10 which indicates a strong relationship between the y and x variables. The R^2 value was 86.76% which means that 86.76% of the variation in y can be explained by the regression model. The R^2 adjusted value was found as 82.351% which indicates that most of the variables were useful in terms of generating the model. The incremental impact of x variables indicated that aging temperature had a 70.3987% impact on increasing R^2 value compared to only 6.57032% for aging time. Also, there were no residual values nor any strong curvature or clusters which would have indicated problems with the regression model. All the data points fall randomly on both sides of zero indicating a good fit.

The regression analysis found the relationship for UTS as:

$$y = 95.63 - 0.4070 \times x_1 - 0.1099 \times x_2 + 0.000900 \times x_1^2 + 0.000998 \times x_1 \times x_2 \quad (5.1)$$

Where:

y = UTS (MPa)

x_1 = Thermal aging temperature (°C)

x_2 = Thermal aging time (mins).

A comparison was made between the results of the experimental work and the results obtained using the regression equation (1). Figure 5.10 shows the comparative plot of UTS values of SGN 1-17 obtained from experimental work and from the regression equation.

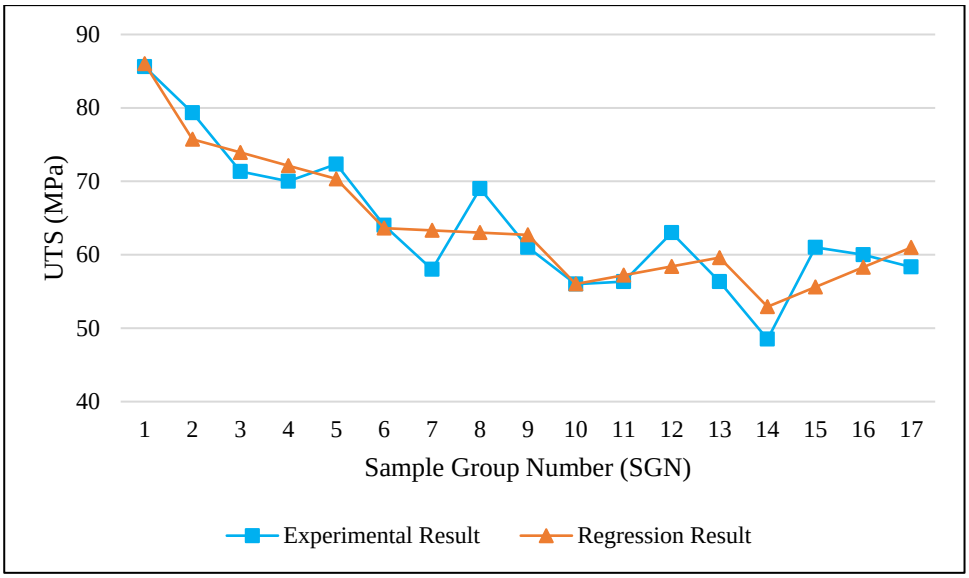

Fig. 5.10: Comparison of experimental and regression results for UTS.

From the Figure above it is seen that the UTS values obtained through the regression equation closely follow the experimental values. The average absolute error of all 17 SGN was calculated and found as 4%.

5.6 Performance of the Predictive Model

Combining the results from the Image Processing, Regression Analysis and Artificial Neural Networks; the predictive model predicted the UTS value of the thermally aged samples. The model was tested with 05 samples within SGN 10-17. Figure 5.11 graphically compares the experimental result and the predictive model predicted result. Table 5.1 shows the dataset of the experimental result and predictive model predicted result with associated errors.

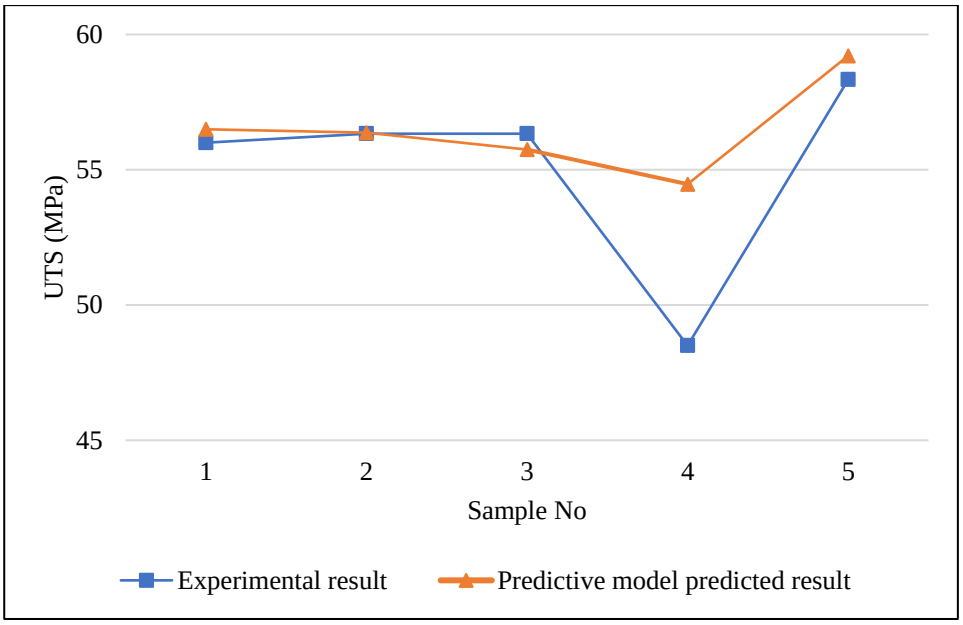

Fig 5.11: Comparison of experimental results with predictive model predicted results.

Table 5.1. Comparison of experimental results with predictive model predicted results

Sample No	SGN	Temp. (°C)	Time (mins)	Exp. UTS (MPa)	Predictive Model predicted UTS (MPa)	Error (%)	Absolute Error (%)
1	10	150	30	56.00	56.50	-1%	1%
2	11	150	60	56.33	56.37	0%	0%
3	13	150	120	56.33	55.75	1%	1%
4	14	200	30	48.50	54.47	-12%	12%
5	17	200	120	58.33	59.21	-2%	2%
Average Absolute Error							3%

From the Figure, it is evident that the predictive model estimated the experimental results of samples no 1, 2 and 3 with 99%, 100% and 99% accuracy. In sample no 4, the predictive model successfully followed the declining trend of the experimental result. However, the estimation had a 12% error. Again, in sample no 5, the predictive model successfully followed the rising trend of the experimental result and made an estimation with 98% accuracy. The average absolute accuracy of the predictive model is calculated as 97%.

The accuracy of the predictive model depends on the input image quality which influences the RGB values. Also, the accuracy largely depends on the regression equation as it is a

best-fit equation by nature that inherently has some errors. Moreover, the predictive model is compared with experimental results which are also prone to scattering due to matrix rearrangement post-thermal aging, sample randomness and several other experimental factors. It is seen that only in the case of sample 4, the predictive model made a noticeable error. This error may be attributed to the causes discussed above. In general, the accuracy of the predictive model can be maximized by increasing the number of experimental work samples and the ANN training dataset.

CHAPTER 6
CONCLUSIONS

6.1 Conclusions

This study investigated the mechanical properties of thermally aged GFRP composites. Also, a novel predictive model was also developed consisting of image processing, regression analysis and cascaded artificial neural networks. The conclusions of the study are presented as follows:

Woven Fiber GFRP exhibits superior mechanical properties compared to Random fiber GFRP. Mechanical cutting exhibits super surface finishing and mechanical properties compared to Laser cutting. Optimization of laser cutting parameters is critical to achieve good surface finish and mechanical properties.

Thermal aging of woven GFRP leads to color changes from 150°C onward (from light brown to gradually darker). UTS values slowly decline as samples are exposed to higher temperatures. The thermally aged UTS values have scattering which is consistent with the literature. The thermal aging temperature has a significantly higher impact (70.39%) than thermal aging time (6.57%) within the chosen thermal aging conditions.

The developed predictive model can estimate the UTS value of thermally aged samples with only a photographic image of the affected sample. The model has an average absolute accuracy of 97%. A Larger dataset can further improve the accuracy of the model.

6.2 Recommendations

The current research investigates the characterization and predictive modeling of thermally aged glass fiber reinforced plastic composites. In the future, the investigation can be continued by the augmentation of the following activities:

i. Investigation of different manufacturing techniques like compression molding and vacuum resin transfer molding.
ii. Optimization of laser machining parameters to have a better surface finish.
iii. Investigate a greater range of thermal aging temperatures and time. Particular attention may be given to temperatures beyond 200 °C.

iv. Investigation of the effect of thermal aging on other mechanical properties like flexural testing and microhardness.
v. Investigate the effect of larger datasets on the accuracy of the predictive model.

REFERENCES

Abass, B. A., Hunain, M. B., & Khudair, J. M. A. (2021, February 1). Effects of Titanium Dioxide Nanoparticles on the Mechanical Strength of Epoxy Hybrid Composite Materials Reinforced with Unidirectional Carbon and Glass Fibers. IOP Conference Series: Materials Science and Engineering, 1094(1), 012159. https://doi.org/10.1088/1757-899x/1094/1/012159

Alavudeen, A., Rajini, N., Karthikeyan, S., Thiruchitrambalam, M., Venkateshwaren, N., (2015). Mechanical properties of banana/kenaf fiber-reinforced hybrid polyester composites: Effect of woven fabric and random orientation. Mater. Des. 66, 246–257. https://doi.org/10.1016/j.matdes.2014.10.067

Almeida, J.H.S., Angrizani, C.C., Botelho, E.C., Amico, S.C., (2015). Effect of fiber orientation on the shear behavior of glass fiber/epoxy composites. Mater. Des. 65, 789–795. https://doi.org/10.1016/j.matdes.2014.10.003

Altin Karataş, M., Gökkaya, H., (2018). A review on machinability of carbon fiber reinforced polymer (CFRP) and glass fiber reinforced polymer (GFRP) composite materials. Defence Technology 14, 318–326. https://doi.org/10.1016/j.dt.2018.02.001

Ashrafi, H., Bazli, M., Jafari, A., Ozbakkaloglu, T., (2020). Tensile properties of GFRP laminates after exposure to elevated temperatures: Effect of fiber configuration, sample thickness, and time of exposure. Compos. Struct. 238, 111971. https://doi.org/10.1016/j.compstruct.2020.111971

Bakis, C.E., Bank, L.C., Brown, V.L., Cosenza, E., Davalos, J.F., Lesko, J.J., Machida, A., Rizkalla, S.H., Triantafillou, T.C., (2002). Fiber-Reinforced Polymer Composites for ConstructionState-of-the-Art Review. Journal of Composites for Construction 6, 73–87. https://doi.org/10.1061/(ASCE)1090-0268(2002)6:2(73)

Balguri, P. K., Samuel, D. H., & Thumu, U. (2021). A review on mechanical properties of epoxy nanocomposites. Materials Today: Proceedings, 44, 346–355. https://doi.org/10.1016/j.matpr.2020.09.742

Bazli, M., Ashrafi, H., Jafari, A., Zhao, X.L., Gholipour, H., Oskouei, A.V., (2019). Effect of thickness and reinforcement configuration on flexural and impact behaviour of GFRP laminates after exposure to elevated temperatures. Compos B Eng 157, 76–99. https://doi.org/10.1016/j.compositesb.2018.08.054

Bellenger, V., Verdu, J., (1985). Oxidative skeleton breaking in epoxy–amine networks. J Appl Polym Sci 30, 363–374. https://doi.org/10.1002/APP.1985.070300132

Beura, S., Thatoi, D., Chakraverty, A., Mohanty, U., (2018). Impact of the ambiance on GFRP composites and role of some inherent factors: A review report. Journal of Reinforced Plastics and Composites 37, 533–547. https://doi.org/10.1177/0731684418754359

Bishay, A., et al. (2017). Characterization and Prediction of the Glass Transition Temperature of Glass Fiber-Reinforced Polymer Composites. Journal of Composite Materials, 51(8), 1073-1087

Bhaskar, V., Kumar, D., Singh, K.K., (2019). Laser processing of glass fiber reinforced composite material: a review. Aust. J. Mech. Eng. 17, 95–108. https://doi.org/10.1080/14484846.2017.1363989

Egbo, M.K., (2021). A fundamental review on composite materials and some of their applications in biomedical engineering. Journal of King Saud University - Engineering Sciences 33, 557–568. https://doi.org/10.1016/j.jksues.2020.07.007

Birger, S., Moshonov, A., Kenig, S., (1989). The effects of thermal and hygrothermal ageing on the failure mechanisms of graphite-fabric epoxy composites subjected to flexural loading. Composites 20, 341–348. https://doi.org/10.1016/0010-4361(89)90659-9

Cai, R., Jin, T., (2018). The effect of microstructure of unidirectional fibre-reinforced composites on mechanical properties under transverse loading: A review. Journal of Reinforced Plastics and Composites 37, 1360–1377. https://doi.org/10.1177/0731684418796308

Choudhury, I.A., Chuan, P.C., (2013). Experimental evaluation of laser cut quality of glass fibre reinforced plastic composite. Opt. Lasers Eng. 51, 1125–1132. https://doi.org/10.1016/j.optlaseng.2013.04.017

Cs. Varga, N. Miskolczi, L.B. and G.L., (2010). Improving the Mechanical Properties of Glass-Fibre-Reinforced Polyester Composites by Modification of Fibre Surface [WWW Document]. Materials and Design, Vol. 31M. URL https://www.scirp.org/(S(351jmbntvnsjt1aadkposzje))/reference/ReferencesPapers.aspx?ReferenceID=1014445 (accessed 4.21.22).

Daniel, I.M., Ishai, O., (2005). Engineering Mechanics of Composite Materials. https://doi.org/10.1604/9780195150971

Devendra, K., Rangaswamy, T., (2012). Determination Of Mechanical Properties Of Al 2 O 3 , Mg (OH) 2 And Sic Filled E-Glass/ Epoxy Composites. International Journal of Engineering Research and Applications (IJERA) www.ijera.com 2, 2028–2033.

Dhawan, V., Singh, S., Singh, I., (2013). Effect of Natural Fillers on Mechanical Properties of GFRP Composites. J Compos 2013, 1–8. https://doi.org/10.1155/2013/792620

Doblies, A., Boll, B., Fiedler, B., (2019). Prediction of Thermal Exposure and Mechanical Behavior of Epoxy Resin Using Artificial Neural Networks and Fourier Transform Infrared Spectroscopy. Polymers 11, 363. https://doi.org/10.3390/polym11020363

Dodds, N., Gibson, A.G., Dewhurst, D., Davies, J.M., (2000). Fire behaviour of composite laminates. Compos Part A Appl Sci Manuf 31, 689–702. https://doi.org/10.1016/S1359-835X(00)00015-4

El-Hofy, M.H., Soo, S.L., Aspinwall, D.K., Sim, W.M., Pearson, D., Harden, P., (2011). Factors affecting workpiece surface integrity in slotting of CFRP. Procedia Eng 19, 94–99. https://doi.org/10.1016/J.PROENG.2011.11.085

EL-Wazery, M.S., EL-Elamy, M.I., Zoalfakar, S.H., (2017). Mechanical Properties Of Glass Fiber Reinforced Polyester Composites. Int. J. Appl. Sci. Eng. 14, 121–131. https://doi.org/10.6703/IJASE.2017.14(3).121

Erden, S., Sever, K., Seki, Y., Sarikanat, M., (2010). Enhancement of the mechanical properties of glass/polyester composites via matrix modification glass/polyester composite siloxane matrix modification. Fibers and Polymers 2010 11:5 11, 732–737. https://doi.org/10.1007/S12221-010-0732-2

Fatimah, S., Ishak, M., Aqida, S.N., (2012). CO2 Laser Cutting of Glass Fiber Reinforce Polymer Composite. IOP Conf Ser Mater Sci Eng 36, 012033. https://doi.org/10.1088/1757-899X/36/1/012033

Fazilat, H., Ghatarband, M., Mazinani, S., Asadi, Z.A., Shiri, M.E., Kalaee, M.R., (2012). Predicting the mechanical properties of glass fiber reinforced polymers via artificial neural network and adaptive neuro-fuzzy inference system. Computational Materials Science 58, 31–37. https://doi.org/10.1016/j.commatsci.2012.01.012

Gayatri Vineela, M., Dave, A., Kiran Chaganti, P., (2018). Artificial neural network based prediction of tensile strength of hybrid composites. Mater Today Proc 5, 19908–19915. https://doi.org/10.1016/j.matpr.2018.06.356

Ghafarizadeh, S., Lebrun, G., Chatelain, J.F., (2015). Experimental investigation of the cutting temperature and surface quality during milling of unidirectional carbon fiber reinforced plastic: http://dx.doi.org/10.1177/0021998315587131 50, 1059–1071. https://doi.org/10.1177/0021998315587131

Ghani, A.F.A., Mahmud, J., (2017). Shear deformation behavior of hybrid composite (GFRP/CFRP). Materialwissenschaft und Werkstofftechnik 48, 273–282. https://doi.org/10.1002/mawe.201600771

Gibson, A.G., Torres, M.E.O., Browne, T.N.A., Feih, S., Mouritz, A.P., (2010). High temperature and fire behaviour of continuous glass fibre/polypropylene laminates. Compos Part A Appl Sci Manuf 41, 1219–1231. https://doi.org/10.1016/J.COMPOSITESA.2010.05.004

Gibson, R.F. (2016). Principles of Composite Material Mechanics (4th ed.). CRC Press.

Hameed, N., Sreekumar, P.A., Francis, B., Yang, W., Thomas, S., (2007). Morphology, dynamic mechanical and thermal studies on poly(styrene-co-acrylonitrile) modified epoxy resin/glass fibre composites. Compos Part A Appl Sci Manuf 38, 2422–2432. https://doi.org/10.1016/J.COMPOSITESA.2007.08.009

Harada, Y., Kawai, K., Suzuki, T., Teramoto, T., (2012). Evaluation of cutting process on the tensile and fatigue strength of CFRP composites. Materials Science Forum 706–709, 649–654. https://doi.org/10.4028/www.scientific.net/MSF.706-709.649

Haykin, S. S. (2009), Neural networks and learning machines, Pearson Education , Upper Saddle River, NJ .

Hegde, S., Satish Shenoy, B., Chethan, K.N., (2019). Review on carbon fiber reinforced polymer (CFRP) and their mechanical performance. Materials Today: Proceedings 19, 658–662. https://doi.org/10.1016/j.matpr.2019.07.749

Hirsch, P., Bastick, S., Jaeschke, P., van den Aker, R., Geyer, A., Zscheyge, M., Michel, P., (2019). Effect of thermal properties on laser cutting of continuous glass and carbon fiber-

reinforced polyamide 6 composites. Mach. Sci. Technol. 23, 1–18. https://doi.org/10.1080/10910344.2018.1449216

Hull, D. and Clyne, T. W. (1996) An Introduction to Composite Materials. 2nd edn. Cambridge: Cambridge University Press (Cambridge Solid State Science Series). doi: 10.1017/CBO9781139170130.

Jafari, A., Bazli, M., Ashrafi, H., Oskouei, A.V., Azhari, S., Zhao, X.-L., Gholipour, H., (2019). Effect of fibers configuration and thickness on tensile behavior of GFRP laminates subjected to elevated temperatures. Constr. Build. Mater. 202, 189–207. https://doi.org/10.1016/j.conbuildmat.2019.01.003

Kaleg, S., Ariawan, D., Diharjo, K., (2018). The Flexural Strength of Glass Fiber Reinforced Polyester Filled with Aluminum Tri-Hydroxide and Montmorillonite. Key Engineering Materials 772, 28–32. https://doi.org/10.4028/www.scientific.net/kem.772.28

Karuppannan Gopalraj, S., Kärki, T., (2021). A Finite Element Study to Investigate the Mechanical Behaviour of Unidirectional Recycled Carbon Fibre/Glass Fibre–Reinforced Epoxy Composites. Polymers 13, 3192. https://doi.org/10.3390/polym13183192

Kim, Y., Oh, H., (2021). Comparison between Multiple Regression Analysis, Polynomial Regression Analysis, and an Artificial Neural Network for Tensile Strength Prediction of BFRP and GFRP. Materials 2021, Vol. 14, Page 4861 14, 4861. https://doi.org/10.3390/MA14174861

Kinloch, A.J., (1987). Adhesion and Adhesives: Science and Technology. https://doi.org/10.1023/b13212910.1007/978-94-015-7764-9

Kelly, A., Zweben, C., (1999). Comprehensive composite materials. Materials Today 2, 20–21. https://doi.org/10.1016/s1369-7021(99)80033-9

Krauklis, A.E., Echtermeyer, A.T., (2018). Mechanism of Yellowing: Carbonyl Formation during Hygrothermal Aging in a Common Amine Epoxy. Polymers 2018, Vol. 10, Page 1017 10, 1017. https://doi.org/10.3390/POLYM10091017

Krishnamoorthy, A., Boopathy, S.R., Palanikumar, K., (2009). Delamination Analysis in Drilling of CFRP Composites Using Response Surface Methodology:

http://dx.doi.org/10.1177/0021998309345309 43, 2885–2902. https://doi.org/10.1177/0021998309345309

Kun, G.A.O., Hanqiao, S.H.I., Baogang, S.U.N., Zhenhe, W., Zhiyong, Y., Yajuan, X. et al. (2016). Effects of hydro-thermal aging on properties of glass fiber/epoxy composites. Acta Materiae Compositae Sinica, 2016, Vol. 33, Issue 6, Pages: 1147-1152 33, 1147–1152. https://doi.org/10.13801/J.CNKI.FHCLXB.20160108.001

Lan, Z., Deng, J., Song, Y., Xu, Z., Nie, Y., Chen, Y., Ma, Y., (2022). Color Changes and Mechanical Properties of Glass Fiber Reinforced Polycarbonate Composites after Thermal Aging. Polymers (Basel) 14, 222. https://doi.org/10.3390/polym14020222

Le, T.-T., (2020). Surrogate Neural Network Model for Prediction of Load-Bearing Capacity of CFSS Members Considering Loading Eccentricity. Applied Sciences 10, 3452. https://doi.org/10.3390/app10103452

Read image from graphics file - MATLAB imread [WWW Document], n.d. . Read image from graphics file - MATLAB imread. URL https://www.mathworks.com/help/matlab/ref/imread.html

Deep Learning ToolboxDocumentation [WWW Document], n.d. . Deep Learning ToolboxDocumentation. URL https://www.mathworks.com/help/deeplearning/

Meng, Z., Hu, Y., Ancey, C., (2020). Using a Data Driven Approach to Predict Waves Generated by Gravity Driven Mass Flows. Water 12, 600. https://doi.org/10.3390/w12020600

Dodiuk, H. (Ed.), (2013). Handbook of Thermoset Plastics, Plastics Design Library. William Andrew.

Mishra, M., Agarwal, A., Maity, D., (2019). Neural-network-based approach to predict the deflection of plain, steel-reinforced, and bamboo-reinforced concrete beams from experimental data. SN Appl Sci 1, 584. https://doi.org/10.1007/s42452-019-0622-1

Morampudi, P., Namala, K. K., Gajjela, Y. K., Barath, M., & Prudhvi, G. (2021). Review on glass fiber reinforced polymer composites. Materials Today: Proceedings, 43, 314–319. https://doi.org/10.1016/j.matpr.2020.11.669

Mouritz, A.P., (2002). Post-fire flexural properties of fibre-reinforced polyester, epoxy and phenolic composites. J Mater Sci 37, 1377–1386. https://doi.org/10.1023/A:1014520628915

Nassar, A., & Nassar, E. (2020). Effect of fiber orientation on the mechanical properties of multi layers laminate nanocomposites. Heliyon, 6(1), e03167. https://doi.org/10.1016/j.heliyon.2020.e03167

Nayak, R.K., Dash, A., Ray, B.C., (2014). Effect of epoxy modifiers (Al 2 O 3 /SiO 2 /TiO 2) on mechanical performance of epoxy/glass fiber hybrid composites. Procedia Materials Science 6, 1359–1364. https://doi.org/10.1016/j.mspro.2014.07.115

Negarestani, R., & Li, L. (2012). Laser machining of fibre-reinforced polymeric composite materials. Machining Technology for Composite Materials, 288–308. https://doi.org/10.1533/9780857095145.2.288

Montgomery, D. C., Peck, E. A., & Vining, G. G. (2012). Introduction to Linear Regression Analysis (Vol. 821).

Parveez, B., Kittur, M.I., Badruddin, I.A., Kamangar, S., Hussien, M., Umarfarooq, M.A., (2022). Scientific Advancements in Composite Materials for Aircraft Applications: A Review. Polymers 14, 5007. https://doi.org/10.3390/polym14225007

Pan, Y., (2022). Mechanical and Microstructural Characteristics of the Fiber-Reinforced Composite Materials. Journal of Minerals and Materials Characterization and Engineering 10, 477–488. https://doi.org/10.4236/jmmce.2022.106034

Pavan, G., Singh, K.K., Mahesh, (2021). Elevated thermal conditioning effect on flexural strength of GFRP laminates: An experimental and statistical approach. Mater Today Commun 26, 101809. https://doi.org/10.1016/J.MTCOMM.2020.101809

Peairs, D.M., Park, G., Inman, D.J., (2004). Improving Accessibility of the Impedance-Based Structural Health Monitoring Method. Journal of Intelligent Material Systems and Structures 15, 129–139. https://doi.org/10.1177/1045389x04039914

Polanský, R., Mentlík, V., Prosr, P., Sušír, J., (2009). Influence of thermal treatment on the glass transition temperature of thermosetting epoxy laminate. Polymer Testing 28, 428–436. https://doi.org/10.1016/j.polymertesting.2009.03.004

Mijanur Rahman, M., Muzibur Rahman, M., (2023). Effect of laser cutting on mechanical performance of woven glass fiber reinforced plastic composites. Materials Today: Proceedings 80, 911–917. https://doi.org/10.1016/j.matpr.2022.11.327

Mohamed, Y.S., El-Gamal, H., Zaghloul, M.M.Y., (2018). Micro-hardness behavior of fiber reinforced thermosetting composites embedded with cellulose nanocrystals. Alexandria Engineering Journal 57, 4113–4119. https://doi.org/10.1016/j.aej.2018.10.012

Ratim, S., Bonnia, N.N., Surip, N.S., (2012). The effect of woven and non-woven fiber structure on mechanical properties polyester composite reinforced kenaf, in: AIP Conference Proceedings. pp. 131–135. https://doi.org/10.1063/1.4732481

Rao B, S.D., Sethi, A., Das, A.K., (2019). Fiber laser processing of GFRP composites and multi-objective optimization of the process using response surface methodology. J Compos Mater 53, 1459–1473. https://doi.org/10.1177/0021998318805139

Rose, M., Schettler, S., Klemm, F., Beyer, E., Zimmermann, M., Rose, M., Schettler, S., Klemm, F., Beyer, E., Zimmermann, M., (2020). Mechanical Properties of Remote-Laser Cut CFRP and Thermographic Laser-Process Monitoring. Mater. Sci. Appl. 11, 560–575. https://doi.org/10.4236/MSA.2020.118037

Roustazadeh, D., Aghadavoudi, F., Khandan, A., (2020). A synergic effect of CNT/Al2O3 reinforcements on multiscale epoxy-based glass fiber composite: fabrication and molecular dynamics modeling. https://doi.org/10.1080/08927022.2020.1815729 46, 1308–1319. https://doi.org/10.1080/08927022.2020.1815729

Saad, A. H., et al. (2020). A Review of Drilling Processes for Fiber-Reinforced Polymer Composites. Journal of Composite Materials, 54(1), 23-42.

Shalaby, Y., et al. (2018). Experimental Investigation and Analytical Modeling of the Effect of Thermal Aging on the Mechanical Properties of E-Glass/Polyester Composites. Polymer Testing, 69, 1-10.

Sathishkumar, T., Satheeshkumar, S., Naveen, J., (2014). Glass fiber-reinforced polymer composites – a review. Journal of Reinforced Plastics and Composites 33, 1258–1275. https://doi.org/10.1177/0731684414530790

Sehrawat, M., Rani, M., Bharadwaj, S., Sharma, S., Chauhan, G.S., Dhakate, S.R., Singh, B.P., (2022). Glass Transition Temperature Measurement of Polycarbonate Specimen by Dynamic Mechanical Analyser Towards the Development of Reference Material. MAPAN 37, 517–527. https://doi.org/10.1007/s12647-022-00572-3

Seydibeyoğlu, M. Z., Dogru, A., Wang, J., Rencheck, M., Han, Y., Wang, L., Seydibeyoğlu, E. A. et al. (2023). Review on Hybrid Reinforced Polymer Matrix Composites with Nanocellulose, Nanomaterials, and Other Fibers. Polymers, 15(4), 984. https://doi.org/10.3390/polym15040984

Slamani, M., Chatelain, J.-F., (2023). A review on the machining of polymer composites reinforced with carbon (CFRP), glass (GFRP), and natural fibers (NFRP). Discover Mechanical Engineering 2. https://doi.org/10.1007/s44245-023-00011-w

Solati, A., Hamedi, M., Safarabadi, M., (2019). Comprehensive investigation of surface quality and mechanical properties in CO 2 laser drilling of GFRP composites. International Journal of Advanced Manufacturing Technology 102, 791–808. https://doi.org/10.1007/S00170-018-3164-6

Song, Y., Deng, J., Xu, Z., Nie, Y., Lan, Z., (2022). Effect of thermal aging on mechanical properties and color difference of glass fiber/polyetherimide (Gf/pei) composites. Polymers (Basel) 14, 1–10. https://doi.org/10.3390/polym14010067

Standard Test Method for Tensile Properties of Polymer Matrix Composite Materials [WWW Document], (2014). . D3039/D3039M Standard Test Method for Tensile Properties of Polymer Matrix Composite Materials. URL https://www.astm.org/d3039_d3039m-08.html

Standard Test Methods for Flexural Properties of Unreinforced and Reinforced Plastics and Electrical Insulating Materials [WWW Document], (2017). . D790 Standard Test Methods for Flexural Properties of Unreinforced and Reinforced Plastics and Electrical Insulating Materials. URL https://www.astm.org/d0790-17.html

Standard Test Method for Microindentation Hardness of Materials [WWW Document], (2022). . E384 Standard Test Method for Microindentation Hardness of Materials. URL https://www.astm.org/e0384-22.html

The Questionable Engineering of Oceangate. (2023). YouTube. https://www.youtube.com/watch?v=6LcGrLnzYuU

Tikhani, F., Moghari, S., Jouyandeh, M., Laoutid, F., Vahabi, H., Saeb, M., & Dubois, P. (2020). Curing Kinetics and Thermal Stability of Epoxy Composites Containing Newly Obtained Nano-Scale Aluminum Hypophosphite (AlPO2). Polymers, 12(3), 644. https://doi.org/10.3390/polym12030644

Turco, C., Funari, M.F., Teixeira, E., Mateus, R., (2021). Artificial neural networks to predict the mechanical properties of natural fibre-reinforced compressed earth blocks (Cebs). Fibers 9. https://doi.org/10.3390/fib9120078

Udupi, S. R., & Lester Raj Rodrigues, L. (2016). Detecting Safety Zone Drill Process Parameters for Uncoated HSS Twist Drill in Machining GFRP Composites by Integrating Wear Rate and Wear Transition Mapping. Indian Journal of Materials Science, 2016, 1–8. https://doi.org/10.1155/2016/9380583

Zavatta, N., Rondina, F., Falaschetti, M.P., Donati, L., (2021). Effect of Thermal Ageing on the Mechanical Strength of Carbon Fibre Reinforced Epoxy Composites. Polymers (Basel) 13, 2006. https://doi.org/10.3390/polym13122006

Zhang, Kai, Zhang, Ke, Bao, R., (2023). Machine learning models to predict the residual tensile strength of glass fiber reinforced polymer bars in strong alkaline environments: A comparative study. Journal of Building Engineering 73, 106817. https://doi.org/10.1016/j.jobe.2023.106817

Zhou, Y., Wang, Y., Jeelani, S., & Xia, Y. (2007). Experimental Study on Tensile Behavior of Carbon Fiber and Carbon Fiber Reinforced Aluminum at Different Strain Rate. Applied Composite Materials, 14(1), 17–31. https://doi.org/10.1007/s10443-006-9028-5

Zuo, P., Tcharkhtchi, A., Shirinbayan, M., Fitoussi, J., Bakir, F., (2020). Effect of thermal aging on crystallization behaviors and dynamic mechanical properties of glass fiber reinforced polyphenylene sulfide (PPS/GF) composites. Journal of Polymer Research 27. https://doi.org/10.1007/S10965-020-02051-2

APPENDICES

Appendix A: Image Processing MATLAB Code

```
clc
% Import Image
I=imread('image.jpg');

%Seperate RGB values in seperate matrix
R=I(:,:,1);
G=I(:,:,2);
B=I(:,:,3);

%Calculate the Mode of each RGB Matrix
mode_R=mode(R);
mode_G=mode(G);
mode_B=mode(B);

%Calculate the Mean of all the values of mode_R, mode_G and mode_B
%matirx

mean_R=mean(mode_R)
mean_G=mean(mode_G)
mean_B=mean(mode_B)
```

Appendix B: ANN1 Training MATLAB Code

```
input_temp = [134   116 65
132 116 65
158 137 76
154 135 74
147 128 76
154 135 76
130 112 60
162 142 82
153 133 68
144 92  21
137 85  19
133 73  16
128 75  16
123 63  11
91  44  18
109 51  14
89  37  16
99  41  21
92  35  14
]';
target_temp = [150
150
150
150
150
150
150
150
200
200
200
200
200
200
200
200
200
200
]';
nntool
```

Appendix C: ANN2 Training MATLAB Code

```
input_time = [134   116 65  150
132 116 65  150
158 137 76  150
154 135 74  150
147 128 76  150
154 135 76  150
130 112 60  150
162 142 82  150
153 133 68  150
144 92  21  200
137 85  19  200
133 73  16  200
128 75  16  200
123 63  11  200
91  44  18  200
109 51  14  200
89  37  16  200
99  41  21  200
92  35  14  200
]';
target_time = [30
30
60
60
90
90
90
120
120
30
30
60
60
60
90
90
90
120
120
]';
nntool
```

Appendix D: ANN1 Testing MATLAB Code

```
test_temp = [149    130 68
149 131 70
142 121 59
130 76  17
98  34  10
]';
test_target_temp = [150
150
150
200
200
]';
result_temp=sim(network_temp,test_temp);
plot(test_target_temp); hold on; plot(result_temp);
fprintf('%5.5f \n', [test_target_temp]')
fprintf('%5.5f \n', [result_temp]')
```

Appendix E: ANN2 Testing MATLAB Code

```
test_time = [149    130 68  150
149 131 70  150
142 121 59  150
130 76  17  200
98  34  10  200
]';
test_target_time = [30
60
120
30
120
]';
result_time=sim(network_time,test_time);
plot(test_target_time); hold on; plot(result_time);
fprintf('%5.5f \n', [test_target_time]')
fprintf('%5.5f \n', [result_time]')
```

Appendix F: Predictive Model MATLAB Master Code

```
clear
load network_temp;
load network_time;

% Read RGB from Image

I=imread('image.jpg');

R=I(:,:,1);
G=I(:,:,2);
B=I(:,:,3);

mode_R=mode(R);
mode_G=mode(G);
mode_B=mode(B);

mean_R=mean(mode_R);
mean_G=mean(mode_G);
mean_B=mean(mode_B);

RGB_Matrix = [mean_R mean_G mean_B]
%Find Temp from RGB

test_temp = RGB_Matrix';
result_temp=sim(network_temp,test_temp)

%Find Time from RGB and Temp

test_time = [mean_R mean_G mean_B result_temp]';
result_time=sim(network_time,test_time)

%Calculate UTS from Regression Equation

result_UTS = 95.63-0.4070*result_temp-
0.1099*result_time+0.000900*result_temp^2+0.000998*result_temp*result_ti
me

%Calculate Max Strain from Regression Equation

result_max_strain = 6.522-0.01275*result_temp
```

Appendix G: ANN1 Dataset

Training Dataset

	Input (3)			Output (1)
Dataset No	R	G	B	Aging Temp (x_1)
1	134	116	65	150
2	132	116	65	150
3	158	137	76	150
4	154	135	74	150
5	147	128	76	150
9	154	135	76	150
7	130	112	60	150
8	162	142	82	150
9	153	133	68	150
10	144	92	21	200
11	137	85	19	200
12	133	73	16	200
13	128	75	16	200
14	123	63	11	200
15	91	44	18	200
16	109	51	14	200
17	89	37	16	200
18	99	41	21	200
19	92	35	14	200

Test Dataset

	Input (3)			Output (1)
Dataset No	R	G	B	Temp (x_1)
1	149	130	68	150
2	149	131	70	150
3	142	121	59	150
4	130	76	17	200
5	98	34	10	200

Appendix H: ANN2 Dataset

Training Dataset

	Input (4)				Output (1)
Dataset No	R	G	B	Temp (x_1)	Aging Time (x_2)
1	134	116	65	150	30
2	132	116	65	150	30
3	158	137	76	150	60
4	154	135	74	150	60
5	147	128	76	150	90
9	154	135	76	150	90
7	130	112	60	150	90
8	162	142	82	150	120
9	153	133	68	150	120
10	144	92	21	200	30
11	137	85	19	200	30
12	133	73	16	200	60
13	128	75	16	200	60
14	123	63	11	200	60
15	91	44	18	200	90
16	109	51	14	200	90
17	89	37	16	200	90
18	99	41	21	200	120
19	92	35	14	200	120

Test Dataset

	Input (4)				Output (1)
Dataset No	R	G	B	Temp (x_1)	Aging Time (x_2)
1	149	130	68	150	30
2	149	131	70	150	60
3	142	121	59	150	120
4	130	76	17	200	30
5	98	34	10	200	120

Appendix I: Technical Specifications of Glass Fiber Cloth

2. Technique Data Sheets for High Silica Cloth

1	WEAVE		SATIN 8HS		Testing Method
2	Width		92cm	36.2inch	DIN EN 1773
			100cm	39.4inch	
			84cm	33.1inch	
3	SiO2 Content		≥96%		-
4	Linear shrinkage (1000C 30min)		<7.10%		-
5	Area Shrinkage(1000C 30min)		<13.0%		-
6	Color		White / Golden		-
7	Thickness		1.3±0.1mm	0.051inch	DIN EN ISO 5084
8	Treatment		Hydrochloric acid treatment		-
9	Weight		1100g/m2	32.4OZ/YD2	DIN EN 12127
10	Thread count	WARP	20 per cm	51 per inch	DIN EN 1049-2
		WEFT	15 per cm	38 per inch	DIN EN1049-2
11	Tensile strength	WARP	≥1100		EN ISO 13934-1
	N/Inch	WEFT	≥900		EN ISO 13934-1
12	Service temperature		Up to 1100℃		-

Ref: http://www.jnglassfiber.com/

Appendix J: Technical Specifications of Epoxy Resin and Hardener

Property

Fatigue Strength

Tested using a load frequency of 90 Hz and a 1 inch (25 mm) joint overlap (Cured 20 min @ 212°F (100°C)

Fatigue Limit Load

% Static Shear Strength	Cycles to Failure[1]
50	10^3-10^4
40	10^4-10^5
30	10^5-10^6
25	10^5-10^6
20	10^6-10^7
15	10^7

Property	Test Method	Test Values[1]
Ultimate Tensile Strength, psi (MPa)	ASTM D-638	4800 (33)
Elongation, %	ASTM D-638	9
Tg per DMA, °F (°C)	ASTM D-4065	146 (63)
Hardness, Shore D	ASTM D-2240	80
Coefficient of Thermal Expansion (in/in/°C)	ASTM E-831	8.5×10^{-5}
Roller Peel Test, pli (N/mm)	ISO 4578	28 (4.9)

[1]Tested @ 77°F (25°C)

Electrical Properties

Thermal Conductivity, W/mK	0.22
Surface Resistivity, ohms	1.2 E+16
Dielectric Strength, volt/mil	400
Volume Resistivity, ohms-cm	7.1 E+14
Dielectric Constant, at 50Hz/1KHz/10KHz	3.4/3.2/3.2
Loss Tangent, % at 50Hz/1KHz/10KHz	1.7/1.8/2.6

STORAGE/ SHELF LIFE: Araldite epoxy adhesive components should be stored in their original, sealed containers at room temperature. When stored at temperatures from 59-77°F (15-25°C), the resin and hardener will remain in useable condition for 12 months from date of shipping from Huntsman.

Ref: https://www.huntsman.com/

Appendix K: ATR 72-212A Type Certificate Datasheet

ATR72-212A	PW127N	06 June 2014

ATR 72-101 / -201 and -102 / -202 models are certified for 120 min ETOPS operations according to Condition Technique Complémentaire (CTC) 20 ETOPS and in compliance with the technical requirements of AC 20-142A, issue dated December 30th, 1988.

ATR 72-212A model is certified for 120 min ETOPS operations (supported by ATR Modification 4711) in compliance with the technical requirements of JAA Information Leaflet n° 20.

The type design, system reliability and performance of ATR model(s) were found capable for extended range operations when configured, maintained and operated in accordance with the current revision of the ETOPS Configuration, Maintenance and Procedures (CMP) document applicable to each model.

This paragraph does not constitute an approval to conduct extended range operations. Operational approval must be obtained from the Authority responsible for aircraft operations.

Note: ATR 72-212A with MOD 7900 (full cargo) installed is not certified for ETOPS operations.

IV. Operating and Service Instructions

1. Airplane Flight Manual (AFM)
   Refer to relevant approved Airplane Flight Manual

2. Instructions for Continued Airworthiness and Airworthiness Limitations
   Refer to ATR AMM, SRM, IPC, CMM documents and the relevant approved "Time Limits" document

3. Weight and Balance Manual (WBM)
   Refer to Weight and Balance Manual

V. Operational Suitability Data (OSD)

The Operational Suitability Data elements listed below are approved by the European Aviation Safety Agency under the EASA Type Certificate [TC number EASA.A.084] as per Commission Regulation (EU) 748/2012 as amended by Commission Regulation (EU) No 69/2014.

1. Master Minimum Equipment List
   a) Master Minimum Equipment List (ATR 42 and ATR 72 Master Minimum Equipment List (MMEL) EDORA reference: EFOS-4775/15) approved at revision 00 dated December 2015, (refer to the latest approved revision) as per the defined Master Minimum Equipment List Operational Suitability Data Certification Basis: JAR MMEL / MEL, Amendment 1.

An agency of the European Union

Ref: www.easa.europa.eu

https://www.easa.europa.eu/en

Appendix L: ATR 72-212A Air Conditioning System Schematic

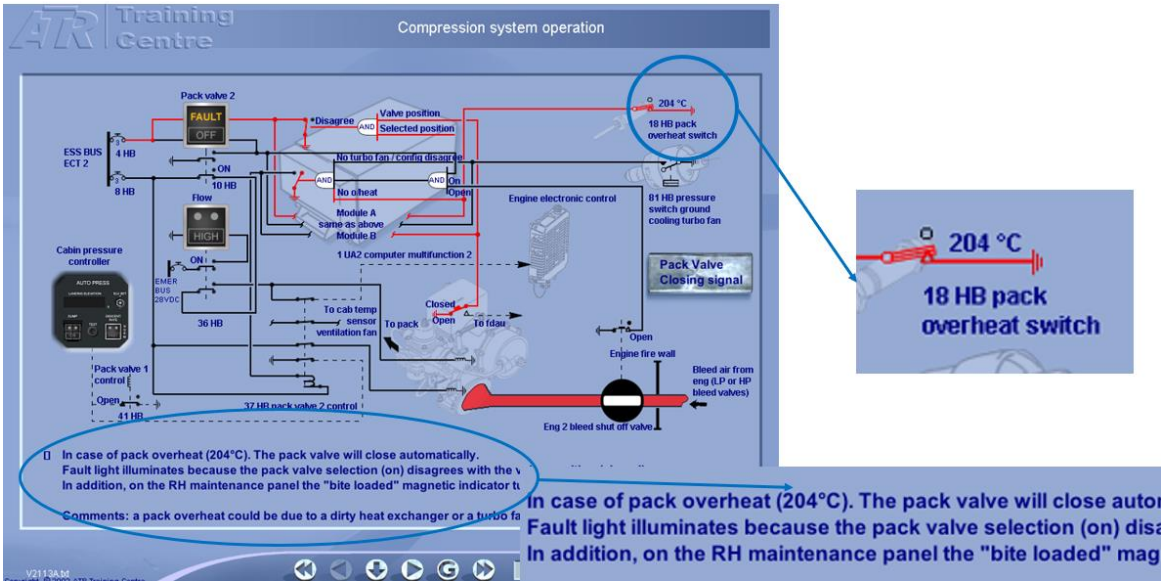

Ref: [ATR Training Centre - ATR Aircraft (atr-aircraft.com)]

https://www.atr-aircraft.com/training/atr-training-centre/

Appendix M: Materials Used for GFRP fabrication

(a) (b)

Fig: Glass fiber cloth (a) Woven (b) Random

Fig: Araldite AW 106 IN epoxy resin and HV 953 U hardener

Appendix N: Photos of Lab Equipment and Apparatus

Fig: HST Kason PLS 100 UTM Machine (For Tensile and Flexural Test)

Fig: TMTECK-10MDT Auto Turret Vickers Microhardness Tester

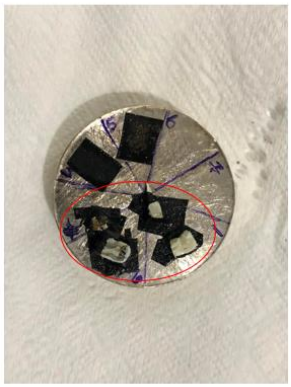

GFRP samples are placed on the SEM platform

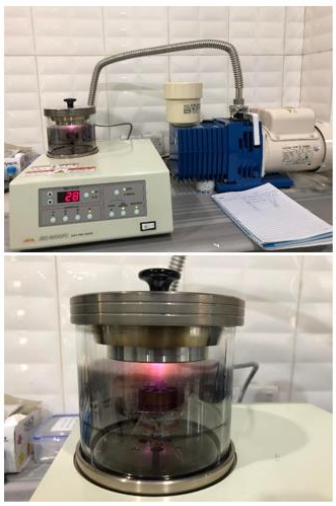

Platinum coating process

SEM machine JSM-7610F

Fig: SEM Imaging Equipment

Fig: Bosch GWS 900-100 professional angle grinder with TJWELD 1.2 mm thickness cutting wheel

Fig: TJWELD 1.2 mm thickness cutting wheel

Fig: CO_2 laser cutting machine model STJ1530M

Appendix O: Tensile Test Data of Unaged Samples

Tensile test data of Woven GFRP mechanically cut samples

Sample No	UTS (MPa)	Yield Strength (MPa)	Elastic Modulus (GPa)
Sample 1	74	22	1.65
Sample 2	87	26	1.37
Sample 3	84	25	1.42
Sample 4	85	25	1.41
Sample 5	98	30	1.51
Average	85.6	25.60	1.47
Standard Deviation	8.56	2.88	0.11

Tensile test data of Woven GFRP laser cut samples

Sample No	UTS (MPa)	Yield Strength (MPa)	Elastic Modulus (GPa)
Sample 1	64	19.00	1.17
Sample 2	67	20.00	1.4
Sample 3	42	13.00	1.06
Sample 4	74	22.00	1.47
Sample 5	70	21.00	1.39
Average	63.4	19.00	1.30
Standard Deviation	12.52	3.54	0.17

Tensile test data of Random GFRP mechanically cut samples

Sample No	UTS (MPa)	Yield Strength (MPa)	Elastic Modulus (GPa)
1	50	15	0.75
2	57	17	0.83
3	58	17	0.80
4	53	16	0.77
5	53	16	0.87
Average	54.20	16.20	0.80
Standard Deviation	3.27	0.84	0.05

Tensile test data of Random GFRP laser cut samples

Sample No	UTS (Mpa)	Yield Strength	Elastic Modulus (GPa)
1	46	14.00	0.76
2	30	9.00	0.75
3	46	14.00	0.73
4	49	15.00	0.71
5	48	14.00	0.75
Average	43.8	13.20	0.74
Standard Deviation	7.82	2.39	0.02

Appendix P: Flexural Test Data of Unaged Samples

Flexural test data of woven GFRP

Machining	Sample	UFS (Mpa)	E (Flex Modulus) Gpa
Mechanical (MC)	Sample 1	88.78	3.33
	Sample 2	93.50	3.71
	Sample 3	58.66	2.48
	Sample 4	64.67	3.72
	Sample 5	62.70	3.82
	Average	73.66	3.41
	Std Dev	16.19	0.55
Laser (LC)	Sample 1	56.16	3.16
	Sample 2	47.11	1.83
	Sample 3	59.68	3.02
	Sample 4	50.32	3.05
	Sample 5	69.90	3.46
	Average	56.63	2.91
	Std Dev	8.89	0.62

Table. Flexural test data of random GFRP

Machining	Sample	UFS (Mpa)	E (Flex Modulus) Gpa
Mechanical (MC)	Sample 1	35.63	0.78
	Sample 2	54.04	2.06
	Sample 3	67.61	2.36
	Sample 4	93.90	3.38
	Sample 5	58.27	2.13
	Average	52.43	2.14
	Std Dev	16.05	0.93
Laser (LC)	Sample 1	42.36	2.14
	Sample 2	44.75	2.53
	Sample 3	36.91	1.90
	Sample 4	91.67	2.93
	Sample 5	38.33	0.95
	Average	41.34	2.09
	Std Dev	4.02	0.75

Appendix Q: Microhardness Test Data of Unaged Samples

Vickers Micro Hardness test data of woven GFRP

Sample No	HV Value (Mechanically Cut)	HV Value (Laser Cut)
Sample 1	34.26	37.36
Sample 2	33.75	34.00
Sample 3	31.84	36.91
Sample 4	37.71	35.62
Sample 5	35.14	39.67
Average	34.54	36.71
Standard Deviation	2.14	2.11

Vickers Micro Hardness test data of random GFRP

Sample No	HV Value (Mechanically Cut)	HV Value (Laser Cut)
Sample 1	5.8	5.46
Sample 2	4.08	4.76
Sample 3	4.58	5.2
Sample 4	6.54	4.76
Sample 5	3.08	4.68
Average	4.82	4.97
Standard Deviation	1.37	0.34

Appendix R: Tensile Test Dataset with Thermal Aging Variables

Tensile test dataset with thermal aging variables and corresponding mechanical properties

SGN	Temperature (°C)	Time (mins)	UTS (MPa)	Max Strain (%)	Yield Strength (MPa)
1	Unaged	Unaged	85.6	6.34	25.60
2	50	30	79.33	5.52	23.83
3	50	60	71.33	5.74	20.50
4	50	90	70.00	6.30	21.47
5	50	120	72.33	5.71	21.54
6	100	30	64.00	5.64	19.33
7	100	60	58.00	5.39	17.65
8	100	90	69.00	5.59	20.67
9	100	120	61.00	4.83	18.53
10	150	30	70.33	4.37	17.00
11	150	60	56.33	4.22	17.00
12	150	90	80.67	5.02	19.00
13	150	120	62.50	5.08	19.00
14	200	30	47.00	3.71	11.90
15	200	60	63.33	4.41	18.50
16	200	90	64.67	4.06	18.50
17	200	120	58.33	3.99	17.67

Appendix S: Publication Endeavors of This Study

At the time of writing this thesis, this research work has produced one published paper, one paper in the process of being published and one paper in the review process. The details of the publication endeavor are as follows:

i. Mijanur Rahman, M., Muzibur Rahman, M., 2023. Effect of laser cutting on mechanical performance of woven glass fiber reinforced plastic composites. Materials Today: Proceedings 80, 911–917. https://doi.org/10.1016/j.matpr.2022.11.327

ii. Mechanical Performance of Mat Glass Fiber Reinforced Plastic (GFRP) Composites subjected to Laser Cutting.
Presented at ICMEAS 22 – MIST. The Paper is accepted for publishing at Scopus-indexed proceedings.

iii. Characterization and Predictive Modeling of Thermally Aged Glass Fiber Reinforced Plastic Composites.
The Paper is under review at a Q-ranked journal.